LOW GRADIENT MAGNETIC SEPARATION OF MAGNETIC NANOPARTICLE UNDER CONTINUOUS FLOW: EXPERIMENTAL STUDY, TRANSPORT MECHANISM AND MATHEMATICAL MODELLING

TAN YEE WIN

MASTER OF ENGINEERING SCIENCE

FACULTY OF ENGINEERING AND GREEN TECHNOLOGY
UNIVERSITI TUNKU ABDUL RAHMAN
OCTOBER 2022

LOW GRADIENT MAGNETIC SEPARATION OF MAGNETIC NANOPARTICLE UNDER CONTINUOUS FLOW: EXPERIMENTAL STUDY, TRANSPORT MECHANISM AND MATHEMATICAL MODELLING

By

TAN YEE WIN

A dissertation submitted to the Department of Industrial Engineering,
Faculty of Engineering and Green Technology,
Universiti Tunku Abdul Rahman,
in partial fulfillment of the requirements for the degree of
Master of Engineering Science
October 2022

ABSTRACT

LOW GRADIENT MAGNETIC SEPARATION OF MAGNETIC NANOPARTICLE UNDER CONTINUOUS FLOW: EXPERIMENTAL STUDY, TRANSPORT MECHANISM AND MATHEMATICAL MODELLING

Tan Yee Win

Low gradient magnetic separation (LGMS) of magnetic nanoparticles (MNP) has been proven to be one of the techniques with great potential for biomedical and environmental engineering applications. Recently, the underlying principle of particle capture by LGMS, through a process known as magnetophoresis, under the influence of hydrodynamic effect has been widely studied and illustrated. Even though the influence of hydrodynamic effect is very substantial for batch processes, its impact on LGMS operated at continuous flow condition remained largely unknown. Hence, in this study, the dynamical behavior of LGMS process operated under continuous flow (CF) was being studied in detail. Firstly, the LGMS experiments using poly(sodium 4-styrenesulfonate) (PSS)-functionalized-MNP with 44.1 nm core diameter and 245.3 nm hydrodynamic diameter (saturation magnetization = 69.48 emu/g) as modelled particle system was performed through batchwise (BW) and CF

modes at different operating conditions, including (i) magnet arrangement, (ii) MNP concentration, and (iii) MNP solution flowrate. Here BW operation was used as a comparative study to elucidate the transport mechanism of MNP under the similar environment of CF-LGMS process, and it was found out that the convection induced by magnetophoresis is only significant at far-from-magnet region. Since the timescale for the induced convection to be effective is ~1200 seconds as observed from BW-LGMS experiments, it can be deduced that forced convection is more dominant on influencing the transport behavior of CF-LGMS (with resident time of about or less than 240 seconds). Moreover, in this study, it was found that the separation efficiency of CF-LGMS process can be boosted by the higher number of magnets, the higher MNP concentration and the lower flowrate of MNP solution. To better illustrate the underlying dynamical behavior of LGMS process, a mathematical model was developed to predict its separation efficiency and kinetic profile. The separation efficiency of CF-LGMS process was determined at great accuracy, with average error of ~2.6% compared to the experimental results. Last but not least, to verify the feasibility of implementing the CF-LGMS process to achieve sufficiently high separation efficiency in the real time application, the CF-LGMS experiments were conducted in multistage manner, which resembles the MNP solution that is flowing through a few separation columns at are connected in series. The outcome from these experiments shows that the separation efficiency (both experiment and simulation results) can be boosted to almost 90% after undergoing 3 stages of CF-LGMS column.

ACKNOWLEDGEMENT

Foremost, I am extremely grateful to my supervisor Dr Leong Sim Siong for the invaluable advice and continuous support of my Master study, for his patience, motivation, and enthusiasm. His immense knowledge and valuable guidance have helped me in all the time of my academic research. I could not have imagined having a great supervisor and guide in my research. Also, I would like to thank to my co-supervisor Prof. Lim Jit Kang, who provided valuable suggestions and guidance that greatly improved my research work. Next, many thanks to Dr Yeoh Wei Ming for the constant support throughout this research.

In addition, I wish to thank my loving and supportive parents and friends who have helped and encouraged me. Their belief in me has kept my spirits and motivation high during this process, without their constant love and support I would not have been able to successfully complete my studies. Besides, I would like to thank all the Petrochemical Laboratory staffs for their assistance in helping me to conduct the research.

APPROVAL SHEET

This dissertation entitled "**LOW GRADIENT MAGNETIC SEPARATION OF MAGNETIC NANOPARTICLE UNDER CONTINUOUS FLOW: EXPERIMENTAL STUDY, TRANSPORT MECHANISM AND MATHEMATICAL MODELLING"** was prepared by TAN YEE WIN and submitted as partial fulfillment of the requirements for the degree of Master of Engineering Science at Universiti Tunku Abdul Rahman.

Approved by:

(Dr. LEONG SIM SIONG)
Date: 4th October 2022
Supervisor
Department of Industrial Engineering
Faculty of Engineering and Green Technology
Universiti Tunku Abdul Rahman

(Dr. YEOH WEI MING)
Date: 4th October 2022
Co-supervisor
Department of Petrochemical Engineering
Faculty of Engineering and Green Technology
Universiti Tunku Abdul Rahman

FACULTY OF ENGINEERING AND GREEN TECHNOLOGY

UNIVERSITI TUNKU ABDUL RAHMAN

Date: 4th October 2022

SUBMISSION OF DISSERTATION

It is hereby certified that ***TAN YEE WIN*** (ID No: ***20AGM05310***) has completed this dissertation entitled "*LOW GRADIENT MAGNETIC SEPARATION OF MAGNETIC NANOPARTICLE UNDER CONTINUOUS FLOW: EXPERIMENTAL STUDY, TRANSPORT MECHANISM AND MATHEMATICAL MODELLING*" under the supervision of Dr. Leong Sim Siong (Supervisor) from the Department of Industrial Engineering, Faculty of Engineering and Green Technology, and Dr. Yeoh Wei Ming (Co-Supervisor) from the Department of Petrochemical Engineering, Faculty of Engineering and Green Technology.

I understand that University will upload softcopy of my dissertation in pdf format into UTAR Institutional Repository, which may be made accessible to UTAR community and public.

Yours truly,

_____

(*TAN YEE WIN*)

DECLARATION

I hereby declare that the dissertation is based on my original work except for quotations and citations which have been duly acknowledged. I also declare that it has not been previously or concurrently submitted for any other degree at UTAR or other institutions.

Name TAN YEE WIN

Date 4th October 2022

TABLE OF CONTENTS

LIST OF TABLES

LIST OF FIGURES

LIST OF ABBREVIATIONS

BW	Batchwise
BW-LGMS	Batchwise Low Gradient Magnetic Separation
CF	Continuous flow
CF-LGMS	Continuous Flow Low Gradient Magnetic Separation
DI	Deionized
DLS	Dynamic light scattering
Gr_m	Magnetic Grashof Number
HGMS	High Gradient Magnetic Separation
IONPs	Iron Oxide Nanoparticles
LGMS	Low Gradient Magnetic Separation
MNPs	Magnetic Nanoparticles
NdFeB	Neodymium Ferrum Boron
PDDA	Poly(diallyldimethylamonium chloride)
PSS	Poly(Sodium 4-Styrenesulfonate)
VSM	Vibrating Sample Magnetometer

CHAPTER ONE

INTRODUCTION

This chapter outlines a brief introduction on the several topics that are related to this research work. The first section of this chapter describes the main physical phenomenon relevant to this study, namely magnetophoresis of magnetic nanoparticles (MNPs). After that, the magnetic separation under batchwise and continuous flow mode are introduced. Next, the mathematical modelling of magnetophoresis kinetics with the consideration of cooperative and hydrodynamic effects are elaborated. Moreover, this chapter also includes problem statements and research objectives of this study.

1.1 Magnetophoresis of Magnetic Nanoparticles (MNPs)

The engineering application of separation processes by using magnetism has undergone rapid development in the past 200 years, which subsequently driven the need to synthesize well-engineered magnetic nanoparticles (MNPs) in the recent decades (Zborowski et al., 1999; Lim et al., 2014; Sangaiya and Jayaprakash, 2018; Devi, Nivetha and Prabha, 2019). The application of MNPs in separation process often involves its motion controlled by external magnetic field under a non-contact/non-invasive mode (Krishnan et al., 2009; Benelmekki et al., 2011; Lim et al., 2012). This process is commonly known as

magnetophoresis of the MNPs, which is the motion of MNPs in relative to the surrounding fluid in response to the externally applied magnetic field (Yavuz et al., 2006; Faraudo, Andreu and Camacho, 2013; Leong, Ahmad and Lim, 2015; Yan et al., 2017). The growing interest on magnetophoresis of MNPs among technologists is attributed to its simplicity, excellent efficiency, well-defined magnetic field, non-invasive nature, wide selection of MNP material as well as the ability to operate under ambient temperatures (Liu et al., 2018; Ma et al., 2019; Tang et al., 2019; Leong et al., 2020). Hence, plenty of engineering applications have been developed according to this concept, which are ranging from environmental treatment to biomedical fields (Laurent et al., 2008; Hyun and Jung, 2013; Gómez-Pastora, Bringas and Ortiz, 2014; Chen et al., 2015; Narayana Iyengar et al., 2021).

Typically, in a magnetic separation process, MNPs are first dispersed in the solution to be treated so that the targeted substances can be specifically tagged by MNPs through physical or chemical bindings (Zborowski et al., 2003; Yeap et al., 2014; Chong, Leong and Lim, 2021; Sun et al., 2021). Next, with the appropriate application of a magnetic field (can be produced by an electromagnet or permanent magnet), MNPs can be isolated from the solution together with the targeted substances (Lim et al., 2014; Lim, Yeap and Low, 2014; Khizar et al., 2020). By this way, the targeted substances are separated from the solution which is leading to the formation of clear solution free of the targeted substances. After that, the used MNPs can be regenerated by detaching the targeted substances from them, which can be recycled in the subsequent separation operations (Leong, Yeap and Lim, 2016; Chong, Leong and Lim, 2021). One of the most remarkable advantages of magnetophoresis of MNPs in

the real time separation process is due to the high surface area-to-volume ratio of MNPs for the tagging of targeted substance, such that the quantity of MNP material needed for the separation process can be minimized (Gupta and Wells, 2004). Furthermore, this technique is more environment sustainable in term of material efficiency, in which MNPs can be reused/regenerated for subsequent operations due to their high reusability (de Las Cuevas, Faraudo and Camacho, 2008; Toh et al., 2012). Additionally, the feasibility of magnetic separation has been significantly enhanced by the utilization of superparamagnetic nanoparticle, due to its highly tunable magnetic property and excellent specificity in separating a particular targeted entity (Leong et al., 2017).

By looking into the strength of magnetic field gradient employed, magnetic separation of MNPs can be divided into high gradient magnetic separation (HGMS) and low gradient magnetic separation (LGMS) (Leong, Yeap & Lim, 2016). In the past, HGMS (Hatch and Stelter, 2001; Ge et al., 2017) was normally employed for numerous engineering applications, which involves the usage of magnetic field gradient ∇B with magnitude greater than 100 T/m (Moeser et al., 2004; Mariani et al., 2010). In this regard, the high gradient magnetic field can be produced in a column packed with randomly arranged magnetizable wires encompassed by magnetic arrays. The magnetizable wires will dehomogenize the magnetic field which subsequently generate intense magnetic field gradient that is localized around the wires (Ditsch et al., 2005b; Stephens, Beveridge and Williams, 2012). Then the MNP solution is flowing continuously through the column, so that the MNPs can be trapped on the magnetically susceptible wires and removed from the original solution (Moeser et al., 2004). However, HGMS suffers several disadvantages,

such as: (1) high installation and operating cost (Toh et al., 2012; Chong et al., 2021); (2) difficulty to develop analytical solution to describe the transport behavior owing to the highly randomized and non-uniform magnetic field in the column (Leong, Ahmad and Lim, 2015); (3) high maintenance cost due to the MNP deposition on the magnetizable wires (Toh et al., 2012).

In this regard, an alternative strategy has been given more attention recently, namely LGMS (Yavuz et al., 2006). By using LGMS technique, a lower magnetic field gradient ($\nabla B < 100$ T/m) (Yavuz et al., 2006; Faraudo et al., 2016) is generated across the MNP solution by an externally applied magnetic field, without the insertion of magnetizable wires into the solution (Corchero and Villaverde, 2009). Such a simple arrangement has greatly reduced the complexity of the process (Leong, Ahmad and Lim, 2015). Despite of its low driving magnetophoretic force (owing to the low magnetic field gradient), various researchers have revealed that LGMS is capable to remove MNPs suspended in the solution within a reasonable timescale (Leong, Ahmad and Lim, 2015; Sun et al., 2019). For instance, by referring to the work reported by De Las Cuevas and coworkers, the collection of MNPs (with diameter as tiny as 200 nm) can be accomplished within 60 seconds under low magnetic field gradient (de Las Cuevas, Faraudo and Camacho, 2008). The relatively rapid separation of MNPs under LGMS mode is due to the cooperative effect of MNPs (spontaneous self-aggregation of MNPs) upon exposure to the external magnetic field (de Las Cuevas, Faraudo and Camacho, 2008; Andreu, Camacho and Faraudo, 2011; Leong et al., 2020). With the larger magnetic volume, MNP aggregates experience larger magnetophoretic

force that is sufficient to induce rapid separation of MNPs from the solution (Andreu et al., 2012b; Faraudo et al., 2016).

Apart from cooperative effect, recent research works also have shown that the hydrodynamic effect (transfer of momentum between the MNPs and the surrounding fluid) is able to accelerate the separation of MNPs under low magnetic field gradient. Owing to the hydrodynamic effect, magnetophoresis induced convection is generated within the MNP solution subjected to LGMS, which subsequently causes the continuous agitation/distribution of MNPs within the solution throughout the entire process (Leong, Ahmad and Lim, 2015; Leong et al., 2017). Such an induced convection can spread relatively faster to the far end region of MNP solution where magnetic field gradient is very low, which in turn causes MNPs initially located at that region to be swept towards the magnets and being collected in a more rapid manner.

As compared to HGMS, LGMS technology is relatively new and only demonstrated excellent separation efficiency in laboratory experiments carried out in a batchwise mode. However, in term sustainability, LGMS technology (which requires only a simple setup and handheld permanent magnet) has outperformed the HGMS technology (which involves more complex column setup and consumes a lot of electrical energy to power up the electromagnet). In addition, powering up the electromagnet in HGMS system also can produce large amount of heat, which causes the HGMS setup to require extra equipment to lower the temperature during the operation. Easy operation, non-invasive nature, cost-effectiveness, and simplicity exhibited by LGMS have caused it to be more a favorable option over HGMS, hence, LGMS has large potential to be emerging as a versatile separation technology for engineering applications.

1.2 Magnetic separation operated under Batchwise and Continuous Modes

Generally, the operation of physicochemical process can be conducted under two different modes: (i) batchwise (BW) mode or (ii) continuous flow (CF) mode. BW mode involves the charging of process fluid into an equipment/container (where is process is being carried out) at the beginning of the operation, which is then being removed when the operation ends. On the other hand, CF mode involves the process fluid that is flowing continuously into or out of the equipment and the process operation is conducted under the fluid flow condition. Most studies on the separation of MNPs from the suspension by using LGMS technique are conducted in BW manner. Here, the LGMS process involves the placement of handheld permanent magnet(s) outside the MNP solution to distally control the particle motion in a non-contact mode so that the MNPs suspended in aqueous solution can drive towards the magnetic source (region with highest magnetic field). While the MNPs are being captured on the container wall adjacent to the magnet and isolated from the solution, the clear solution is being discharged from the container. Under BW configuration, the study on the fundamental behavior of MNPs subjected to magnetophoresis is relatively easier due to the quiescent fluid condition and the effect of forced convective flow can be safely excluded from the analysis. Furthermore, the study on the transport phenomena of MNPs also can be facilitate under the BW operating mode, as the distribution of MNPs in the solution (caused by the magnetophoresis effect) can be visualized more easily (Andreu et al., 2011). In addition, the LGMS experiment in BW mode also can be conducted under homogeneous magnetic gradient so that the

difficulty of developing analytical solutions can be greatly reduced, which subsequently contributes to a better understanding of the magnetophoretic mechanism (Faraudo and Camacho, 2010).

On the other hand, HGMS systems are operated under CF mode, in which the MNP solution is pumped continuously through a column packed with random magnetizable wires and encompassed by an external magnetic field (such as electromagnets (Moeser et al., 2004), permanent magnets (Mariani et al., 2010), or superconducting solenoids (Baik et al., 2010)) as shown in Figure 1.1. Such an operational mode of HGMS enables the automation to be conducted more easily and less labor demanding, as the fluid is being pumped in or out of the column once the operation is initiated, without the requirement of manpower. Owing to this reason, HGMS has been widely implemented in the real time engineering applications. For instance, HGMS technology is used in industrial wastewater treatment such as kaolin purification (Oberteuffer, 1974), removal of phosphate from water (Shaikh and Dixit, 1992), separation of the dissolved heavy metals from wastewater (Terashima, Ozaki and Sekine, 1986) and removal of the oil and suspended solids from municipal sewage (Ying, Yiacoumi and Tsouris, 2000). Furthermore, HGMS also have been applied in the removal of biological substances from the wastewater, such as algae (Toh et al., 2012), cells (Šafařík and Šafaříková, 1999) and yeast (Dauer and Dunlop, 1991).

Due to its CF operational mode, HGMS can be conducted in large scale industry for the separation of targeted materials (Gómez-Pastora et al., 2017). The design of HGMS allows certain variations in feed conditions without the requirement for manual adjustment before sending to the HGMS column. The

dimension of HGMS column can be scaled up, which allows large volume of solution to continuously flow through the separation column and accelerate the separation process. For instance, Oberteuffer reported that HGMS with resistive solenoid or toroidal electromagnets is able to separate the fluid in volumes as high as 10 m^3 within an hour (Oberteuffer, 1974).

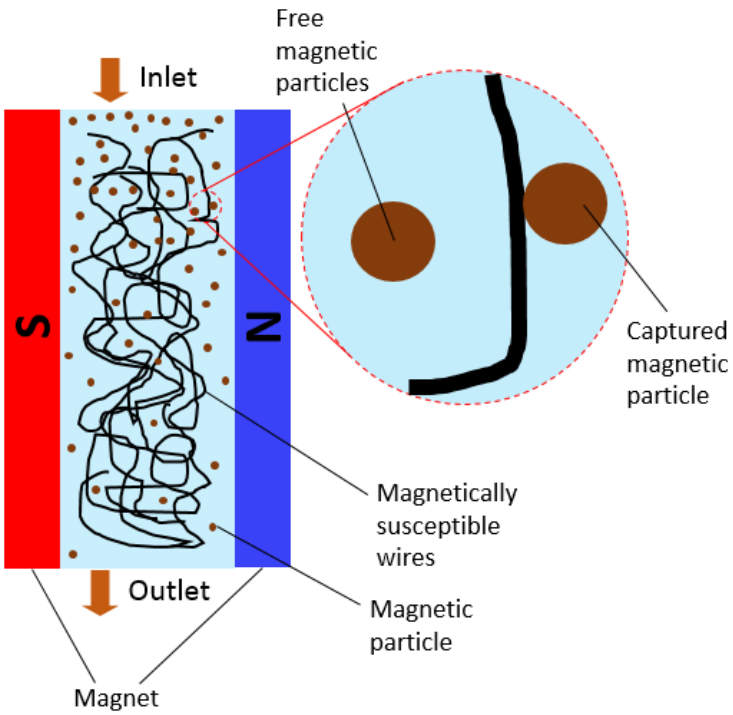

Figure 1.1: Illustration of HGMS column (Leong, Yeap and Lim, 2016)**.**

1.3 Mathematical Modelling on the kinetics of magnetophoresis process

In order to design magnetic separator and optimize its performance, it is crucial to understand the underlying physics of MNPs subjected to magnetophoresis. The understanding on the physics of it is accompanied by the establishment of mathematical model that is able to describe the magnetophoresis process up to

great accuracy. To dates, the development of mathematical model to depict the dynamical behavior of magnetophoresis kinetics are growing rapidly (de Las Cuevas, Faraudo and Camacho, 2008; Helseth and Skodvin, 2009; Andreu et al., 2011). In this context, the magnetophoresis kinetics are studied by recording the transient evolution of several parameters (such as MNP concentration, flow velocity, etc.) under the influence of the magnetic field (Schaller et al., 2008). Here, the kinetics of magnetophoresis process can be expressed in term velocity or concentration profile of MNP solution with respect to time after the magnetophoresis has been initiated. Then, it is desirable to construct a mathematical model that is able to duplicate the real time concentration as well as velocity profiles that are measured experimentally. The ability to predict the kinetics of magnetophoretic separations is particularly important in designing and optimizing magnetic separators for real-time engineering applications.

The very first modelling of magnetophoresis process (classical magnetophoresis model) assumes that all MNPs move individually (or non-cooperatively) and penetrate through a fluid that is always in stationary state. Here, it has been assumed that the entire body of fluid is unaffected by the motion of the MNPs within the fluid (Schaller et al., 2008; Andreu et al., 2011). Later, it has been revealed that the aggregation of MNP is significant and non-negligible in many real-time magnetophoretic applications (especially for MNP systems with higher concentration or larger particles size), which subsequently motivates the incorporation of particle aggregation effect into the mathematical model (Yavuz et al., 2006). The aggregation process can alter the separation kinetics significantly, whereas the formation of long chains of MNP aggregates

can move rapidly during magnetophoresis, which subsequently improves the separation of MNP solution in the presence of external magnetic field. Therefore, the modification of classical non-interacting magnetophoresis model by incorporating the cooperative effect has been carried out by few researchers. For instance, by referring to the work reported by Schaller and coworkers the prediction of mathematical models for the dynamics of one-dimensional magnetophoresis process was introduced with the assumption of MNP aggregation during migration of MNPs throughout magnetophoresis (Schaller et al., 2008). Moreover, De Las Cuevas and coworkers established a simple experimental model to relate the separation time of MNPs to concentration and magnetic Bjerrum length of MNPs, by considering the particle-particle interaction that occurs during cooperative magnetophoresis (de Las Cuevas, Faraudo and Camacho, 2008).

Apart from that, the dynamical behavior of magnetophoretic process has been discovered to be influenced by hydrodynamic effects, thus, there is a need to incorporate this effect into the mathematical modelling to predict its kinetics. For instance, as demonstrated by Leong and coworkers in their experiments, circulating convection flow was observed in the MNP solution upon exposure to magnetic field (Leong, Ahmad and Lim, 2015). Here, the experimental results indicated that the induced convection generates the continuous homogeneity throughout the entire MNP solution during the magnetophoresis, which is contradictory with the results that predicted by the classical model without incorporating the effect of hydrodynamic. After considering hydrodynamic effect in the mathematical model (using Navier-Stokes equations to address the effect of momentum transfer), the occurrence

of convective current and homogeneity of MNP solution can be observed in the simulation results of the magnetophoresis process, which is consistent with the experimental observation. Similar to cooperative effect, the magnetophoretic separation rate of LGMS can also be enhanced by hydrodynamic effect, according to both experimental and simulation results.

1.4 Problem Statement

As reported in the earlier research works, the role of MNPs as the scavenger of targeted substance has proven to be feasible in various engineering applications, which is ranging from environmental treatment to biomedical field. In this regard, it is essential to design a separation scheme that is able to conduct the isolation of MNPs more conveniently. However, most studies related to LGMS were conducted at benchtop in BW manner with small scale, which commonly involves a permanent handheld magnet located outside a container (with dimension of few centimeters) filling with MNP solution. This separation strategy is not appropriate to be implemented at industry scale as the MNP separation can only be effectively conducted in small scale (with length scale of the order to 10^{-3} – 10^{-2} m). In addition, as the operational principle is ill-defined with batch or semi-batch implementation that usually involves high level of manual adjustment/intervention and demanding labor power (Lee et al., 2015). Furthermore, BW magnetic separation has difficulties in automating the process and operating it remotely, which is in contradiction to the current trend of the latest industrial revolution that encourages the implementation of

automation systems in the production lines. If scaling up the LGMS process in a BW mode, it requires a large quantity of separation vessels and materials, as a result, it involves a great demand for labor to manipulate the charging and discharging of solution in/out of the separation vessels as well as to monitor the separation process. Due to the mentioned disadvantages, it is not a suitable strategy for LGMS system under BW mode to be extended into large scale engineering applications.

In this regard, it is appealing to integrate the CF feature of HGMS into the LGMS system, in order to facilitate the real-time application of this separation technique. Here, the low gradient magnetic separator is operated under continuous flow (CF-LGMS) with the MNP solution being pumped through the separator column that is surrounded by permanent magnets where the separation of MNPs from the suspension is conducted simultaneously. In contrast to the BW-LGMS that involves the magnetophoresis of MNPs under the fluid without any forced convection, the separation of MNPs is performed under the presence of forced convection (the flow of MNP solution generated by a pumping system) for the CF-LGMS process. Such setup is operational without the requirement of high labor force investment. Besides, by utilizing the LGMS concept, the CF magnetic separator does not require the installation of wires inside the column, therefore, the main limitation of HGMS can be avoided. Furthermore, as the estimation of magnetic fields generated by the magnets within the LGMS column (without the random magnetizable wires as found in the HGMS column) is relatively easier, such an operational setup can greatly simplify the modelling and optimization of the magnetic separation process.

However, the information related on the transport phenomena as well as the dynamical behavior of CF-LGMS (with the length scale ranging from 10^{-2} m to 10^{-1} m, which is a transition length scale from microscale to the large scale of magnetic separation) in the current literature is still lacking and remained largely unexplored. Owing to this reason, it is important to elucidate the transport mechanism of MNPs subjected to CF-LGMS process, which is necessary for making accurate assumptions in the development of a mathematical model to depict the kinetics of this process. Furthermore, it is also essential to identify the effect of several design parameters of magnetic separator, including (i) spatial distributions of magnetic field (Khashan and Furlani, 2013; 2014), (ii) MNP concentration, and (iii) MNP solution flowrate, on its separation efficiency to provide some insights in the design of the separator for practical use in the future.

Hence, mathematical models that describe the transport behavior of MNPs subjected to magnetophoresis under BW and CF modes are to be proposed in this study, and the accuracy of these mathematical models in predicting the real time CF-LGMS processes is examined by comparing the simulation results with experimental findings. From such comparison, the dominating transport mechanism that governs the CF-LGMS process is identified. The MNP separation efficiency resulted from the CF-LGMS experiments under different operating conditions is then compared with the simulation result generated by the CF-LGMS mathematical model to be developed in this study. It is anticipated that with the understanding on the working principle of CF-LGMS and the development of mathematical model, a

new design rule for magnetic separation operated under CF-LGMS can be further established.

1.5 Objectives of the Research

The objectives in this study are:

- To characterize the unmodified magnetic nanoparticles (MNPs) as well as PSS-functionalized-MNPs used in this study.
- To elucidate the transport mechanism of MNPs subjected to low gradient magnetic separation (LGMS) conducted under batchwise (BW) and continuous flow (CF) manners.
- To evaluate the effect of magnets arrangement, MNP concentration, MNP solution flowrate on the separation efficiency of the CF-LGMS process.
- To develop a mathematical model to depict the dynamical behavior of low gradient magnetophoresis of MNPs under CF mode.
- To verify the feasibility of implementing the CF-LGMS process in real time application to achieve high separation efficiency.

CHAPTER TWO

LITERATURE REVIEW

This chapter is elaborated the discussion and summary of published report correlated to this study. Firstly, the magnetic separation technology is reviewed with the historical development of magnetic separation technology, brief introduction to magnetic nanoparticles (MNPs) and magnetophoresis process in Section 2.1. Next, the detail of applications of MNPs in the engineering-related fields is demonstrated in Section 2.2. Next, Section 2.3 discusses the physical phenomena that exert significant impact on the transport behavior of MNPs subjected magnetophoresis, such as Brownian motion, cooperative effect, and hydrodynamic effect. Then, several magnetic separation strategies are demonstrated in Section 2.4, which includes convectional magnetic separators as well as the principles of HGMS and LGMS to separate MNPs from the solution. Lastly, the effect of several parameters on the separation efficiency of magnetic separation conducted under CF mode is briefly discussed in Section 2.5.

2.1 Magnetism and Magnetic Separation

In this section, some general information related to magnetic separation is discussed. Firstly, the brief history of the development of magnetic separation

technology is reviewed. Next, the magnetic properties of the MNPs as well as their role in magnetic separation are demonstrated. Finally, this section ends with the discussion of a physical phenomenon that is essential in the magnetic separation of MNPs, namely magnetophoresis.

2.1.1 History of the Magnetic Separation

The application of magnetism in separation processes have been discovered to be feasible in a variety of industrial applications, which are particularly useful for separating magnetic materials from non-magnetic materials. Generally, the implementation of magnetism in separating objects with different magnetic property is known as magnetic separation, which is usually aided by a magnetic force acting on them upon exposure to an external magnetic field (generated by electromagnet or permanent magnet).

In the 1792, William Fullerton was granted a patent describing a method for separating iron ore using magnetic attraction, which is the pioneer of the application of magnetic separation in the mining industry (Gunther, 1909; Yavuz et al., 2009). Furthermore, in the mid-1800s, an English scientist, Michael Faraday has discovered that the difference in magnetic susceptibility of the materials would allow them to be effectively separated under an externally applied magnetic field (Bronkala, 2000). Since then, many US patents on magnetic separation have been developed, which usually involve the application of this technique in mineral processing (Parker, 1977). For instance, most of the applications of magnetic separation in early stages involved the

removal of tramp iron and the concentration of iron ore (Morgan and Bronkala, 1993). The conventional magnetic separation equipment can only be used for separating materials with a high magnetic response (such as iron and magnetite) (Oberteuffer, 1974). Over the years, numerous different varieties of mechanical design equipment (magnetic pulleys, grate magnets, magnetic drum separators, high-intensity cross belt etc.) have been developed, which extending its functionality and application in other fields (Bronkala, 2000). In last few decades, magnetic separation has been increasingly employed for the purification of kaolin clay (Oberteuffer et al., 1975), wastewater treatment (Mariani et al., 2010; Zeng et al., 2015), mining (Kelland, 1973), petroleum processing (Jeong et al., 1982; Friedman and Yellen, 2005) and the chemical industry (Cieśla, 2003).

In the 1950s, high gradient magnetic separation (HGMS) technology was developed to separate the paramagnetic materials with lower magnetic susceptibility and smaller size (from micron up to nano-sized particles) from non-magnetic fluid (Oberteuffer, 1973). Such a HGMS system can maximize the magnetic field gradient by combining a strong magnetic field and a magnetic matrix (Gómez-Pastora et al., 2017). In the HGMS process, a column filled with a magnetically susceptible wire is able to create extremely localized and high magnetic field gradient under the presence of external magnetic field (> 100 T/m), which can separate the weaker paramagnetic particles of smaller size from the solution (Oberteuffer, 1973). This technology improves the magnetic separation technique by expanding its feasibility towards the separation of particulate matters that are weakly magnetic susceptible (Yavuz et al., 2009). To date, HGMS technique has been well established and it is widely used to

remove fine iron impurities in various fluids as well as integrated into the wastewater treatment system (Gómez-Pastora et al., 2017).

Further on, the magnetic separation operated under low gradient magnetic field (< 100 T/m) was discovered to produce attractive results in terms of economic potential as well as the separation efficiency in comparison to HGMS (Yavuz et al., 2006; de Las Cuevas, Faraudo and Camacho, 2008; Lim et al., 2012). This magnetic separation scheme is known as low gradient magnetic separation (LGMS). In this context, LGMS system only requires handheld permanent magnet(s) to induce the separation of targeted particles from the solution, which causes it to be a simple and cost-effective method for engineering application. Yavuz and coworkers have demonstrated the feasibility of LGMS in the separation arsenic from water by using monodisperse iron oxide nanocrystals under low magnetic field gradient generated by a handheld permanent magnet (Yavuz et al., 2006). The success of LGMS is due to the ability of MNPs to perform self-aggregation in the presence of an external magnetic field and followed by the formation of larger size aggregates that experience sufficiently high magnetic force even under a low magnetic field gradient (de Las Cuevas, Faraudo and Camacho, 2008; Andreu, Camacho and Faraudo, 2011; Faraudo, Andreu and Camacho, 2013). In fact, as shown in various experiments, LGMS is proven to have vast potential in real time applications, ranging from microscale biomedical technology to large-scale environmental treatment such as water purification and pollutant removal. In the biomedical application, LGMS can be utilized for cell isolation and diagnosing diseases such as separation of mouse macrophages, human ovarian cancer (HeLa) cells (Pamme and Wilhelm, 2006),

Salmonella enterica (Chen et al., 2015), biotinylated substrate, prostate cancer cells and leukemia cells (Song et al., 2011; Leong, Yeap and Lim, 2016), as well as red blood cells and lymphoid cells (Zborowski et al., 2003). In addition, the concepts of LGMS were also applied in gene and drug delivery applications (Dobson, 2006; de Jong, 2008; Lee, Kim and Cheon, 2013). In the environmental treatment, the coupling of MNPs and LGMS technology has demonstrated great potential in the removal of organic pollutant (Che et al., 2014), heavy metals (Kim et al., 2013), microalgae (Lim et al., 2012), dye (Long, Xiao and Cao, 2017; Zirak et al., 2018) and etc.

2.1.2 Fundamental of Magnetism of Magnetic Materials

Since some fundamentals of magnetism theory is crucial and closely related to the magnetic separation process, it is presented in this subsection. Typically, in a magnetic separation process, magnetic field are generated by the movement of charged particles within a material which is measured by a physical quantity, denoted as the magnetic field strength, $\vec{H}$ (Am^{-1}). When any magnetic responsive material is exposed to an external magnetic field, it will show some responses toward it with the induction of magnetic flux density, $\vec{B}$ within the material. The relationship between the magnetic field strength and magnetic flux density in the free space (vacuum or air) is expressed by following equation (Hatch and Stelter, 2001):

$$\vec{B} = \mu_0 \vec{H} \qquad (2.1)$$

where μ_0 is magnetic permeability of free space that equal to $4\pi \times 10^{-7}\, m \cdot kg/(s^2 \cdot A^2)$.

On the other hand, within a magnetic material, the magnetic flux density is dependent on two factors: (1) magnetic flux density in the free space where the material is located, (2) the magnetization of the material by applied magnetic field, as shown in the following equation (Svoboda, 2004):

$$\vec{B} = \mu_0 \vec{H} + \mu_0 \vec{M} = \mu_0 (\vec{H} + \vec{M}) \tag{2.2}$$

Here $\vec{M}$ is the volumetric magnetization of the magnetic material by the applied field. Again, the volumetric magnetization can be defined as the magnetic dipole moment, $\vec{\mu}$ per unit volume, V of magnetic material (Hatch and Stelter, 2001):

$$\vec{M} = \frac{\vec{\mu}}{V} \tag{2.3}$$

Under the weak magnetic field, the volumetric magnetization of the magnetic material is linearly dependent on the magnetic field strength (when the magnetization is very far from its saturation magnetization), which is shown in the following equation (Hatch and Stelter, 2001):

$$\vec{M} = \chi \vec{H} \tag{2.4}$$

where χ is the magnetic susceptibility of the magnetic material. According to the magnitude of magnetic susceptibility, the magnetic material can be classified into various types such as ferromagnetic, ferrimagnetic, antiferromagnetic, diamagnetic, and paramagnetic (Pamme, 2006).

However, the volumetric magnetization of magnetic material does not increase unlimitedly with the strength of the magnetic field as it has a

saturation value. When the magnetic field strength is sufficiently high, the volumetric magnetization will approach its peak value and further increase in magnetic field strength will not be able to boost the volumetric magnetization to higher values (Chong, Leong and Lim, 2021). In this case, the material is denoted as being completely magnetized, which indicates all the magnetic dipole moments within the material are perfectly aligned with the magnetic field and the material has achieved magnetic saturation. The volumetric magnetization of magnetic material in a saturated state is known as saturation magnetization, $\overrightarrow{M_s}$, which differs greatly for different materials (Jordens et al., 2014).

2.1.3 Magnetic Nanoparticles

The implementation of HGMS and LGMS in engineering applications is often accompanied by magnetic nanoparticles (MNPs), due to their intrinsic magnetic properties that cause them to be able to be remotely manipulated by magnetic fields. MNPs are made of magnetic responsive material which typically have the average size ranging from 1-100 nm in diameter and it can be appeared in various shape (such as spheroid shaped particles, rod-shaped particles, needle-like shaped particles and etc.) (Singh, Srivastava and Singh, 2017). One of the examples of the transmission electron microscopy (TEM) image is shown in Figure 2.1.

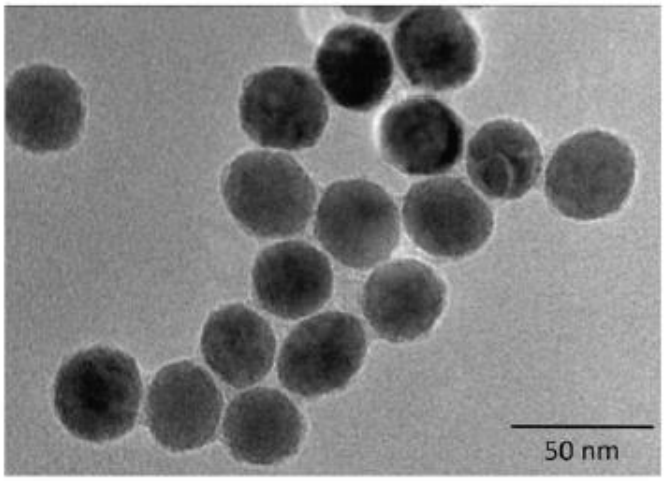

Figure 2.1: Transmission Electron Microscopy (TEM) images of MNPs (Leong et al., 2017)**.**

The nano size of MNPs enables them to possess a relatively high surface area to volume ratio, which causes them to exhibit very distinctive chemical and physical properties as compared to their bulk counterparts (Ali et al., 2021). With the huge surface area, the total mass of particles needed for the various surface activities (such as adsorption and reaction) in engineering application will be greatly decreased (Mohammed et al., 2017). For instance, according to the work reported by Lin and coworkers, when the size of nanoparticles is reduced from 500 nm to 100 nm, the reactivity of nZVI nanoparticles increased by approximately 50 to 90 times (Lin, Weng and Chen, 2008). Additionally, Shen and coworkers have demonstrated in their experimental work that the adsorption capacity of 8 nm nanoparticles is 7 times higher as compared to 50 nm nanoparticles (Shen et al., 2009). Thus, nano-sized particles with unique properties of high surface area to volume ratio has imposed excellent adsorption capacity/reactivity towards them, which in turn renders them to be more appealing as compared to mesoporous particles.

Moreover, MNPs exhibit a unique property known as superparamagnetism, in which each MNP is sufficiently small to be made up of only a single magnetic domain. Owing to this feature, the magnetic dipole moment of MNPs can freely rotate and it is easily aligned with the direction of the externally applied magnetic field. Thus, when the MNPs are exposed to an external magnetic field, the dipole moments will align in the direction of the magnetic field (Figure 2.2).

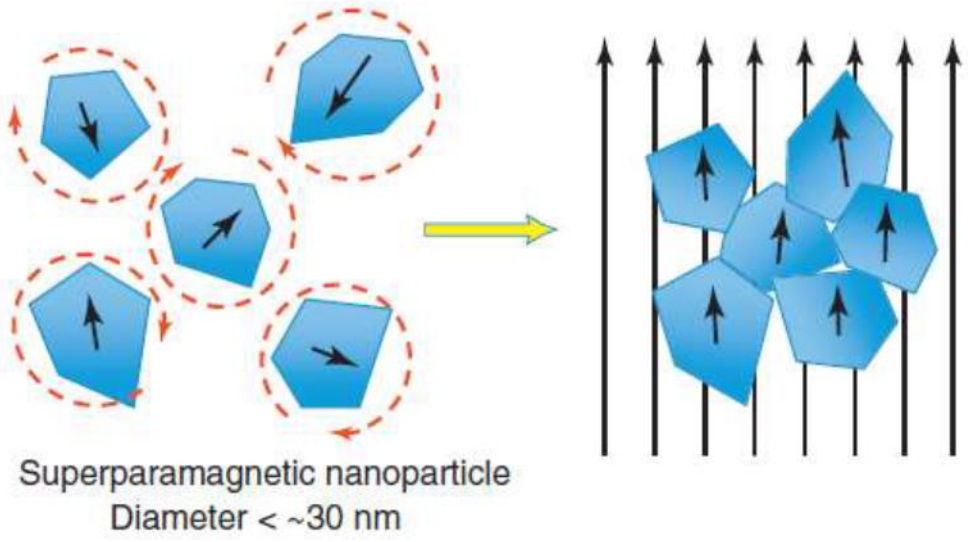

Figure 2.2: Microscopic structure of superparamagnetic material under the absence and presence of magnetic field, *H* (Ahmed and Abdel, 2016)**.**

Once the external magnetic field is removed, the uniform arrangement of the dipole moments is disrupted and randomized by the thermal energy. If the measurement duration of magnetization of the superparamagnetic nanoparticles is much longer than the Neel relaxation time (the time internal between the subsequent flip of the magnetic dipole moment induced by the thermal effect), the measured magnetization appears to be zero. Therefore, superparamagnetic nanoparticles are also behaving as paramagnetic material,

in which they exhibit zero remanent magnetization under the absence of an external magnetic field. In other words, MNP with superparamagnetic property does not possess any magnetic memory. Due to this unique magnetic property of MNPs, the magnetic effect (magnetization) of MNP can be turned on/off by manipulating the magnetic field imposed on it.

Nevertheless, unmodified MNPs (without any material immobilized on surface) has several limitations that restrict its practicability for real-time applications such as poor biocompatibility, lack of chemical instability in physiological environment as well as low colloidal stability and prone to agglomeration in a short period of time. Such disadvantages significantly affect the performance/efficiency of MNPs in various applications such as water purification efficiency (Yeap et al., 2012). Unmodified MNPs are susceptible to rapid aggregation (Phenrat et al., 2007) due to the van der Waals and magnetic dipole-dipole attraction between particles (Lim, Majetich and Tilton, 2009) as well as the tendency of nanomaterials to reduce their surface energy (Ditsch et al., 2005a). As compared to non-aggregated MNPs, the exposed surface area of MNP clusters is relatively small, which reduces their adsorption capacity and catalytic reactivity (Schrick et al., 2004). In such cases, polyelectrolyte is usually used for the surface functionalization/modification of MNPs prior to their applications (Yeap et al., 2012). The surface coating introduces the electrostatic repulsion between particles and provides physical barrier (or so-called steric repulsion) to overcome the short-range interparticle attractive interactions (Seebergh and Berg, 1994; Runkana, Somasundaran and Kapur, 2006). Several examples of coated MNPs that have been used in various research are shown in Table 2.1.

Table 2.1: Types of coated materials on the MNPs and their application.

Coating Material	**Particles Size**	**Particle magnetization (Am^2/kg)**	**Application**	**References**
Poly(diallyldimethylammonium chloride) (PDDA)	d_H = 474.4 nm	113.8	Removal of microalgae	(Toh et al., 2012)
	64.4 nm d_H = 107.4 nm	71	Removal of microalgae, *Chlorella sp.*	(Lim et al., 2012)
Amine	d_H = 66 nm	90	Removal of oil droplet	(Ko et al., 2017)
Polyethylene glycol diacid	20 nm	47.6	Act as agent in magnetic resonance imaging (MRI)	(Feng et al., 2008)
cis-diamminedichloroplatinum(II) (cisplatin)	d_H = 250 nm	32.5	Used in controlled drug release	(Babincova et al., 2008)
Pyrimidine-2,4-diamine	20-35 nm	15	Synthesis of pharmaceutical products	(Taheri-Ledari, Rahimi and Maleki, 2019)
Poly(2-vinyl-4,4-dimethylazlactone)	12.4 nm	53.6	Act as enzyme immobilization carriers	(Mu et al., 2014)
cyclodextrin	20 nm	66	delivery of a hydrophobic drug	(Oroujeni et al., 2018)
polyvinyl alcohol (PVA)	~10 nm	41.78	delivery of 5-Fu	(Aliabadi, Shagholani and Yunessnia lehi, 2017)

2.1.4 Magnetophoresis

The magnetic separation process (for either HGMS or LGMS) involves the motion of MNPs in the solution that are controlled by external magnetic field under a non-contact/non-invasive mode. This process is commonly known as magnetophoresis of the MNPs (Lim et al., 2014). The motion of MNPs under magnetic field is mainly dictated by two main forces: (i) magnetic force and (ii) viscous drag force.

Under the presence of inhomogeneous/non-uniform external magnetic field, MNPs experience magnetic force which can be formulated as follows (Mariani et al., 2010):

$$\overrightarrow{F_{mag}} = \mu \nabla \vec{B} \tag{2.5}$$

where μ is the magnetic dipole moment of MNP, $\nabla \vec{B}$ is the magnetic field gradient. If the magnetic particle is spherical in shape, it can be evaluated as follow (de Las Cuevas, Faraudo and Camacho, 2008):

$$\overrightarrow{F_{mag}} = \frac{\pi {d_p}^3}{6} M_{p,m} \nabla \vec{B} \tag{2.6}$$

Here $M_{p,m}$ is the mass magnetization of MNPs (defined as magnetic dipole moment per unit mass) and d_p is the core diameter of MNPs. For the special case in which the external magnetic field is created by a cylindrical permanent magnet, the magnetic flux density *B* along the symmetry axis is formulated as follow (Schaller et al., 2008):

$$B = \frac{B_r}{2}\left[\frac{y+h}{\sqrt{(y+h)^2 + r^2}} - \frac{y}{\sqrt{y^2 + r^2}}\right] \tag{2.7}$$

where h and r are the length and radius of the magnet, respectively and the B_r is the remanent magnetization of the magnet. Here, y is the distance from the magnet pole along the symmetrical axis. During magnetophoresis, the inhomogeneous magnetic field is playing the following roles to induce the motion of MNPs: (i) it magnetizes the MNPs and causes them to acquire magnetic dipole moment (μ) or magnetization, and (ii) it generates magnetic field gradient $\nabla\vec{B}$ which impose the magnetic force on the particle (see Equation (2.5)). Based on Equation (2.5), the magnetic force experienced by the MNPs is directed in the same directions as the magnetic field gradient, which means that the magnetic force exerting on MNPs is pointing towards the region with the highest rate of increase of the B value.

The second force that plays a crucial role in dictating the dynamics of MNPs during magnetophoresis is viscous drag force, which is originated from the friction that resists the relative motion of MNPs with respect to the surrounding fluid (Warren L. McCabe, Julian C. Smith and Peter Harriott, 2018):

$$\overrightarrow{F_d} = -3\pi\eta\, d_H\, \overrightarrow{v_p} \tag{2.8}$$

Here, η is the viscosity of surrounding fluid, d_H is the hydrodynamic diameter of MNP, $\overrightarrow{v_p}$ is the magnetophoretic velocity of MNP. This equation is only valid for the spherical particle under the condition that the surrounding fluid is not moving. If the magnetophoresis of MNPs is conducted under a flowing fluid, Equation (2.8) should be modified and the viscous drag force is formulated as follows (Binder et al., 2006):

$$\overrightarrow{F_d} = -3\pi\eta d_H(\overrightarrow{v_p} - \overrightarrow{v_f}) \quad (2.9)$$

where $\overrightarrow{v_f}$ is the fluid velocity. The negative sign in Equations (2.8) and (2.9) indicates that the drag force is directed in the opposite direction of the particle velocity.

Thus, the total force applied on a MNP during magnetophoresis is computed by the addition of $\overrightarrow{F_{mag}}$ and $\overrightarrow{F_d}$:

$$\overrightarrow{\sum F} = m_p\vec{a} = \overrightarrow{F_{mag}} + \overrightarrow{F_d} \quad (2.10)$$

where $\vec{a}$ is the acceleration of MNP. It should be noted that the gravitational force is relatively very small in magnitude (due to the employment of nanometer-sized MNPs) as compared to magnetic and viscous drag forces, it is being ignored in Equation (2.10) (Leong, Ahmad and Lim, 2015). Also, it should be recalled that the acceleration term is often negligible for the creeping flow under a low Reynold number environment (which is the case for the magnetophoresis of MNPs), therefore, further rearrangement of Equation (2.10) results in (Chong et al., 2021):

$$\overrightarrow{F_{mag}} = -\overrightarrow{F_d} \quad (2.11)$$

After incorporating Equations (2.6) and (2.7) into equation (2.11), some mathematical rearrangement can lead to:

$$\overrightarrow{v_p} = -\frac{m_p}{3\pi\eta d_H} M_{p,m}\nabla\vec{B} = -\frac{\mu}{3\pi\eta d_H}\nabla\vec{B} \quad (2.12)$$

Equation (2.12) is showing the magnetophoretic velocity of MNPs within a stagnant fluid. Conceptually, the magnetophoretic velocity of the MNPs can be

controlled by manipulating the field gradient of the external magnetic field. For instance, Tham and coworkers found out that the monodispersed iron oxide nanoparticles achieved a magnetophoretic velocity around 71 μm/s under the field gradient of 93.8 T/m. However, under a lower magnetic field gradient (~13.0 T/m), the magnetophoretic velocity of MNPs has remarkably declined to around 7.8 μm/s (Tham et al., 2021). Yet, due to the relatively small size of MNPs, the viscous drag force and Brownian motion can potentially impose a significant effect in prohibiting their deterministic motion induced by the magnetic field. In this context, the motion of MNPs can be very slow (huge viscous drag force in relative to magnetic force) and being randomized by the thermal effect, which causes the manipulation of MNPs to be extremely challenging. Hence, in order to overcome those opposing factors, extremely high magnetic field gradient is required as the magnitude of magnetic force experienced by the MNPs is directly proportional to the applied magnetic field gradient, $\nabla\vec{B}$ as shown in Equation (2.5).

2.2 Application of Magnetic Nanoparticles

Due to the unique characteristics of MNPs (such as high ratio of surface area to volume, superparamagnetic, fast absorption kinetics and etc.), the magnetophoresis of MNPs has been revealed to be highly feasible in a variety of engineering applications such as biomedical/biotechnology field, environmental treatment, and etc. The details applications of MNPs in biomedical field as well as water remediation is outlined in this section.

2.2.1 Biomedical Applications

In the biotechnology field, magnetic separation scheme is found to be useful in repairing tissue, purifying cells, controlled delivery of drugs or biomaterials, detoxification, detection of diseases and contrast agents in magnetic resonance imaging (MRI) (Berensmeier, 2006; Sun, Lee and Zhang, 2008). In bioscience and biomedical studies, MNPs are used to target, manipulate, isolate, and separate the specific molecules such as cells, enzymes, proteins, antigens, and DNA. The multifunctionality of MNP in biomedical separation processes is due to its unique size, easy processability, promising separation scheme, good dispersibility and also exhibit the ability to enhance the proton relaxation of particular tissues, which renders cell separation, immunoprecipitation, protein purification, as well as RNA/DNA extraction to be highly efficient (Salmani, Hashemian and Khandan, 2020). Intensive research and experiments have allowed the selective and controlled transport of target cells by MNPs, in the presence of magnetic field gradient.

One of the well-known applications of magnetic separation in biomedicine is magnetic disease targeting, which is used to detect vascular defects (Chorny et al., 2011), tumors (Song et al., 2011), malaria (Ngo et al., 2016), cancer (Kang et al., 2017), and other localized pathologies. This detection can be rapid and highly accurate, which is usually accompanied by the detection of targeted biological components in the blood. As most of the targeted biological components (bacteria, viruses, and pathogens) are non-magnetic (Lien et al., 2007; Chen et al., 2010), they must be labeled with surface-modified MNP through attachment by specific functional groups (Rezayan et al., 2016; Mashhadi Malekzadeh et al., 2017). The MNP-labelled target entity or infectious agent can be magnetically separated for clinical diagnosis of a particular disease. The disease diagnosis by MNPs is extremely appealing because it can provide patients with accurate detection and simple medical evaluation.

Furthermore, there are numerous biomedical diagnostic applications that have adopted the LGMS concept in their operations and have produced excellent results. For instance, in the detection of cancer by using magnetic separation, the mixture of monocytes and macrophages can be successfully separated within a free-flowing magnetophoresis chip where the permanent magnet was employed (with $\nabla\vec{B}$ ~30–80 T/m), which results in excellent throughput (10 – 100 cells/s) and high purification (>88%) (Robert et al., 2011). In addition to this, as demonstrated by Xu and coworkers, SuperMag^{TM} separator (Ocean NanoTech) (with $\nabla\vec{B}$ ~ 100 T/m) can be employed to isolate the tumor cells from fresh whole blood and gives rise to an enrichment factor (ratio of cancer cells to normal cells) as high as 1:10,000,000 (Xu et al., 2011).

Moreover, Song and coworkers developed the magnetic scaffold with low magnetic field gradient ($\nabla\vec{B}$ < 100 T/m) for the detection and isolation of the individual target cell from analytical samples (Song et al., 2011). According to the given experimental condition, the magnetophoretic capture efficiencies of prostate cancer cells and leukemia cells can achieve up to 97% and 96%, respectively.

In addition, with the advancement of nanotechnology in the biomedical treatment, MNPs also play an important role in the treatment of tumor in a process known as hyperthermia (Moy and Tunnell, 2017). During the hyperthermia process, large dose of MNPs is injected into the tumor cells and then exposed to external fluctuating magnetic field to induce the vibrational motion of the MNPs in the tumor cells. Consequently, heat will be produced by the high frequency vibration of the MNPs within unresectable tumor which subsequently causes the tumor cells to be destroyed and killed (Kolosnjaj-Tabi and Wilhelm, 2017).

2.2.2 Waste Removal and Water Treatment

In wastewater treatment, the pollutants to be removed usually consist of a variety of organic and inorganic compounds. Therefore, a strong reducing agent (such as MNP) is incredibly beneficial in the process of degrading pollutants during wastewater treatment. Furthermore, MNPs exhibit excellent efficiency in removing contaminants or hazardous waste from wastewater by adsorbing the harmful substances on its surface due to the high adsorption

capacity of the MNPs which exhibits the large surface-area-to-volume ratio (Babaei et al., 2017). The pollutant-loaded MNPs are then removed by externally applied magnetic fields, which subsequently results in a clean and pollutant-free solution.

Up to current stage, it has been widely reported that several heavy metals from aqueous solutions such as chromium (Badruddoza, Bhattarai and Suri, 2017), selenium (Ma et al., 2018), uranium (Calì et al., 2018), lead (Ge et al., 2018), lanthanide (de Melo et al., 2017), cadmium (Chen et al., 2017), mercury (Bao et al., 2017), copper (Bharath et al., 2017; Sahraei, Sekhavat Pour and Ghaemy, 2017), and iron (Meng et al., 2018) can be effectively removed by surface modified MNPs. For instance, Li and coworkers have illustrated that the magnetic separation techniques incorporated with biosorption can be more effective in removing heavy metal ions (Li et al., 2008) as compared to filtration method. This method is an attractive approach for the removal of heavy metal due to the eco-friendly, simple, and low-cost characteristics of this separation technique.

Apart from that, MNPs also can be applied effectively in microalgae removal from water. For instance, Toh and coworkers have successfully removed microalgae from fishpond water (with separation efficiency more than 90%) by attaching the surface-functionalized MNPs with the microalgae through electrostatic interaction and this method can significantly reduce the biological oxygen demand (BOD) of the fishpond water (Toh et al., 2014).

Furthermore, MNPs are also showing great potential in removing oil from water. Typically, large volume of wastewater (contains highly stable

dispersed waste oil) is generated by the oil and gas extraction process in offshore and onshore wells, which typically creates major environmental hazards (Simonsen, Strand and Øye, 2018). Owing to the limitation of space in offshore and onshore wells, the implementation of large equipment to process such a large volume of oil-polluted wastewater is extremely difficult. Such a limitation can be overcome by using MNPs, which are serving as a nano-tool to remove the oil droplet in offshore operation (Elmobarak and Almomani, 2021). As shown in Figure 2.3, when the MNPs are added to oil-in-water emulsion, the positively charged MNPs can absorb or attach to negatively charged oil droplets quickly and efficiently through the electrostatic attraction by the demulsifying effect, which in turn enables the separation of MNPs-attached oil droplets from water by applying an external magnetic field (Kayvani Fard et al., 2016). Nevertheless, the spent MNPs can be regenerated and reused in following cycles, which can contribute to waste reduction and lower down the operating costs.

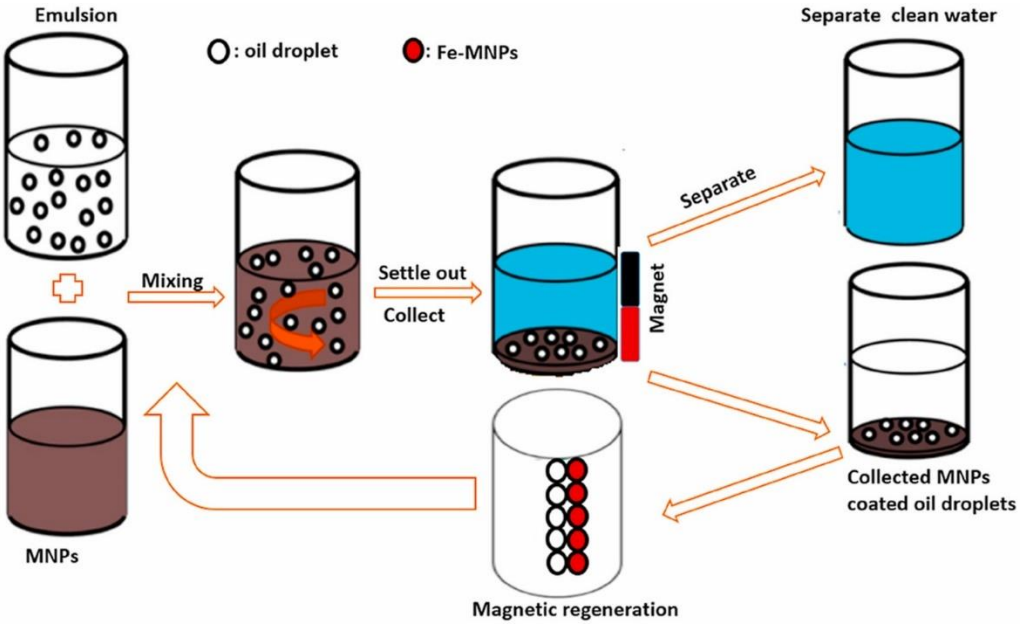

Figure 2.3: The process of removing oil droplet by using MNP (Elmobarak and Almomani, 2021)**.**

2.3 Transport Behavior of MNPs under Magnetophoresis

In this section, the physical phenomena that exert significant impact on the transport behavior of MNPs subjected magnetophoresis is thoroughly discussed: (i) Brownian motion and diffusion of MNPs, (ii) particles/particles interaction (cooperative effect) and (iii) MNPs/fluid interaction (hydrodynamic effect).

2.3.1 Brownian Motion and Diffusion

When MNPs are dispersed in a fluid, there is continuous collision between the particles and the surrounding fluid, which creates the random force acting on MNPs that subsequently causes the particles to experience the random change in the moving direction. Such random motion is denoted as Brownian motion, named after Robert Brown, who stated it in the literature after observing the collision between the pollen grains and the surrounding fluid molecules in the year of 1827 (Darras et al., 2017). Such a random nature of Brownian motion is thermally driven, and it presents another level of randomization in terms of affecting the dynamics (and direction of motion) of magnetophoresis process (Chong, Leong and Lim, 2021). In addition, such a random motion at particle level causes the net migration of particles from region of high particle concentration towards the region of low concentration, which induces a macroscopic process known as diffusion. In fact, the greater extent of Brownian motion will lead to the more significant diffusion process and the magnitude of the diffusive displacement for the Brownian particles in the radial

direction (in term elapsed *t*) can be related to diffusion coefficient *D* by the following equation (Kärger, 1992):

$$d^2 = 2Dt \tag{2.13}$$

For a spherical MNPs in the solution, the diffusion coefficient can be expressed as follows (Liu, Cao and Zhang, 2008):

$$D = \frac{k_B T}{3\pi\eta d_H} \tag{2.14}$$

Here, k_B is Boltzmann constant and *T* is absolute temperature of the MNP solution. According to Equation (2.14), the diffusion coefficient (and hence the intensity of Brownian motion) of the MNP increases under the higher temperature or/and the MNP of smaller size is used (Lim, Yeap and Low, 2014).

2.3.2 Cooperative and Non-Cooperative Magnetophoresis

Typically, magnetophoresis process can be classified into two regimes according to the nature of inter-MNP interaction throughout the process, namely cooperative and non-cooperative magnetophoresis. Cooperative effect of magnetophoresis is a phenomenon involves the self-aggregation and collective motion of MNPs in the solution due to the interaction between the magnetic dipole moment held by each MNP (de Las Cuevas, Faraudo and Camacho, 2008). Due to the superparamagnetic nature of MNPs, MNPs will be magnetized and gain net magnetic dipole moment upon exposure to the external magnetic field. If the particle concentration is sufficiently high (or

MNPs are sufficiently close among each other), such a magnetic interaction among MNPs can be very intense, which renders the cooperative effect to be very significant during magnetophoresis (Figure 2.4 (a)). However, cooperative effect can also be non-existence in the MNP solution with very low concentration, in which the interparticle distance is very large and this causes the dipole-dipole interaction between each MNP to be trivial. Under this scenario, MNPs will migrate individually as single particles toward the magnetic source throughout the entire magnetophoresis process (Figure 2.4 (b)) (Andreu et al., 2012a).

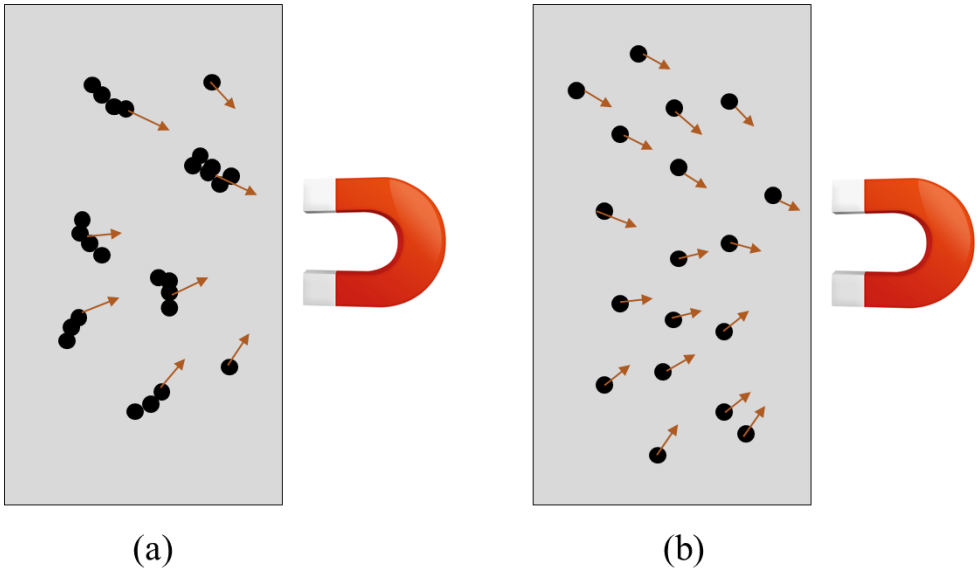

Figure 2.4: Illustration for (a) cooperative magnetophoresis and (b) non-cooperative magnetophoresis of MNPs. The red arrows indicate the motion of MNPs.

Various researchers have observed both cooperative and non-cooperative effects in their real time magnetophoresis experiment, which have been widely published in the scientific literature. For instance, non-cooperative phenomenon has been observed for the magnetophoresis of MNPs are

functionalized with polyelectrolyte stabilizers to produce sufficient electrostatic repulsion between the MNPs and MNP concentration is relatively low (Andreu et al., 2011). On the other hand, cooperative effect has been observed in the experiments reported by Andreu and coworkers, in which the separation time for the magnetophoresis process (to achieve 90% of particle removal) with cooperative effect (~300 s) is about 10 times faster than the magnetophoresis that is occurring under non-cooperative manner (~3000 s), as shown in Figure 2.5 (Andreu et al., 2011).

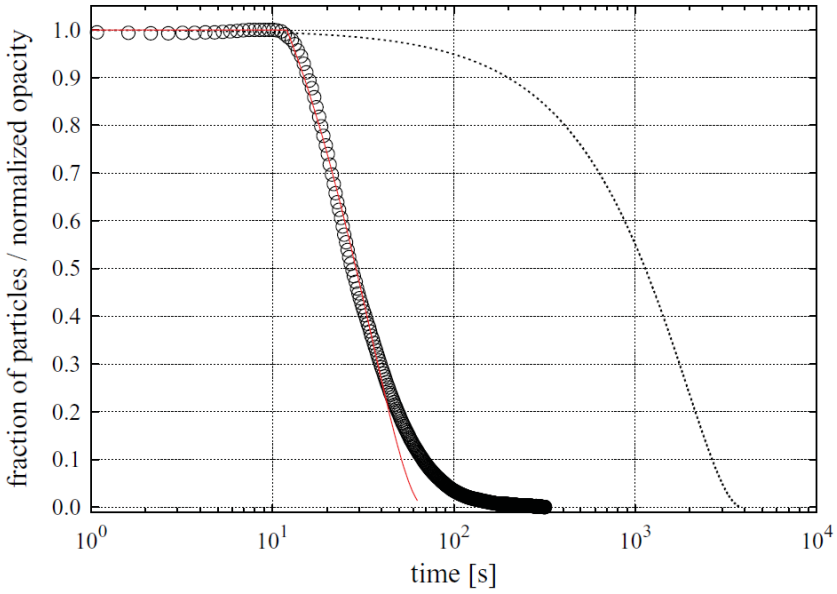

Figure 2.5: Comparison between cooperative effect (circles) and noncooperative effect (dotted line) under magnetophoresis process (Andreu et al., 2011)**.**

Obviously, the occurrence of cooperative effect has remarkably speed up the magnetic separation process. The MNPs are moving individually in the magnetophoresis that occurs non-cooperatively, which causes the MNPs to be subjected to the lower magnetophoretic force (in relative to viscous drag force). Thus, the magnetophoretic velocity acquired by MNPs is lower and this will

cause the successful separation of MNPs from the solution to be more time-consuming. Contradictory, in the cooperative magnetophoresis process, the larger size of aggregated MNPs enhances the magnetic volume which causes the MNP aggregates to experience a larger magnetophoretic force (in relative to the increment of the opposing viscous drag force) and speed up the MNP migration toward the magnetic source. Thus, the shorter separation time will be resulted for cooperative magnetophoresis, as compared to its non-cooperative counterpart (Faraudo, Andreu and Camacho, 2013).

The self-aggregation of MNPs can be rapid and instantaneous, has been observed and reported by various researchers. For instance, upon subjected to magnetic field for few seconds, the MNPs self-aggregate into elongated shape (slender aggregate), with their long axis orientated along the direction of the magnetic field lines (Figure 2.6 (a)) (Schaller et al., 2008). Other than that, Andreu and coworkers have demonstrated that MNPs formed long chain aggregates in their simulation based on an on-the-fly coarse-grain (CG) model (Figure 2.6 (b)) after 0.28 seconds (Andreu et al., 2012b). Furthermore, in Figure 2.6 (c) can be observed that the aggregation of MNPs is accomplished prior to the motion of these MNP aggregates induced by the magnetic field gradient ∇B, as indicated by white arrows (Faraudo, Andreu and Camacho, 2013). Therefore, through the examples given here, it can be revealed that the timescale for the aggregation process is shorter as compared to the magnetophoresis.

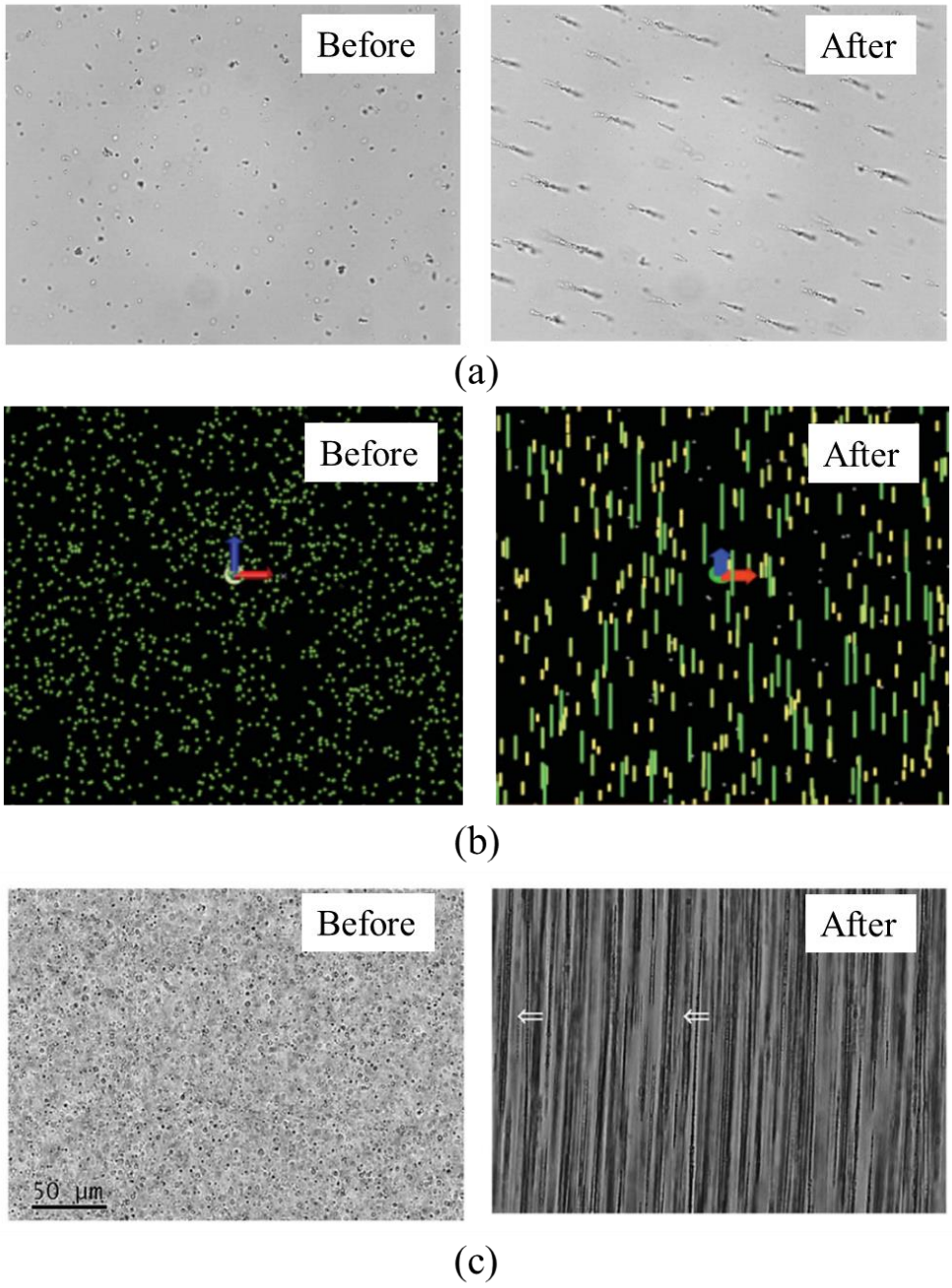

Figure 2.6: (a) Optical microscopy images of nanoparticles (with diameter of 425 nm) in deionized water before and after exposure to an external magnetic field for few seconds (Schaller et al., 2008)**, (b) Snapshots from simulations with Γ = 40 for MPs (green dots) before and after exposure to strong magnetic field for 0.28 s** (Andreu et al., 2012b)**, (c) Optical micrograph showing a MNP solution with concentration of 1 g/L with diameter of 0.41 µm before and after exposed to magnetic field for 120 s. The white arrows indicate the direction of MNP migration under magnetic field.** (Faraudo, Andreu and Camacho, 2013)**.**

In addition, the cooperative or non-cooperative nature of a magnetophoresis process can be predicted by two parameters, namely (1) ratio of magnetic Bjerrum length to particle diameter and (2) aggregation parameter (de Las Cuevas, Faraudo and Camacho, 2008; Faraudo and Camacho, 2010; Andreu et al., 2011).

Magnetic Bjerrum length, λ_B is defined as the distance between two MNPs (with the magnetic dipole moments aligned in the same direction) in which the attractive magnetic energy equals the thermal energy $k_B T$, as shown in following equation (de Las Cuevas, Faraudo and Camacho, 2008):

$$\lambda_B = \left[\frac{\pi \mu_0 M^2}{72 k_B T}\right]^{\frac{1}{3}} d_p^2 \tag{2.15}$$

The presence of self-aggregation in MNP systems can be determined by comparing the values of the magnetic Bjerrum length and the particle diameter, d_p. In fact, the formation of aggregates is conceivable, when the displacement between two MNPs is less than magnetic Bjerrum length where the energy of the magnetic dipole-dipole attraction is greater than the thermal energy. In contrast, if the displacement between two MNPs is greater than magnetic Bjerrum length, thermal energy is dominating, and the magnetic dipole-dipole attraction is not sufficient to cause the aggregation of two MNPs. Therefore, the presence of self-aggregation in MNP systems can be determined by comparing the values of the magnetic Bjerrum length and the particle diameter, d_p. For the case in which $\lambda_B < d_p$, the thermal randomization effect is still overwhelming the magnetic attraction even two particles are in close contact among each other, thus, cooperative effect is insignificant under this scenario. In contrast, the cooperative effect can be apparent for MNP system with $\lambda_B >$

d_p and the self-aggregate of MNPs can play a vital role in altering the dynamical behavior such a magnetophoresis system.

In addition, Andreu and coworkers have proposed another way to predict the occurrence of MNP self-aggregation by using thermodynamic self-assembly theory. Here, the occurrence of cooperative effect in magnetophoresis could be determined by a dimensionless quantity known as aggregate parameter N^*, which is formulated by the following equation (Andreu et al., 2011):

$$N^* = \sqrt{\emptyset_0 e^{\Gamma - 1}} \tag{2.16}$$

Here, $\emptyset_0$ is the volume fraction of MNPs in the solution and Γ is ratio between the magnetic energy associated to the dipole-dipole attraction and the thermal energy when both MNPs are in close contact, as shown in the following equation (Andreu et al., 2011):

$$\Gamma = \frac{\mu_0 \mu^2}{2\pi {d_p}^3 k_B T} \tag{2.17}$$

The aggregation of MNP is observed in a magnetophoresis system when the aggregate parameter is greater than unity ($N^* > 1$). Whereas for $N^* < 1$, there is no formation of particle aggregate, in which the individual motion of MNPs is dominating the dynamical behavior of the entire magnetophoresis process. In addition, under cooperative regime, the value of N^* also can be used to indicate the average number of individual MNPs in an aggregate when the MNP system is subjected to magnetophoresis (Faraudo, Andreu and Camacho, 2013).

2.3.3 Induced Convection under Magnetophoresis

As the magnetophoresis process involves the movement of MNPs in fluid, the interaction between the moving MNPs and the surrounding fluid is inevitable. When the MNPs migrate through a fluid medium (originally in a stagnant state), the momentum will be transmitted from the moving MNPs to the surrounding fluid by viscous effect which subsequently causes the surrounding fluid to acquire momentum. In this regard, there will be the occurrence of convection throughout the MNP solution subjected to magnetophoresis. In fact, not only the magnetically responsive MNPs are moving, but the non-magnetically responsive fluid is also moving during the magnetophoresis. Thus, under the action of the induced convection, the MNPs may be distributed and dispersed evenly in the solution. Such an occurrence of induced convection due to the particle-fluid interaction is also denoted as hydrodynamic effect of magnetophoresis.

According to the literatures available, there are some experimental and simulation evidence showing that the occurrence of induced convection flow in the MNP solution subjected to magnetophoresis. For instance, as demonstrated by Leong and coworkers in their experiments, the presence of induced convection flow was observed in the MNP solution filled in the cuvette (with characteristic length in the order of ~10^{-2} m) upon exposure to magnetic field (which is a typical batch process). In their experiment, dye was injected into the MNP solution subjected to magnetophoresis to visually trace the flow behavior of the solution, as shown in Figure 2.7 (Leong, Ahmad and Lim, 2015; Leong et al., 2017; 2020). In addition, based on the simulation results that were reported by Khashan and Furlani (Figure 2.8), the disturbance of the

streamlines of MNP solution under magnetophoresis can be observed in the CF microfluidic channel (with length scale of the order of ~10^{-4} m) (Khashan and Furlani, 2012; 2013; Mathew et al., 2015). Thus, it can be concluded that the significance of hydrodynamic effect is influenced by the geometrical configuration (ranging from microfluidic channel to macroscopic scale) as well as the operation mode (either BW or CF operation modes).

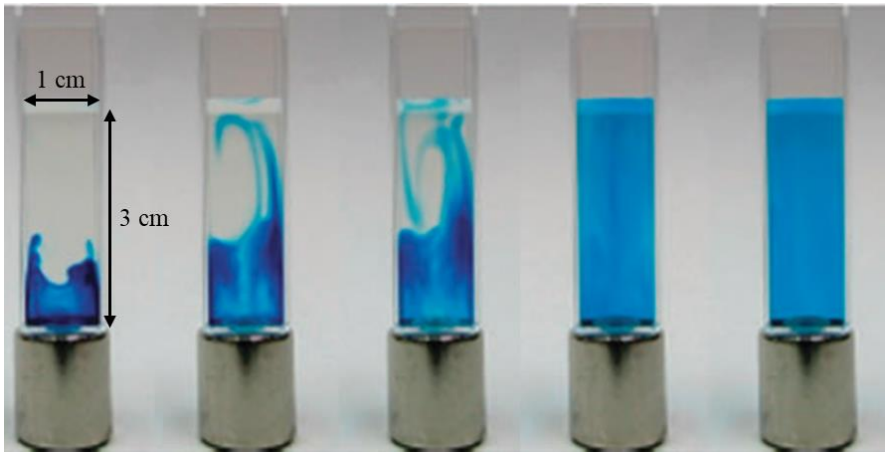

Figure 2.7: Induced convection flow in lab-scaled magnetophoresis system (Leong, Ahmad and Lim, 2015)

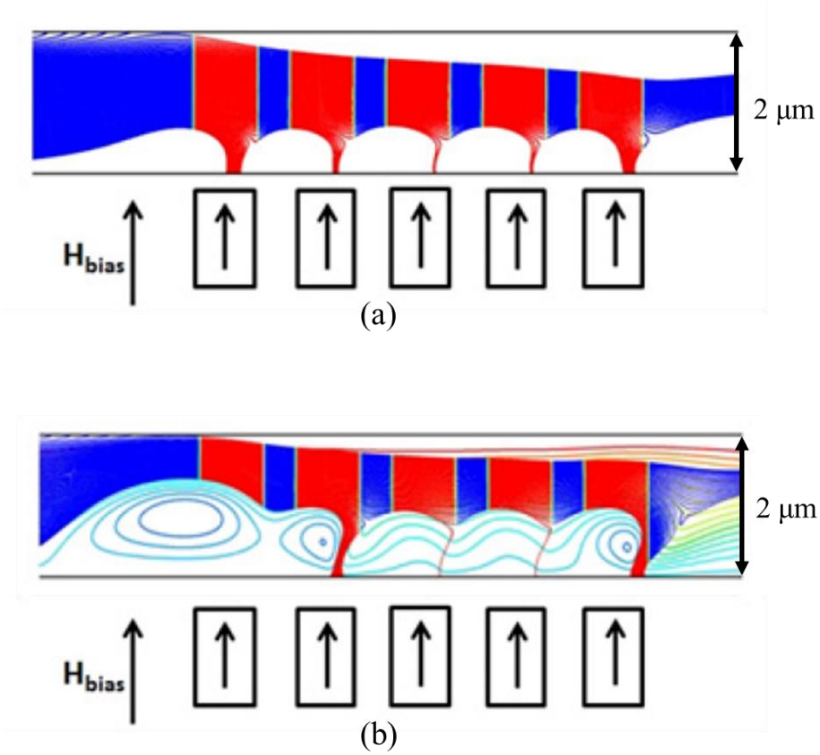

Figure 2.8: Analysis of flow perturbation (streamlines) in MNP solution through the CF microfluidic channel by (a) one-way particle fluid coupling and (b) two-way particle fluid coupling (Khashan and Furlani, 2013)

Interestingly, such an induced convection flow phenomenon has been proven to accelerate the magnetophoresis process and shorten the separation time of MNP significantly. For instance, according to the simulation results presented by Leong and coworkers (Figure 2.9), the collection rate of the MNPs is 27 times faster under the presence of induced convective flow as compared to the condition without considering the hydrodynamic effect and occurrence of induced convection (Leong, Ahmad and Lim, 2015). Moreover, the induced convective flow (typically in the order of magnitude of 10^{-5} – 10^{-4} m/s) is much faster as compared to the magnetophoretic velocity of individual MNP (is estimated to be approximately 10^{-6} m/s under magnetic field gradient of 100 T/m (Leong et al., 2017) for MNPs with size of 43 nm and

magnetization of 42.7 emu/g). In this context, the induced convection flow is eventually driving MNPs that are located at the weaker magnetic gradient region towards the region with stronger magnetic gradient region within shorter duration. When the MNPs arrive at the region with stronger magnetic field gradient, they will experience the stronger magnetophoretic force and being captured more rapidly, which in turn accelerates the magnetophoretic separation rate of the MNPs (Figure 2.7).

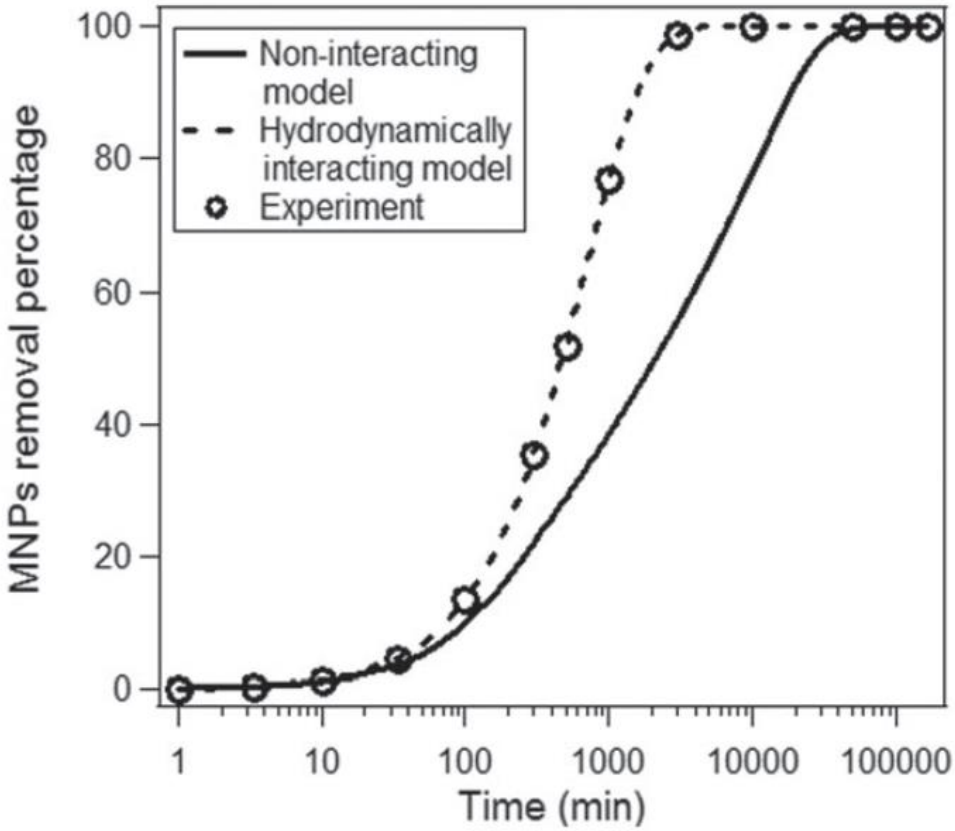

Figure 2.9: Comparison of MNP removal percentage versus time under the conditions with and without the presence of magnetophoresis induced convection (Leong, Ahmad and Lim, 2015)**.**

Apart from the macroscopic scale magnetophoresis system as reported in the previous paragraph, the hydrodynamic effect also plays an important role in enhancing the capture efficiency of MNPs that is conducted in a microfluidic

device. For instance, according to the simulation results as demonstrated by Khashan and Furlani, it has been proven that with hydrodynamic effect (if two-way particle fluid coupling is considered in the modelling), the capture efficiency of MNPs in microfluidic channel (with average inlet fluid velocity of 5 mm/s) is improved to 64% as compared to the case in which only one-way particle fluid coupling approach (~53%) is assumed in the simulation (Khashan and Furlani, 2013). For one-way particle fluid coupling approach (Figure 2.8 (a)), momentum is only allowed to be transported from the surrounding fluid to MNPs but not in the opposite way, so that the fluid flow is assumed to be unaffected by particle motion (Wu, Wu and Hu, 2011). Two-way particle fluid coupling is the approach (Figure 2.8 (b)) in which interchange of momentum between MNPs and fluid can occur in two directions which subsequently leads to the generation of induced convection in the solution (Khashan and Furlani, 2013), thus, increasing the capture efficiency of MNPs.

In addition, the intensity of induced convective flow under magnetophoresis process can be deduced theoretically in a quantitative manner, by using a dimensionless parameter denoted as magnetic Grashof number, Gr_m which is formulated as follows (Leong et al., 2020):

$$Gr_m = \frac{\nabla B \left(\frac{\partial M}{\partial c}\right)_H (c_s - c_\infty) {L_c}^3}{\rho v^2} \tag{2.18}$$

Here c is the concentration of MNPs, c_s is the concentration of MNPs on the surface that MNPs are captured, c_∞ is the concentration of MNPs in bulk solution, L_c is the characteristic length, ρ is the density of the MNP solution and v is the kinematic viscosity of MNP solution. According to Equation (2.18), it is worth emphasizing that the intensity of induced convective flow

(magnetic Grashof number) is strongly affected by the characteristic length of the system under magnetophoresis. This phenomenon is well described in the Figures 2.7 and 2.8 which show the comparison of the induced convection flow under magnetophoresis system performed in a laboratory-scale standard cuvette (dimension size of 1 × 1 × 3 cm) as well as in a microfluidic device (length scale of 200 μm × 2 mm × 10 mm). In the macroscopic system, it can be observed that the turbulence convective current is developed uniformly over the whole volume of the MNP solution (Figure 2.7). In contrast, when a much-confined space of microfluidic channel was used, only a slight interruption in the streamlines can be observed in the region near to the magnet while the laminar flow is still preserved in another region with relatively weaker magnetic field gradient (Figure 2.8).

2.4 Mechanism of Magnetic Separation

In this section, some separation principles of convectional magnetic separators are first discussed. Then, the details on the separators that using the principle of HGMS and LGMS to separate MNPs from the solution are also reviewed. Moreover, the features of the separators involving HGMS and LGMS processes are compared.

2.4.1 Conventional Magnetic Separator

In recent years, many types of magnetic separator have been used in the real time industry for mining applications, such as magnetic rotary drum separator, cross-belt magnetic separator and etc. For instance, the magnetic rotary drum separator consists of a non-magnetic rotating drum with an inner surface made of ceramic or rare-earth magnetic alloys and equipped by a small number of magnets as shown in the Figure 2.10 (Wills and Finch, 2016). Throughout the entire separation operation, the rotary drum whirs at a uniform speed and is fed with a moving stream of materials. Next, the materials (or minerals) in particles form that exhibit the ferromagnetic and paramagnetic properties will be attracted and absorbed by the rotating magnets and adhere to the outer surface of the rotating drum. This separator is able to yield a clean magnetic concentrate with high purity (99.99%) which is suitable for the recovery of valuable minerals from beach sand (Wills and Finch, 2016).

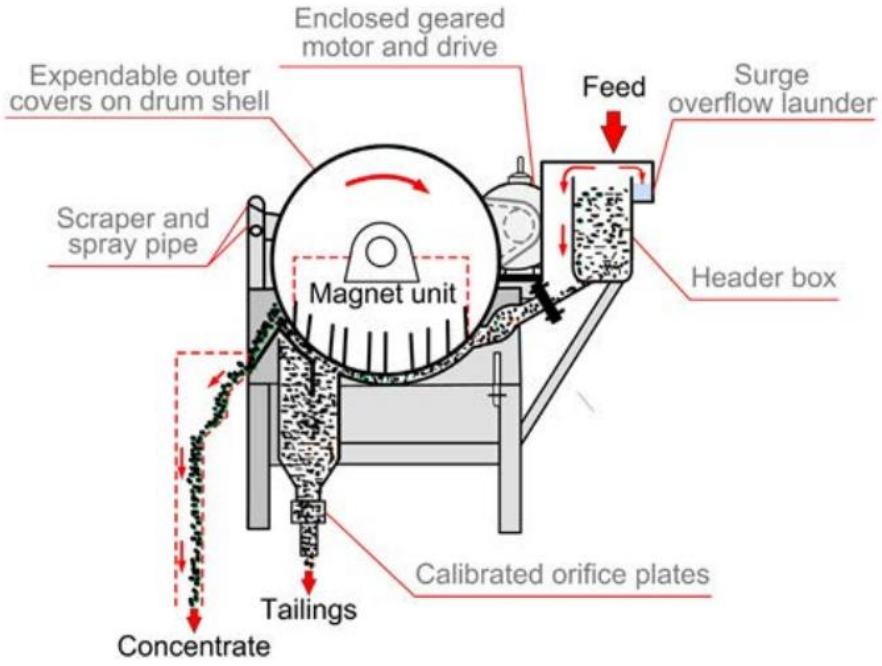

Figure 2.10: Magnetic drum separator (Wills and Finch, 2016)**.**

Furthermore, cross-belt magnetic separator is made up of two conveyor belts, one for transferring the feed materials and one consisting of permanent magnets to attract the magnetic materials as shown in Figure 2.11. During the operation, the minerals carried by the conveyor belt will pass through the conveyor belts consisting of permanent NdFeB magnet that generates a magnetic field to attract the materials with higher magnetic susceptibility and strip them off into the captured minerals or metals storage (Wills and Finch, 2016). This magnetic separation has been widely used for sorting used beverage cans which provides the most intensive and effective method of classifying aluminium and steel cans (Capuzzi and Timelli, 2018). Moreover, cross-belt magnetic separator can be effective on the separation of ilmenite and rutile in the mineral beach sand industry.

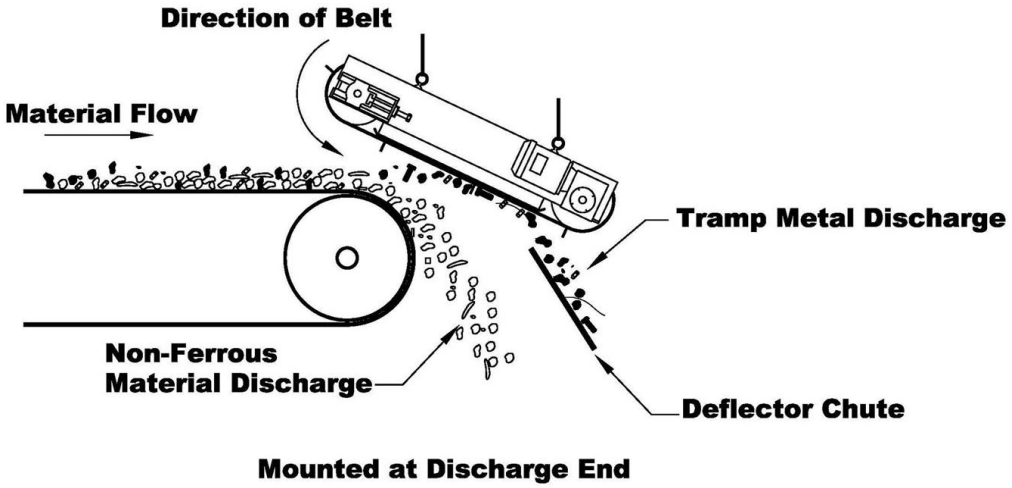

Figure 2.11: Cross-belt magnetic separator (Wills and Finch, 2016)**.**

However, these conventional magnetic separators mentioned here can only be used to separate magnetic materials/particles with relatively huge in size (6 – 8 mm). Thus, it is not applicable if MNPs are used, and more

advanced separation scheme must be developed to achieve the separation of MNPs from their suspension.

2.4.2 Separation Mechanism of HGMS

Typically, the isolation of MNPs from the surrounding medium by using magnetic field is greatly challenging due to the extremely tiny size of MNPs (can be as small as a few nanometer). At such a tiny size, MNPs experience relatively large viscous drag and Brownian forces (as compared to the driving magnetic force) that can hinder the deterministic motion manipulated by the external magnetic field (Lim et al., 2011). In order to cope with this problem, high magnetic field gradient can be applied to the MNP solution so that the magnetophoretic force imposed on the MNPs is sufficiently large to overcome the viscous resistance and random thermal motion, which enables the separation to be achieved within a reasonable time scale (Leong, Ahmad and Lim, 2015). In fact, this concept is employed in HGMS system (Oberteuffer, 1973), which is operated by a combination of magnetized matrix with a strong external magnetic field (created by electromagnet or permanent magnet) as shown in Figure 2.12 (Oberteuffer, 1974). The function of magnetized matrix in HGMS system is to create disturbance in the relatively uniform magnetic field (placed in between the magnetic poles) to generate high magnetic field gradient within the separation column to capture the targeted particles effectively (Moeser et al., 2004). Under this separator configuration, inhomogeneous magnetic fields with extremely high and localized magnetic

gradient are formed in the vicinity of magnetized matrix within the separator column (Moeser et al., 2002). During the operation, the solution containing MNPs will be flowing continuously through the column. When the MNPs are approaching the magnetized matrix with very high magnetic field gradient, they will experience very strong magnetic attraction force and rapidly captured onto the magnetized matrix (Leong, Yeap and Lim, 2016). The common materials to be used as the magnetized matrix are wire coil, steel rods, grids, screens, grooved plates, expanded metal, woven wire mesh, steel balls, and steel wool (Svoboda, 2004; Leong, Yeap and Lim, 2016; Ge et al., 2017). Depending on the material, geometry, size, shape and arrangement of the magnetized matrix, the magnitude of the magnetic field gradient can be as high as 10^3 or 10^4 T/m (Ge et al., 2017). In fact, HGMS has been employed in various real time engineering applications such as purification of liquid, kaolin clay, wastewater treatment, mining, and the chemical industry (Cieśla, 2003).

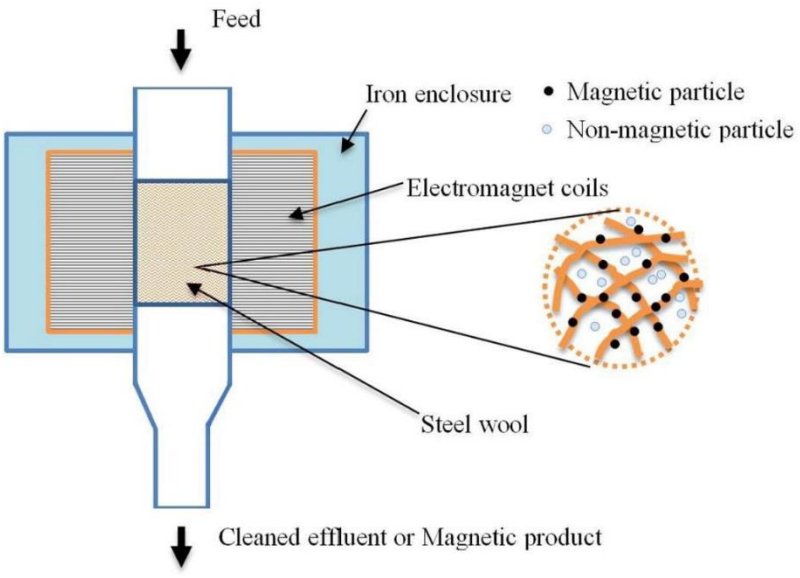

Figure 2.12: Schematic diagram of HGMS (Ge et al., 2017)**.**

Although HGMS is a well-developed and widely established process in industry and has high separation efficiency, it suffers from several drawbacks. First, the installation and operation cost for HGMS system is extremely high owing to the high-power consumption of the electromagnet and magnetic power generation (Toh et al., 2012; 2014). Moreover, the highly randomized magnetized matrix and inhomogeneous magnetic field within the column cause the prediction of the magnetic field distribution to be extremely challenging, which consequently restricts the development of analytical solution to describe and optimize the process (Moeser et al., 2004; Chong et al., 2021). In addition, after conducting one separation cycle, the MNPs attached to the magnetized matrix are difficult to be removed due to the complex structure of the matrix, which can deteriorate the separation efficiency of the subsequent operating cycle. Additionally, this feature also causes the maintenance cost of the HGMS column to be higher (Hatch and Stelter, 2001; Gómez-Pastora, Bringas and Ortiz, 2014).

2.4.3 Separation Mechanism of Batchwise (BW) LGMS

In contrast to HGMS system, LGMS process involves only the utilization of strong permanent magnet(s) located outside a container (or separation chamber) filled with MNP solution, without the involvement of magnetized matrix (Figure 2.13). Under this configuration, it allows magnetic separation to be performed in a less complex environment, however, the inhomogeneity of the magnetic field will be reduced and therefore resulting in a weak magnetic field

gradient over the separation chamber. Typically, the magnetic field gradient decays tremendously with respect to the distance from the magnet, so that the magnitude of the magnetic field gradient at most regions of the separation chamber is below 100 T/m if this separation scheme is employed (Lim, Yeap and Low, 2014). Owing to this reason, magnetophoretic force exerted on the MNPs under LGMS mode is relatively weaker, even though its configuration is much simpler than HGMS column. Nevertheless, the capital cost of LGMS is much lower as compared to HGMS system.

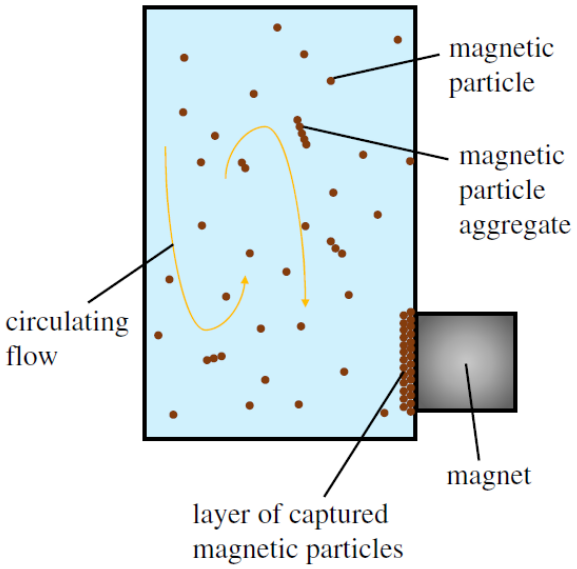

Figure 2.13: Schematic diagram of LGMS (Leong, Yeap and Lim, 2016)**.**

Despite of the low magnetic field gradient (and hence magnetic force imposed on every MNPs) exhibited by the LGMS scheme, MNPs can be collected by within a reasonable timescale according to various experimental studies reported in the existing literature. For instance, Yavuz and coworkers have developed the LGMS technique that operates in BW manner to induce the magnetic separation of iron oxide nanoparticles (IONPs) with different size

(Yavuz et al., 2006). Their results show that magnetic field strength as low as ~0.2 T is sufficient to separate ~100% of IONPs (with size of 12 nm) from their suspension within minutes. Such a rapid separation of IONPs induced by low magnetic field gradient was attributed to the cooperative effect of IONPs during magnetophoresis, whereby the aggregation of IONPs occurred and rendered the formation of IONP aggregates that gained higher magnetophoretic velocity as compared to individual particles (de Las Cuevas, Faraudo and Camacho, 2008). Furthermore, huge number of studies have proven that the rate of magnetic separation can be strongly dependent on the concentration of MNP solution. For instance, by referring to the work reported by Lim and coworkers, the collection of MNPs in nanorod and nanosphere (Figure 2.14 (a) and (b)) under low magnetic field gradient can be accelerated when the higher concentration of MNP solution was employed (Lim et al., 2014), which corresponds to the more intensive cooperative effect.

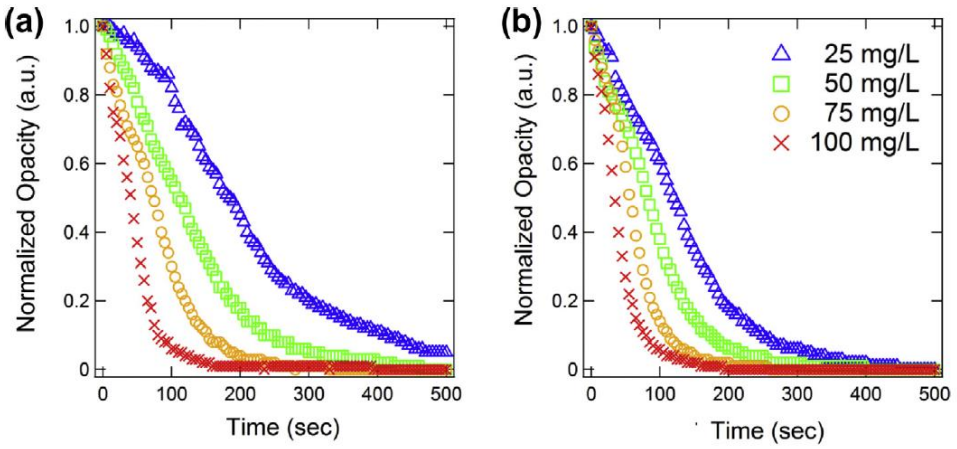

Figure 2.14: Magnetophoresis kinetic profiles of (a) poly(diallyldimethylamonium chloride) (PDDA) coated magnetic nanosphere and (b) PDDA coated magnetic nanorod under different particle concentration (Lim et al., 2014)**.**

Apart from cooperative effect, hydrodynamic effect was also revealed to play an important role in enhancing the magnetophoretic separation rate of LGMS. According to the study reported by Leong and coworkers, the magnetic separation rate for hydrodynamically dominating magnetophoresis is 27 times higher as compared to the conditions without the presence of magnetophoresis induced convection (Leong, Ahmad and Lim, 2015).

Up to the present stage, all studies on the LGMS process have been conducted in a BW manner, which involves the separation of MNPs in a lab-scaled container. However, this separation strategy encounters many drawbacks when it is to be expanded to large industrial scale. Firstly, high level of labor cost is needed as the BW operation is fully controlled by manpower which demanding intensive amount of labor power. In addition, it is also difficult to automate the process and operate remotely if BW-LGMS operation is employed. In fact, the LGMS process can be made feasible for industry applications by incorporating the CF feature towards the process, so that it can handle large volume of solution and facilitate the process automation. The automation and remote operation enable the significant reduction in labor costs, thus, addressing the drawbacks of the high labor costs exhibited BW-LGMS process (Chong et al., 2021).

2.5 Effect of Critical Design Parameters on the Separation Performance of CF-LGMS Processes

According to the existing scientific literature reported by various scientists or engineers, it can be found that the separation efficiency of magnetic separation under CF mode can be affected by several parameters such as (i) spatial distributions of magnetic field, (ii) MNP concentration, and (iii) MNP solution flowrate. Hence, the effect of these parameters on the separation efficiency of magnetic separation conducted under CF mode is briefly discussed in this section.

2.5.1 Effect of Magnet Configuration

Typically, the magnetic field distribution within the separator column (such as microfluidic devices) can be influenced by the geometrical arrangement of magnets which gives a direct impact on the transport behavior of MNPs within the column. For instance, by referring to the works reported by Zhang and coworkers, deflection of the magnetic droplet (consists of superparamagnetic iron oxide nanoparticles) in the superparamagnetic fluid within a microchannel can be affected by the position of magnet (or magnetic field distribution within the microchannel) (Zhang et al., 2009). Their theoretical and experimental results reveal that the magnetic droplet MNP can accomplish a complete deflection when there is a full coverage of intense magnetic field gradient within the microchannel (the position of magnet is on the left of bifurcation as shown in Figure 2.15 (a)). However, the reduction of region with intense magnetic field gradient in the microchannel (the position of magnet is on the

middle of bifurcation as shown in Figure 2.15 (b)) causes the magnet droplet can only accomplish half a deflection when it arrives that the channel exit.

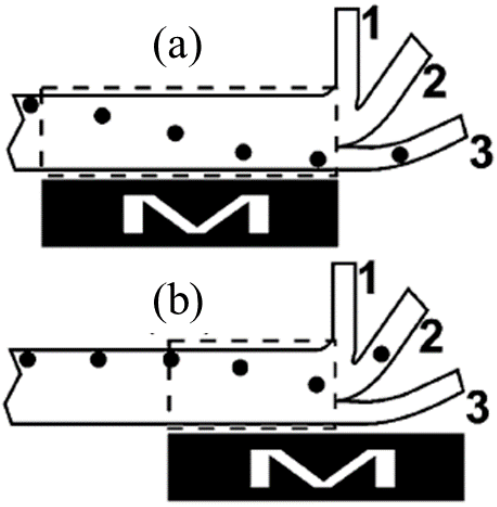

Figure 2.15: Schematic diagrams of the continuous magnetic droplet manipulation method where the magnet is arranged on the (a) left of bifurcation and (b) middle of bifurcation (Zhang et al., 2009)**.**

In addition, the mathematical simulation results reported by Khashan and coworkers also shows that the particle capture efficiency in the microchannel is affected by the magnet configuration around the microchannel (Khashan and Furlani, 2014). Based on the simulation results, it can be observed that the conventional magnet configuration (with soft-magnetic elements or magnets being implanted in the wall of a microchannel, as shown in Figure 2.16 (a)) only has a relatively low capture efficiency at ~33% because it restricts particle capture only to the walls of the channel. On the contrary, the capture efficiency under magnet configuration with flow-invasive elements (soft-magnetic elements or magnets are being arranged in a stair step configuration inside the microchannel as shown in Figure 2.16 (b)) improves remarkably to 100% (which indicates that all particles are captured by magnets) due to the higher exposure surface for the particle capture.

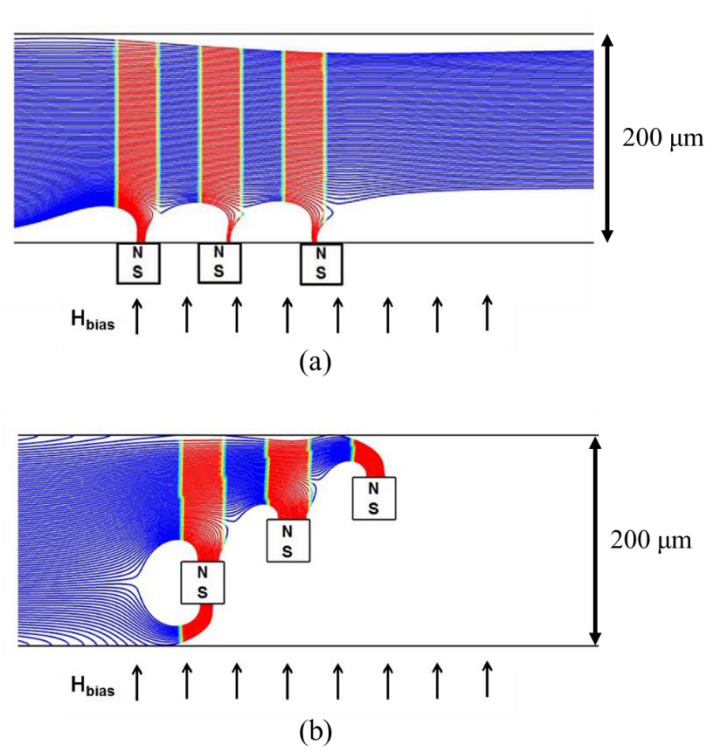

Figure 2.16: Particle trajectories for one-way particle fluid coupling in the (a) conventional magnet configuration and (b) flow-invasive elements (Khashan and Furlani, 2014)**.**

Furthermore, the number of magnets surrounding a separation chamber can alter the coverage of strong magnetic field gradient within the chamber. As the magnetophoretic force exerted on the MNPs is directly proportional the magnetic field gradient (if the particle magnetization is constant), the higher coverage of intensive magnetic field gradient within the separation chamber (which is induced by the higher number of magnets) can enhance the magnetophoretic force of the MNP in solution. Particularly, the magnetic field gradient has been revealed to be decay rapidly with respect to the distance from the magnet and some specific arrangement of magnet might greatly intensify the magnetic field gradient at a particular region. For instance, in the theoretical and experimental works reported by Gassner and coworkers, the magnetic force imposed on a MNP (with size of 300 nm) by a single magnet is

strongest adjacent to the magnetic source (with the highest magnetophoretic force of ~20 pN) in the microfluidic channel with length scale of 100 μm in high and 1 mm long (Gassner et al., 2009). However, if there are two magnets arranged in face-to-back manner, the region with more intensive magnetic field gradient can be enlarged and the highest magnetophoretic force experienced by a MNP can be significantly improved to 100 pN, which in turn accelerates the separation rate (Gassner et al., 2009). Moreover, in the simulation works reported by Chong and coworkers also have found out that increasing the number of magnets can boost the separation efficiency of CF-LGMS with the more significant deflection of MNPs towards the magnets if six magnets are used, as compared to the situation with only four magnets (Chong, Leong and Lim, 2021). Hence, based on the discussion above, the magnet configuration is one of most important parameters to be considered in the design and optimization of magnetic separation device.

2.5.2 Effect of MNP Concentration

Concentration of MNP solution has been proven as one of the important parameters in affecting the separation efficiency of magnetic separation process, either operated under BW or CF mode. In addition, it is also necessary to deal with MNP solution wide range of concentrations in the real time application of LGMS process, so it is important to study and quantitatively capture (by using a mathematical model) the effect of concentration on the separation efficiency of LGMS process. Particle concentration has significant

impact on the magnetic separation rate and magnetophoresis kinetics as the cooperative effect of magnetophoresis is a concentration dependent phenomenon. For instance, De Las Cuevas and coworkers demonstrated both experimentally that the separation time of MNPs in a BW container subjected to magnetic field generated by SEPMAG can be accelerated by the cooperative effect at higher concentration of MNP solution. Evidently, the particles can be captured by magnet in less than one minute at 10 g/L while it takes about 3 minutes to collect the particles at 0.01 g/L, as shown in Figure 2.17 (de Las Cuevas, Faraudo and Camacho, 2008). Furthermore, based on the experimental results reported by Toh and coworkers, the higher particle concentration has greatly improved the removal efficiency of MNPs (tagged microalgae cells) under low magnetic field gradient (Toh et al., 2012). The dynamical behavior of the cooperative magnetophoresis is strongly concentration dependent due to the formation of larger MNP aggregate in the MNP solution with higher concentration and the inter-particle interaction is more intense (Lim et al., 2014). Moreover, in the simulation work to calculate the separation efficiency of MNPs under CF-LGMS process, Chong and coworkers also have found out that the separation efficiency is enhanced when concentration of MNP solution as high as 1000 mg/L (almost 100%) is used, as compared to the scenario with lower particle concentration (78.43% under 10 mg/L) (Chong et al., 2021).

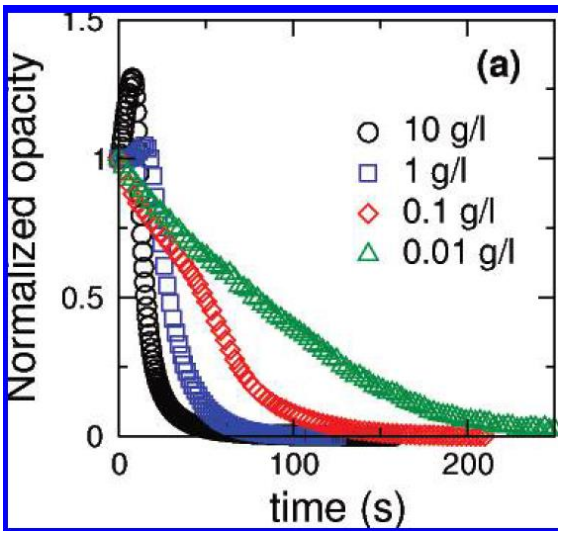

Figure 2.17: The magnetic separation profile of magnetic particles solution at different concentrations subjected to magnetophoresis experiments (de Las Cuevas, Faraudo and Camacho, 2008)**.**

Apart from the cooperative effect, the hydrodynamic effect of magnetophoresis process is also a MNP concentration dependent phenomenon, which can subsequently alter the transport behavior and separation kinetics of LGMS process. For instance, according to the experimental results presented by Leong and coworkers on the LGMS of MNPs (with non-cooperative feature) operated under BW mode, it can be observed that the intensity of induced convection is accelerated as the higher concentration of MNP solution is used (Figure 2.18) (Leong, Ahmad and Lim, 2015). In fact, the induced convection in the solution is too overwhelming and dictating the entire transport behavior of MNP solution for the concentration range employed in this study, thus, the concentration imposes no effect on the separation efficiency for this case. However, there is no experimental evidence that examining the significance of induced convection in CF-LGMS process, in which there is the presence of forced convection within the MNP solution.

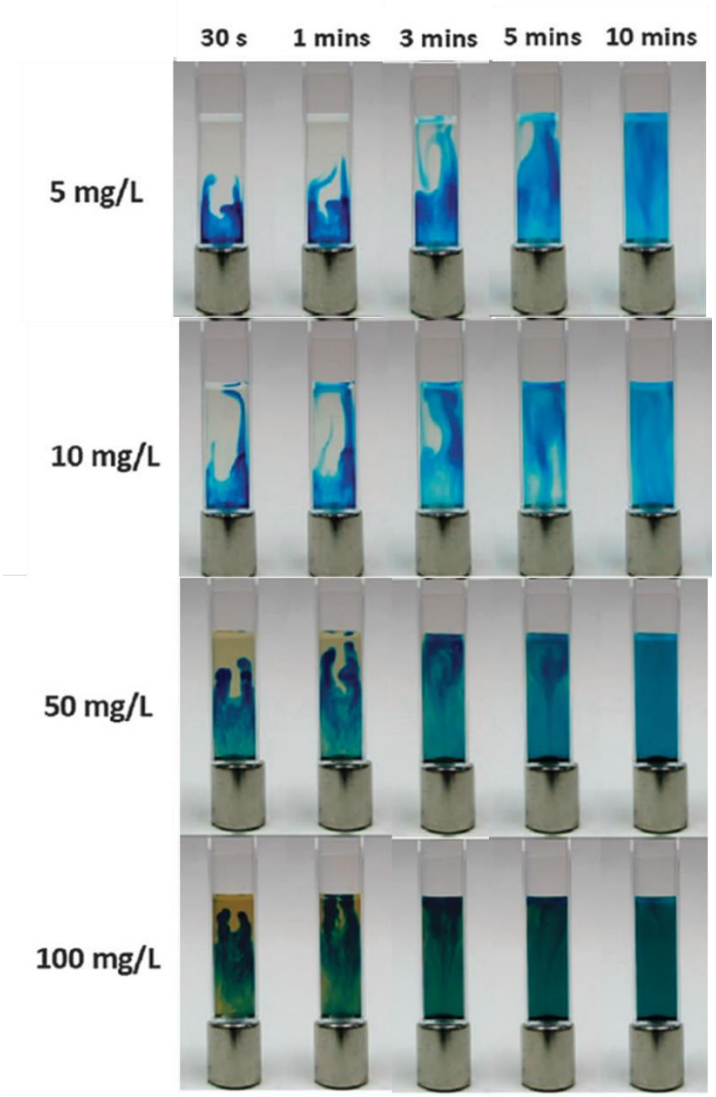

Figure 2.18: Induced convection flow in lab-scaled magnetophoresis system with different concentrations (Leong, Ahmad and Lim, 2015)**.**

2.5.3 Effect of MNP Flowrate

In the magnetic separation performed in a CF manner, the flowrate of MNP solution is revealed to be one of the principal aspects that affects the kinetics of magnetophoresis process. Various LGMS applications conducted under CF manner indicate that the flowrate is one of the essential parameters that governs the transport behavior of MNP within the separation column. For instance,

according to the experimental results presented by Pamme and Wilhelm, the degree of deflection of the superparamagnetic particles (tagged with Mouse macrophage and HeLa cells) by the magnetic field in a CF magnetic separation column is strongly dependent on the flowrate of MNP solution (Pamme and Wilhelm, 2006). For instance, the superparamagnetic particle-tagged cells are deflected by the magnetic field at a greater extent if slower flowrate is adopted (0.4 mm/s), as compared to the situation with the higher flowrate (2 mm/s). Under the lower flowrate, MNPs will have longer residence time in the separation column to migrate towards the magnetic source, being captured and isolated from the solution (Pamme and Wilhelm, 2006). Therefore, the separation efficiency is usually higher if the CF-LGMS process is operated under the lower flowrate.

Furthermore, Gourikutty and coworkers studied the effect of fluid flowrate on the capture efficiency of white blood cells from the whole blood sample by using immune tagging and magnetophoretic separation in a two-stage microchip (Gourikutty, Chang and Puiu, 2016). The experimental observation revealed that the capture efficiency of white blood cells decreases with the increasing in the flowrate, due to the stronger hydrodynamic force (in relative to the magnetic force) under high flow velocities. However, at the lowest flowrate employed in the given study (below 500 μL/min), there is no significant improvement in the capture efficiency because the separation efficiency above 99.9% can be achieved at the flowrate of 500 μL/min.

CHAPTER THREE

MATERIALS AND METHODOLOGY

In this chapter, all experimental work, and detailed methods of computational simulations for this study are outlined. Firstly, the overall research flowchart of this study is demonstrated in Section 3.1. Next, Section 3.2 shows the detailed information of material and equipment used to this research work. Next, the preparation method and characterization of the polyelectrolyte functionalized MNPs are elaborated in the Sections 3.3 and 3.4, respectively. Moreover, detailed procedure for BW-LGMS and CF-LGMS experiments is elucidated in Sections 3.5 and 3.6, respectively. Lastly, Section 3.7 demonstrates the full procedure to perform the numerical simulation of BW-LGMS and CF-LGMS process.

3.1 Research Flow Chart

The overall research stages in this study were demonstrated on below Figure 3.1

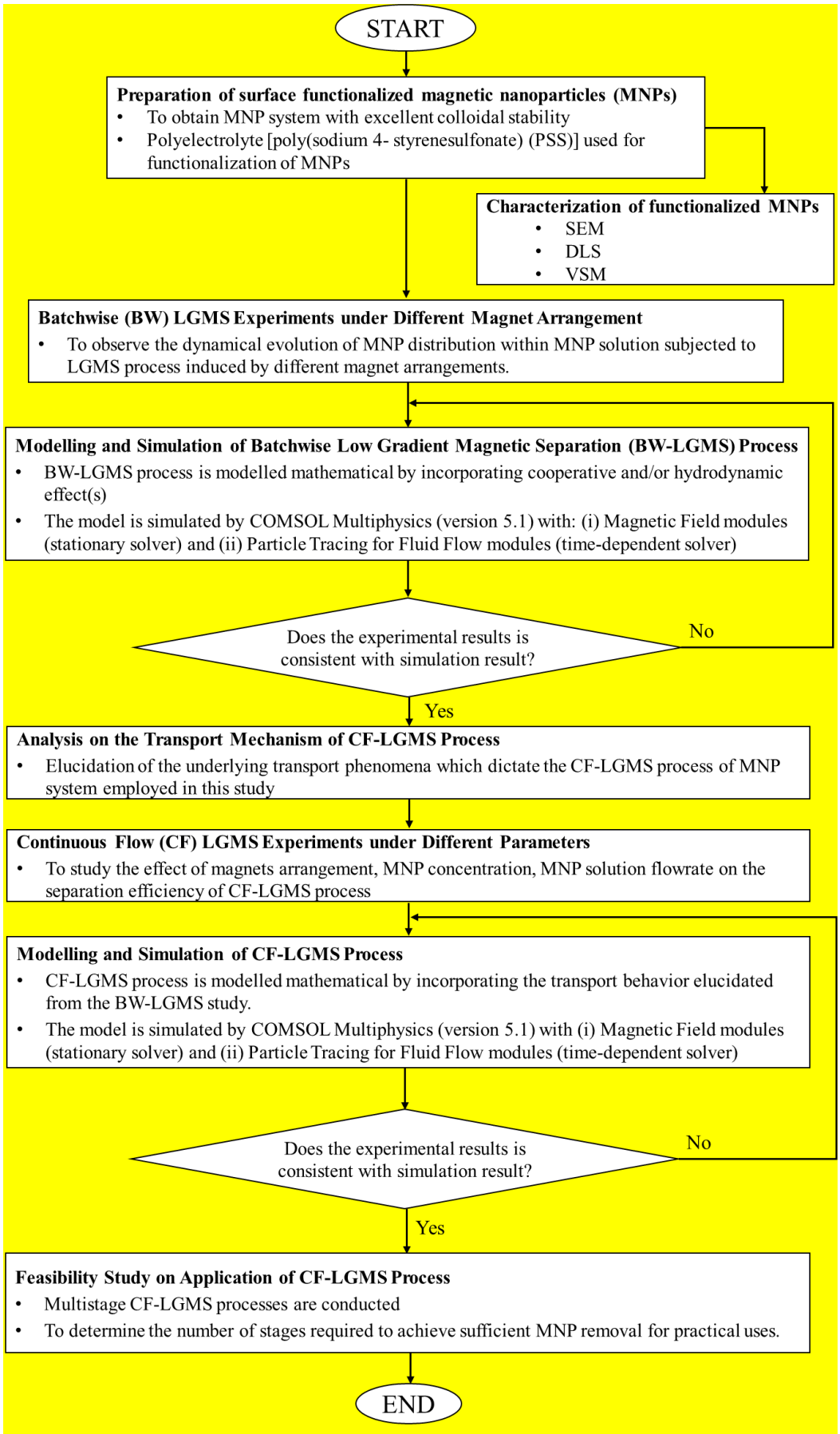

Figure 3.1: Overall research flow chart.

3.2 Raw Material and Equipment

The chemicals and materials used in this study is tabulated in Table 3.1. Iron (II, III) oxide nano powders, Fe_3O_4 (APS, 98+% purity; density: 4.8−5.1 g/cm^3) used in this experiment have the average particle size at 44.1 ± 5.3 nm. The polyelectrolyte [namely poly(sodium 4- styrenesulfonate) (PSS)] used for surface functionalization of MNPs is a yellowish powder with chemical formula of $(C_8H_7NaO_3S)_n$ and average molecular weight of ~70,000 Da.

Table 3.1: Materials used in the experiment.

Material/ Chemical	Purity	Supplier
Iron (II, III) oxide nano powders, Fe_3O_4	98%	Nanostructured & Amorphous Materials, Inc
Poly(sodium 4-styrenesulfonate) (PSS)	~70,000 Da	Sigma-Aldrich
Hydrochloric acid (HCl)	37%	Fisher Scientific

The equipment used in this study are tabulated in Table 3.2. The N52-graded Neodymium Ferrite Boron (NdFeB) cylindrical permanent magnets (1.5 cm in diameter and 2 cm in length with the remanent magnetization of 1.45 T) employed in this study. Moreover, deionized (DI) water used to dilute and disperse the samples was produced by New Human UP 900 Water Purification System with resistivity of 18.2 MΩ. Furthermore, a peristaltic pump (Masterflex L/S 77200-60 model) was used to pump the MNP solution into the separator column through a silicone tube (with inner diameter of 4 mm and outer diameter of 6 mm).

Table 3.2: Equipment used in the experiment.

Equipment name	Brand	Model number
Permanent magnets	-	N52-graded Neodymium Ferrite Boron (NdFeB)
Deionized (DI) water	Human Corporation	New Human UP 900 Water Purification System
Peristaltic pump	Masterflex	L/S 77200-60
Centrifuge machine	Eppendorf	Centrifuge 5430
Scanning electron microscope (SEM)	Joel microscope	JSM 6701F
Dynamic light scattering machine (DLS)	Malvern Instruments	Zetasizer ZS
Vibrating Sample Magnetometer (VSM)	VSM - Lake Shore	7400 Series VSM system

3.3 Preparation of Surface Functionalized Magnetic Nanoparticles (MNPs)

Prior to the magnetic separation experiments, a MNP system with sufficiently good colloidal stability was prepared by functionalizing MNPs with PSS (Yeap et al., 2018). Firstly, PSS powders were dissolved in DI water and stirred at constant speed (700 rpm) for 60 minutes to obtain PSS solution with concentration of 1.25 g/L. Next, the MNP powders were dissolved in DI water and subjected to ultrasonication for 60 minutes to prepare uniformly dispersed MNP solution at concentration of 2.5 g/L. After that, the pH value of both PSS and MNP solutions was adjusted to 3.5 ± 0.4 by using 1.0 M hydrochloric acid. The pH adjustment is to facilitate the physisorption of PSS onto the surface of

MNPs through electrostatic attraction during the functionalization process (Yeap et al., 2018).

After the pH adjustment, both solutions were mixed in a 50 mL centrifuge tube, and the mixture was placed in the ultrasonic water bath for 20 minutes to disperse PSS and MNPs so that the attachment of PSS on MNP surface can be further promoted. After the ultrasonication, the mixture was left on an end-to-end rotator operated at a rotational speed of 50 rpm for 24 hours to promote MNP/PSS adsorption equilibrium (Yeap et al., 2014). After 24 hours, the resulted PSS-functionalized-MNP solution were centrifuged at 7000 rpm to remove the excess PSS in the supernatant. Next, the collected PSS-functionalized-MNP precipitate was subjected to two washing cycles to remove the excess PSS. The washing procedures were conducted as follows: (i) PSS-functionalized-MNP precipitate was resuspended in DI water, (ii) the suspension was subjected to ultrasonication for 20 minutes, (iii) the suspension was centrifuged at 7000 rpm for 20 minutes to separate the supernatant (with excess PSS) from the washed PSS-functionalized-MNP precipitate.

3.4 Characterization of Unmodified and Functionalized MNPs

This section describes the procedure for the characterization of as-received bare MNPs as well as PSS-functionalized-MNPs used in this study: (i) scanning electron microscopy (SEM), (ii) dynamic light scattering (DLS) and (iii) vibrating sample magnetometer (VSM).

3.4.1 Scanning Electron Microscopy (SEM)

The information related to the actual size and geometrical shape of the MNPs used in this study was obtained through Scanning Electron Microscopy (SEM). Before the SEM viewing, 0.1 g of MNPs powder was coated on the specimen to countenance the scanning to transfer the image of particles. After that, the coated samples were placed on the holder and put into the SEM equipment (JOEL JSM 6701F model). The electron beam was allowed to pass through the samples and providing structural information. The magnification (×10k - ×50k) was adjusted to obtain the clear image of MNPs with high resolution (Lone, Ahmed and Ahmad, 2018).

3.4.2 Dynamic Light Scattering (DLS)

Dynamic light scattering (DLS) (Malvern Instruments Zetasizer ZS) was used to acquire the hydrodynamic diameter of PSS-functionalized-MNPs (Ramos, 2017). This characterization is necessary to confirm the successful functionalization of MNPs with PSS and particle suspension formed is within good colloidal stability before the magnetic separation experiments. In order to reduce particle-particle interaction (which will affect the accuracy of the measurement result), the MNP solution was diluted to concentration of 5−10 mg/L prior to the measurement process. Malvern Instruments Zetasizer ZS was used to record the intensity profile of the scattered light measured at an angle of 173º to the incident light, which was subsequently auto-fitted into a correlation function. This auto-fitted correlation function was used to calculate

the translational diffusivity of MNPs, which was needed to determine the hydrodynamic size of the MNPs in the solution by applying Stokes-Einstein equation (Ramos, 2017).

3.4.3 Vibrating Sample Magnetometer (VSM)

The magnetization curves of both bare MNPs and PSS-functionalized-MNPs (Yeap et al., 2014) was determined by using vibrating sample magnetometer (VSM - Lake Shore 7400 Series VSM system with Lake Shore VSM version 4.6.0) with applied field in the range of 0 to 8 kOe under room temperature. The as-received bare MNP powder was used for VSM measurement without further treatment. For the case of PSS-functionalized-MNP, it is necessary to separate these particles from its aqueous suspension and subject the particle precipitate to freeze-drying for complete water removal prior to the VSM measurement. The first step of the measurement involves the distribution of 0.0006 g of the MNP samples (in dry powder form) in epoxy to produce a cast epoxy sample, which was then connected to a vibrating glass rod at the centre of an electromagnet. The linear step (driven at each field) of 200 Oe field increment was applied with the continuous ramp at a ramp rate of 20 Oe/s. With digitally controlled field stepping and data averaging, the response of MNPs to the magnetic field was acquired for both positive and negative field components.

3.5 LGMS Experiments under Batchwise (BW) Mode

Before conducting the LGMS experiments under continuous flow (CF) mode, magnetophoresis of the PSS-functionalized-MNPs was performed under batchwise (BW) mode to observe the distribution of MNP within the magnetic field generated by different magnet arrangements (abbreviated as BW-LGMS process in this study). The purpose to conduct the study of LGMS experiments under BW mode is to scrutinize the transport mechanism of MNPs under the similar magnetic environment of CF-LGMS experiments to be conducted in the subsequent parts of this study. This is because the distribution of MNP under BW mode is easier to be visualized and compared with the simulation results due to the quiescent condition of the fluid. Then, with the transport mechanism concluded from the BW-LGMS experiment, the MNP transport mechanism in CF-LGMS of the same MNP system was deduced and being used to develop the mathematical model to predict the separation efficiency of the CF-LGMS process. In this regard, 10 mL of 80 mg/L functionalized-MNP solution was first filled into a polystyrene container with dimension of 1 cm × 1 cm × 10 cm, which was then being positioned in horizontal arrangement in this experiment. Next, the MNP solution filled in the container was subjected to magnetic field produced by different magnet arrangements (with different magnet orientation and number of magnets), as shown in Figure 3.2. The concentration profile of the MNP solution in the container was traced visually and recorded by using a camera (Canon IXUS 185 Digital Camera) for 20 minutes.

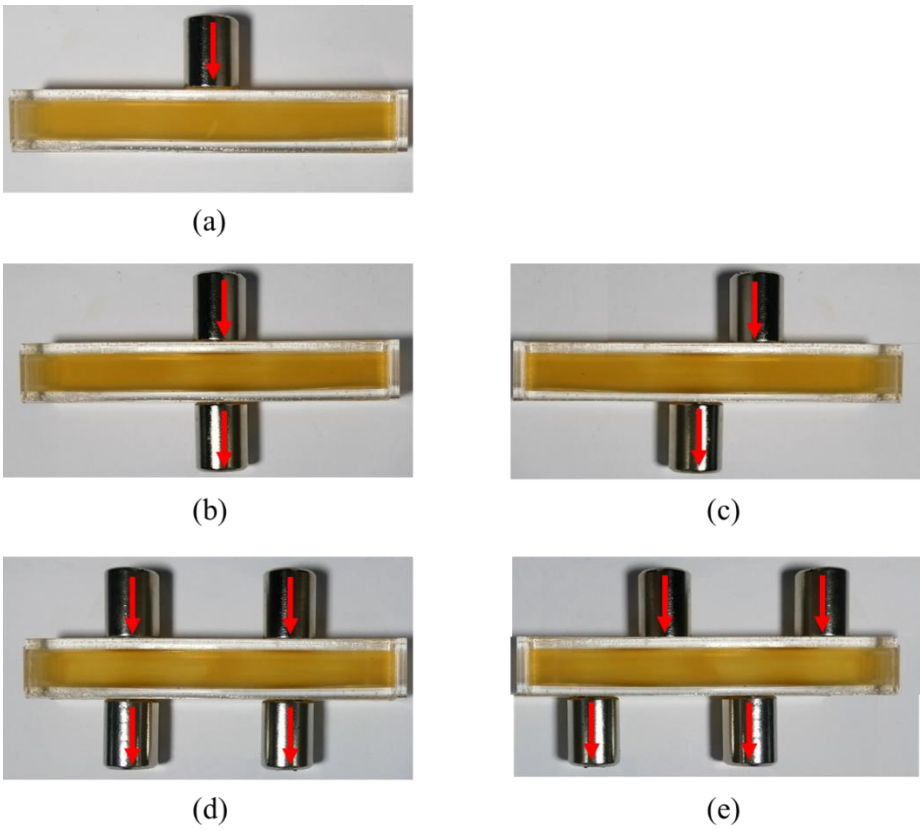

Figure 3.2: Top view of MNP solution subjected to BW-LGMS induced by different magnet arrangements (a) A1 (b) A2, (c) B2, (d) A4 and (e) B4. The red arrows are pointing towards the direction of magnetization of the magnets (pointing from south pole to north pole).

Figure 3.2 shows all magnet arrangements employed in the BW-LGMS experiments. Firstly, only one magnet was used to induce the magnetophoresis of MNPs in the BW container (Figure 3.2 (a)). Then, the number of magnets employed was increased to 2 and 4 with two different types of magnet orientation: (i) the magnets along the two sides of the container were arranged in face-to-back manner (which is denoted as aligned orientation, see Figures 3.2 (b) and (d)); and (ii) the magnets along the two sides of the container were not properly aligned (which is denoted as misaligned orientation, see Figures 3.2 (c) and (e)). In this study, the first type of magnet orientation (aligned orientation) was referred as 'A' arrangement, which involves magnets that

were arranged symmetrically (along the horizontal axis of MNP solution) at the bottom and top of the container, as shown in Figures 3.2 (b) and (d). In other words, this kind of magnet orientation exhibits horizontal symmetry around the MNP solution filled in the container. On the other hand, the second type of magnet orientation (misaligned orientation) was referred as 'B' arrangement, which involves the magnets that were evenly positioned along the bottom and top sides of the MNP solution, however, the magnet arrangement does not exhibit horizontal symmetry around the MNP solution (Figure 3.2 (c) and (e)). The numbering in the notation of the magnet arrangement indicates the total number of magnets involved, for instance, the magnet arrangement of 'A4' involves 4 magnets that were arranged in aligned orientation ('A' arrangement). In addition, it should be noted that the polarity of all magnets was pointing to the same direction in all magnet arrangements adopted in this study. Under such configuration, the magnetic field produced by the magnets from both sides of the separator column was pointing to the same direction, thus, the magnetic field strength within the separator column was undergoing constructive interference and can be maximized (Agiotis et al., 2016).

3.6 LGMS Experiments under Continuous Flow (CF) Mode

Since the main objective of this project is to understand the underlying behavior of MNPs subjected to CF-LGMS, hence, it was important to experimentally study the effect of several design parameters of the CF-LGMS system on its separation efficiency. In this section, the detailed procedures in

conducting these experiments are elaborated, in which the design parameters to be investigated are (i) spatial distributions of magnetic field, (ii) MNP concentration, and (iii) MNP solution flowrate.

3.6.1 Concentration Calibration by UV-vis Spectrophotometry

Prior to the CF-LGMS experiment, the accuracy of Beer-Lambert's Law in predicting the magnetic nanoparticle (MNP) concentrations for all experiments in the current investigation must be verified. As indicated by Beer- Lambert law, the absorbance of a light beam travelling through a MNP solution, A is directly proportional to the MNP concentration, c in the solution and the optical path length, l:

$$A = \varepsilon l c \tag{3.1}$$

where the ε is the light absorptivity of MNPs. A simple experiment was carried out to evaluate the accuracy of Beer-Lambert's Law. In this experiment, MNP solutions with different MNP concentration were prepared: 0 mg/L (Pure water), 5 mg/L, 20 mg/L, 50 mg/L, 75 mg/L, 100 mg/L, 200 mg/L and 500 mg/L. A UV-vis spectrophotometer (Jasco V-730 Spectrophotometer) was used to analyze the light absorbance of all the aforementioned diluted MNP solutions (which were filled in the cuvettes of the same dimension with the same optical path length). The intensity of the outgoing light was calculated and recorded during the measurement of light absorption by using a monochromatic light beam with a wavelength of 532 nm passing through the MNP solution. Figure 3.3 presents the relationship between light absorbance and concentration of MNP solution employed in this study, as resulted from

this experiment. As shown in this figure, light absorbance increases approximately linear with MNP concentration within the concentration range of 0 to 500 mg/L, and the coefficient of determination R^2 is 0.9996. As a result, Beer-Lambert's Law (Equation (3.1)) is valid for MNP system, which can be used to infer the concentration of MNP solution in all experiments conducted in this study.

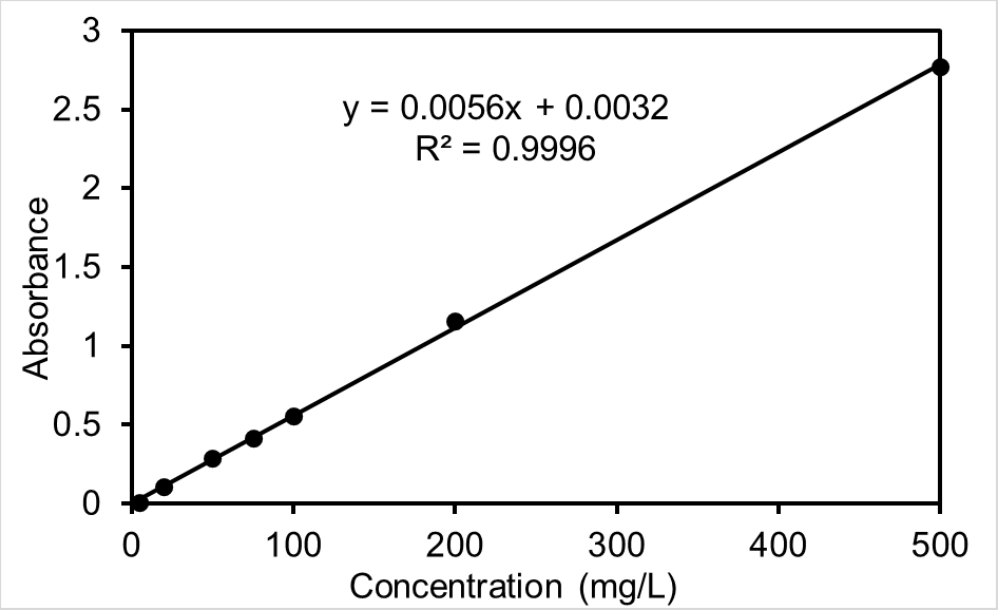

Figure 3.3: The plot of light absorbance versus MNP concentration for MNP solution employed in this study.

3.6.2 Flowrate Calibration of the Peristaltic Pump

In order to manipulate the flowrate of MNP solution (into the CF-LGMS column) by using peristaltic pump (Masterflex L/S 77200-60 model) during the CF-LGMS experiments, it is also necessary to conduct a simple calibration to relate the flow rate to the rotor speed of the peristaltic pump. Such a calibration was conducted under the same condition as the CF-LGMS experiments to be

performed in the later part of this study, i.e., the tubing with the same dimension (wall thickness, inner diameter, and length) and same type of fluid (MNP solution with the same viscosity and density) were used. This is because the tubing dimension and fluid property can affect the relationship between the flow rate and rotor speed of an operating peristaltic pump. In this calibration, the total volume of solution being conveyed by the peristaltic pump over one minute at a certain rotor speed was recorded, in which the flow rate can be calculated by using the following equation:

$$Volume\ Flowrate = \frac{V}{t} \tag{3.2}$$

where the V (mL) is the total volume of solution conveyed and t (min) is the pumping duration. The experiment was repeated three rounds for each rotor speed and relationship between the flowrate and rotor speed is tabulated in the Figure 3.4.

According to Figure 3.4, it can be observed that the flowrate of the solution increases linearly with rotor speed within the speed range of 6 to 250 rpm (which corresponds to the flowrate of 5 to 228 mL/min), with the coefficient of determination R^2 given by 0.9999. With the calibration graph shown in Figure 3.4, the flowrate of MNP solution conveyed by the peristaltic pump can be controlled by manipulating the rotor speed of the pump.

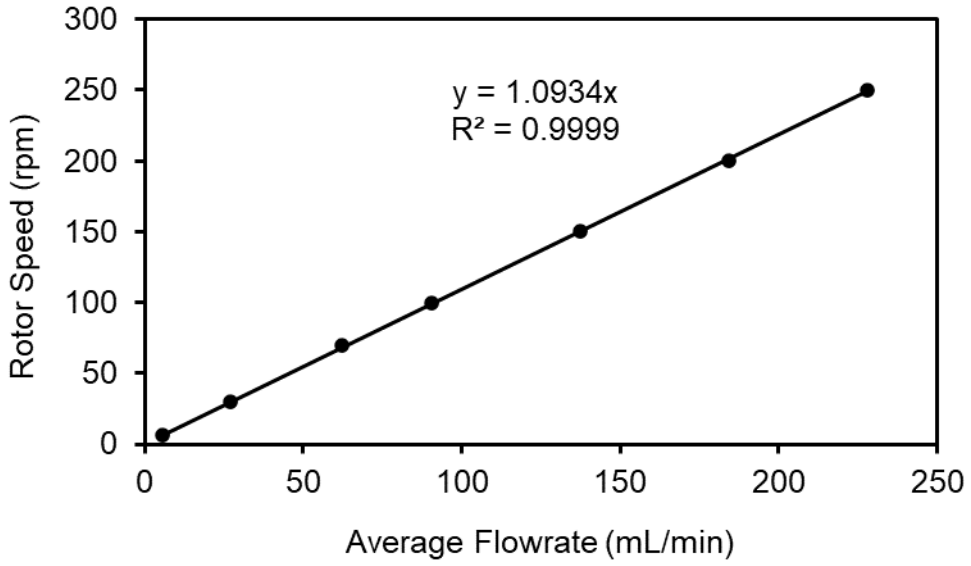

Figure 3.4: The plot of rotor speed versus flowrate for peristaltic pumps.

3.6.3 Performance Study of CF-LGMS

The schematic diagram for experimental setup of CF-LGMS is shown in Figure 3.5. First, the functionalized MNP solution was diluted to the desired concentration. Then, the diluted MNP solution (with concentration range of 20 – 100 mg/L) was pumped into a separator column surrounded by N52-graded NdFeB magnets by using a peristaltic pump with flowrate ranging from 5 mL/min to 20 mL/min (with rotor speed ranging from 6 to 22 rpm), which corresponds to the residence time of ~4 minutes to 1 minutes, respectively. The magnetic field was generated by the magnets located outside of the column such that flowing MNP solution experienced magnetic attraction force and being captured on the inner wall of the column.

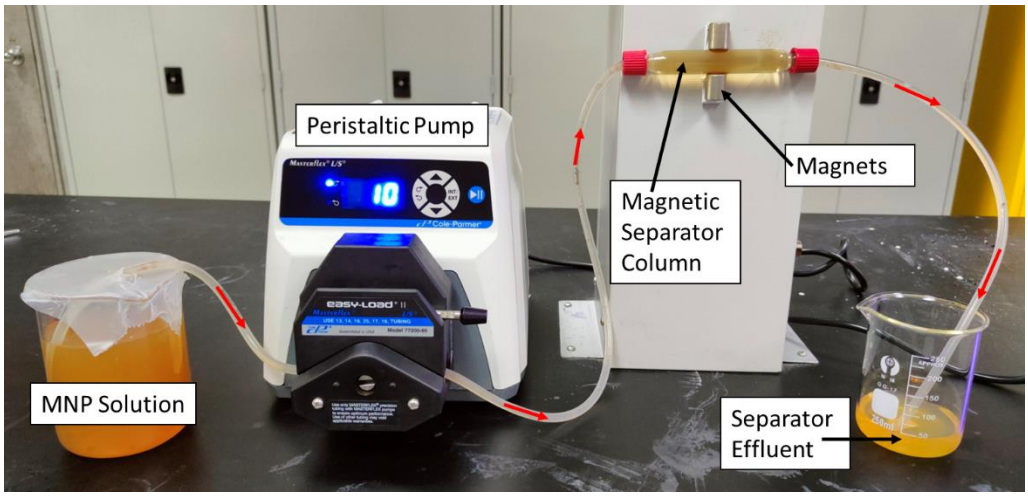

Figure 3.5: The experimental setup of CF-LGMS separator.

After that, the effluent from the separator column was collected and the concentration of the remained MNPs within the effluent was measured by using UV-vis spectrophotometer (Jasco V-730 Spectrophotometer) at the wavelength of 532 nm (Yeap et al., 2012). The correlation between concentration and light absorbance of MNP solution has been proven to obey Beer-Lambert's law (Leong et al., 2017) (see Section 3.6.1 for more details) so that the MNP concentration in the separator effluent can be calculated as follows:

$$Concentration, C = \frac{A_o - A}{A_o - A_{blank}} \times C_o \qquad (3.3)$$

where, A_0 is the initial absorbance of MNP solution fed into the separator, A is the absorbance of separator effluent, A_{blank} is the absorbance of blank solution without MNPs while C_0 is the initial concentration of the MNP solution feed. After that, the separation efficiency of CF-LGMS (percentage of MNPs that are successfully separated from the solution) can be calculated by the following equation:

$$Separation\ efficiency = \frac{C_o - C}{C_o} \times 100\% \quad (3.4)$$

The CF-LGMS experiments were conducted under different operating conditions as shown in Table 3.3. The details of all parameter studies are described in the following paragraphs. The magnet arrangements used in this study are illustrated in Figure 3.6.

Table 3.3: Details of separation experiments performed in current study.

Experimental Set	Flowrate of MNP Solution (mL/min)	Arrangement of Magnets	Number of Magnet	Particle concentration (mg/L)	Investigated Parameters:		
					Concentration	Flowrate	Arrangement of Magnets
1	10	A2	2	80			
2	10	B2	2	80			
3	10	A4	4	80			
4	10	B4	4	80			
5	10	A6	6	80			
6	10	B6	6	80			
7	10	B6	6	20			
8	10	B6	6	40			
9	10	B6	6	60			
10	10	B6	6	100			
11	5	B6	6	80			
12	15	B6	6	80			
13	20	B6	6	80			

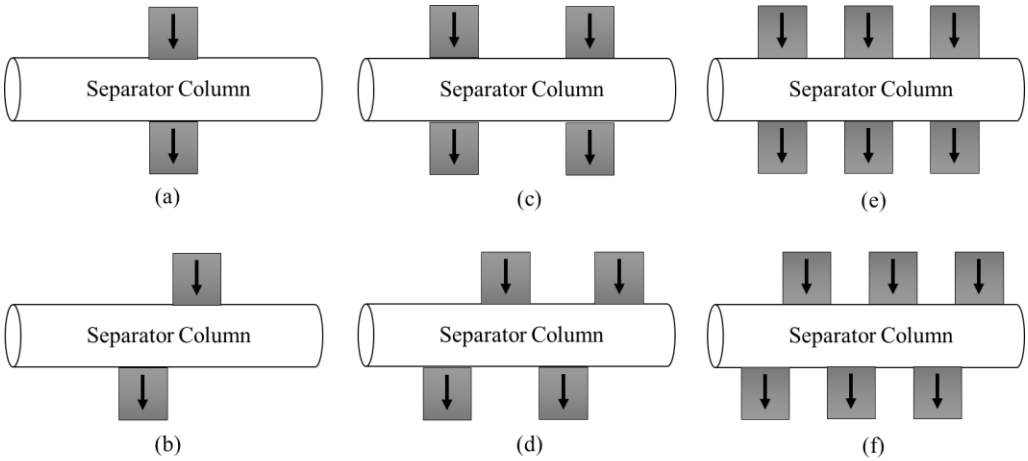

Figure 3.6: The magnetic field distributions for different magnet arrangements (a) A2 (b) B2, (c) A4, (d) B4, (e) A6 and (f) B6 under CF-LGMS.

Initially, the effect of magnetic field distribution (manipulated by the magnet arrangement surrounding the separator column) on the separation efficiency of CF-LGMS was studied. Here, the number and position of magnets surrounding the separator column were varied, as shown in Figure 3.6 (Experiment Sets 1 – 6, as indicated in Table 3.3). In these experiments, the flow rate of MNP solution was fixed at 10 mL/min and the concentration of MNP solution fed into the separator was 80 mg/L. The purpose of this study is to determine the most favorable magnet arrangement leading to the highest separation efficiency. Next, the similar experiment was conducted by using MNP solution with different initial concentration (Experiment Sets 6 - 10 of Table 3.3). The flowrate of the MNP solution was fixed at 10 mL/min and magnet arrangement shown in Figure 3.6 (f) was used (this magnet arrangement causes the highest separation efficiency according to the experimental results, which will be presented in Chapter Four). Finally, the effect of flowrate on separation efficiency of CF-LGMS was studied by varying the flowrate of the MNP solution fed into the separator column

(Experiment Sets 6, 11, 12, and 13 in Table 3.3). The initial concentration of MNP solution was fixed at 80 mg/L and the magnet arrangement shown in Figure 3.6 (f) was adopted.

Apart from the single-stage CF-LGMS experiments as described above, the CF-LGMS process was also performed in multi-stages manner. The main intention of this experiment is to further verify the feasibility of CF-LGMS in achieving sufficiently high separation efficiency for the practical use. For this purpose, the MNP solution was repeatedly pumped into the separator column three times in order to imitate the three-stages series arrangement of CF-LGMS columns. Here, the experiments were conducted by using B4 (Figure 3.6 (d)) and B6 (Figure 3.6 (f)) magnet arrangements where the initial concentration of MNP solution fed into the separator was given by 80 mg/L and 100 mg/L, respectively. The flowrate of the MNP solution was fixed at 10 mL/min.

3.7 Simulation of BW-LGMS and CF-LGMS Processes

In this study, COMSOL Multiphysics (Version 5.1) was used to perform the simulation on the mathematical models that depict the transport behavior as well as kinetics of BW-LGMS and CF-LGMS processes (see Sections 4.2 and 4.3 for the details of the mathematical modelling). In this regard, some simulation details of BW-LGMS and CF-LGMS models are described briefly in this section.

3.7.1 Simulation of BW-LGMS

The geometry of the BW-LGMS process is shown in Figure 3.7, which involves the two-dimensional (2-D) approximation of the real time processes occurring at three-dimensional (3-D) space. In the real time experiments, the container holding the MNP solution is rectangular shaped with dimension of 1 cm (width) × 1 cm (height) × 10 cm (length), whereas the cylindrical magnets employed have diameter D_m of 1.5 cm and height H_m of 2 cm. However, in this mathematical modelling and simulation, the container and magnets are simplified as 2-D rectangles with dimension of 1 cm (height) × 10 cm (length) and 2 cm (height) × 1.5 cm (length), respectively (see Figure 3.7). The 2-D approximation is adopted in the modelling of the magnetic separation processes in this study because it consumes remarkably lower computational resources, without losing much accuracy (Leong, Ahmad and Lim, 2015) (see Appendix A for more detailed discussion).

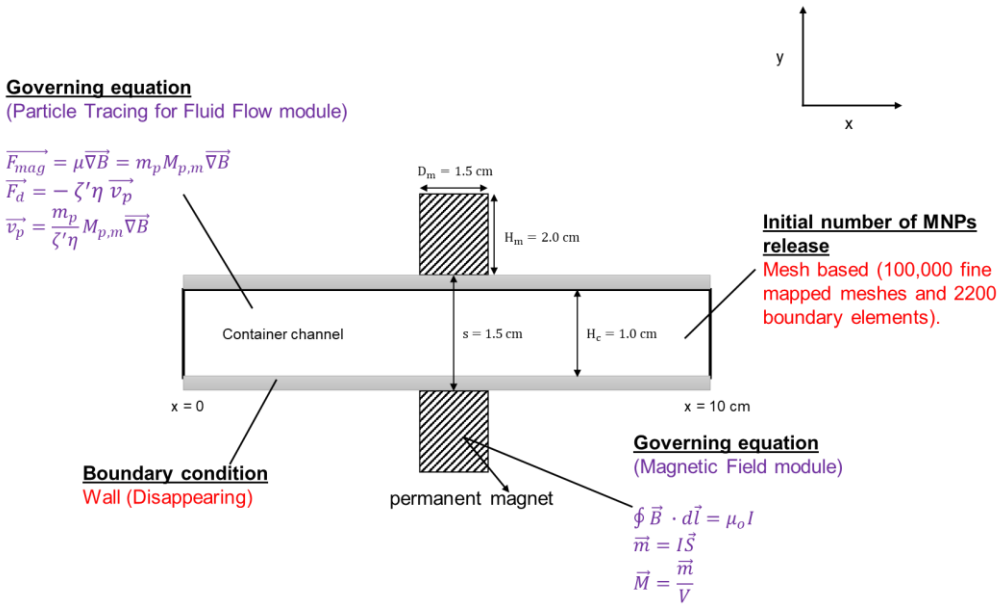

Figure 3.7: Physics and boundary conditions of BW-LGMS model simulation in 2-dimensional space.

The BW-LGMS model was solved by two different modules in COMSOL Multiphysics (Version 5.1): (i) Magnetic Field and (ii) Particle Tracing for Fluid Flow modules via two steps. First, stationary solver was employed to calculate the magnetic field profiles across the magnetic separator by using Magnetic Field module, which was then followed by the application of time-dependent solver in computing the trajectory of particles during magnetophoresis with Particle Tracing for Fluid Flow module (Equations (2.5), (4.1) and (4.2)). The boundary conditions and physics applicable in all domains are illustrated in Figure 3.7, for both modules employed in this study. Prior to the second computational step by using the Particle Tracing for Fluid Flow module, the particles were released into the container domain based on the mesh built across the geometry (100,000 fine mapped meshes and 2200 boundary elements were used in this calculation as shown in Figure 3.8). The results obtained by using this meshing do not have significantly difference as compared to the more refined mesh, which indicates that these meshes are sufficiently fine to generate accurate results for the simulation of this model. The velocity as well as trajectory of MNPs during their migration to the separator wall in the container were then calculated by using the magnetic field gradient generated by the Magnetic Field module from the first step. The 'disappearing' boundary condition was applied to MNPs that are touching with the container wall, which indicates that they have been successfully removed from the solution domain and immobilized on the container wall.

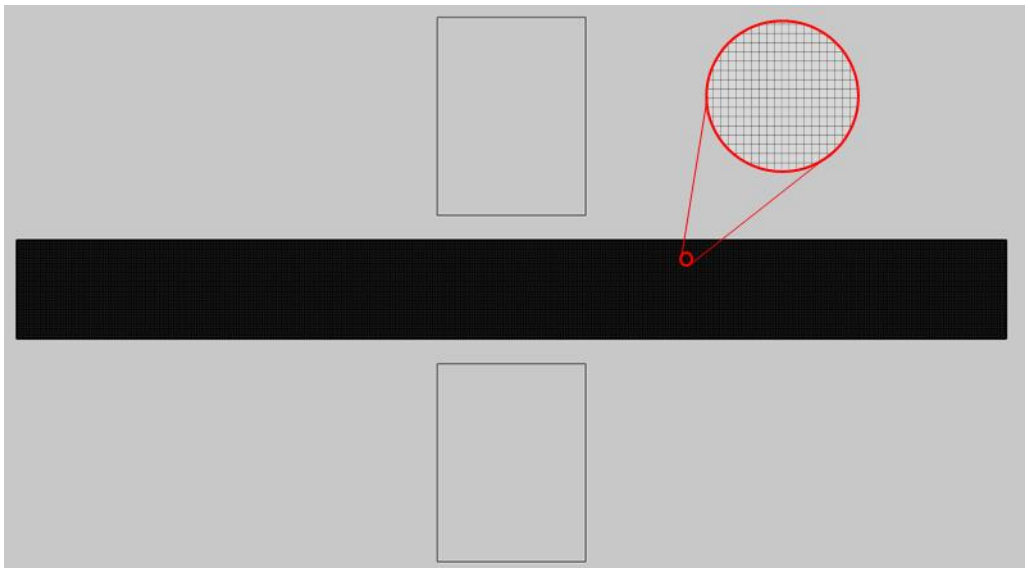

Figure 3.8: Mesh element generated by COMSOL Multiphysics for MNPs released in the container domain.

3.7.2 Simulation of CF-LGMS

In the real time experiments of the CF-LGMS process, the cylindrical magnetic separator column (with 1.6 cm of inner diameter and 10 cm of length) and cylindrical permanent magnets (D_m = 1.5 cm and H_m = 2 cm) are approximated by rectangles with dimension of 10 cm (length) × 1.6 cm (height) and 1.5 cm (length) × 2 cm (height), respectively (Figure 3.9). In addition, the MNP inlet and outlet were defined at the left and right ends of the separator domain, respectively, to represent the MNPs are being bought into and out of the separator by the flowing fluid (Figure 3.9).

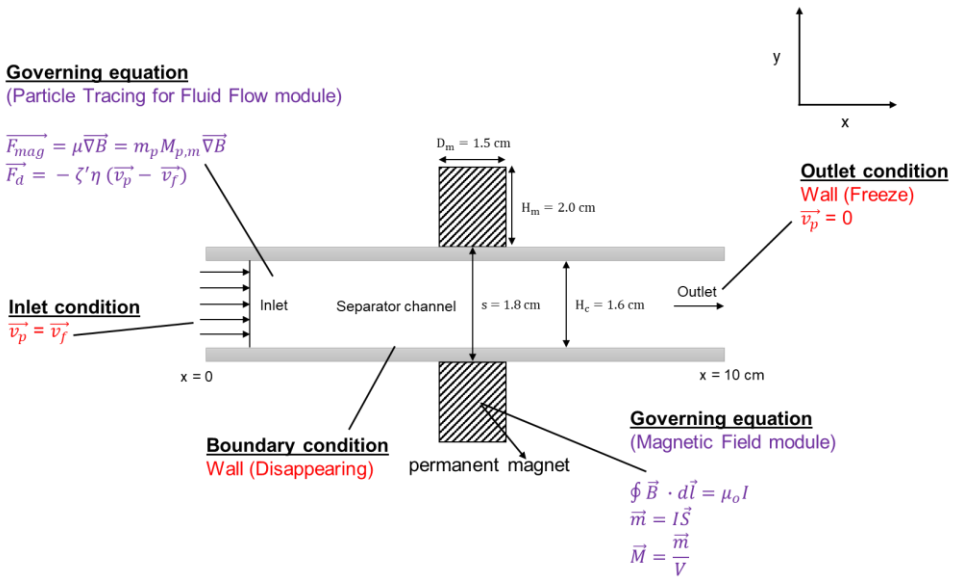

Figure 3.9: Physics and boundary conditions of CF-LGMS model simulation in 2-dimensional space.

Similar to BW-LGMS model, the first step of the simulation involved the generation of the magnetic field profile within the separator column by using Magnetic Field module of COMSOL Multiphysics (Version 5.1). Then, in the second step, the Particles Tracing for Fluid Flow module was used to predict the motion of MNPs within the separator column based on the mesh built across the geometry (100,000 fine mapped meshes and 2200 boundary elements were used in this calculation as shown in Figure 3.8). Prior to the second step of simulation, 100 MNPs (which are uniformly spaced) are released from the inlet boundary, which are moving horizontally (with horizontal (*x*-) component velocity equal to the fluid velocity) and the vertical component (*y*-) of initial velocity is zero upon their release. Throughout their motion in the separator column, MNPs can be deflected towards the top and bottom of the separator column under the effect of magnetophoresis, thus, gaining the velocity along the vertical direction. The horizontal boundaries are defined as the separator wall and the MNP collection plane is allocated for the

horizontal wall adjacent to the magnet. MNPs that are touching the MNP collection plane will disappear from the separator domain, which implies their successful separation from the fluid. The number of MNPs that are not being separated in the column and escape via the outlet boundary will be counted.

CHAPTER FOUR

RESULTS AND DISCUSSIONS

This chapter reports the experimental investigations, mathematical models, simulation results and theoretical discussions related to this study. In Section 4.1, the results of characterization of the MNPs in this study are reported. Next, in Section 4.2, the derivation of mathematical models for BW-LGMS process is thoroughly discussed. Then the comparison between experimental and simulation results of BW-LGMS process is discussed in Section 4.3. In Section 4.4, the transport mechanism that is dominating under CF-LGMS process is determined, which is followed by the derivation of mathematical models to depict CF-LGMS process in Section 4.5. Then the effect of several design parameters of CF-LGMS process (magnet arrangement, particle concentration and flowrate) on the separation efficiency is studied experimentally and theoretically (through model simulation) in Section 4.6. Lastly, the multistage CF-LGMS processes is studied experimentally and theoretically (through model simulation) in Section 4.7 to further verify the feasibility of implementing the CF-LGMS process in real time application.

4.1 Characterization of MNPs

In this section, the results of the MNPs employed in this study are characterized by using scanning electron micrograph (SEM), dynamic light scattering (DLS) and vibrating sample magnetometer (VSM), are reported.

4.1.1 Scanning Electron Microscopy (SEM)

The scanning electron micrograph (SEM) was used to determine the size and shape of the MNPs that used in this study. The micrograph of the MNPs employed in this study is shown in Figure 4.1. According to the micrograph, it can be noticed that the MNPs are almost spherical in shape with average diameter of 44.1 ± 5.3 nm (based on the results obtained from the analysis conducted on 100 randomly picked MNPs by using Image J). Therefore, it can be demonstrated that MNPs have nanometer dimensions and they are appropriate to be used for the current study.

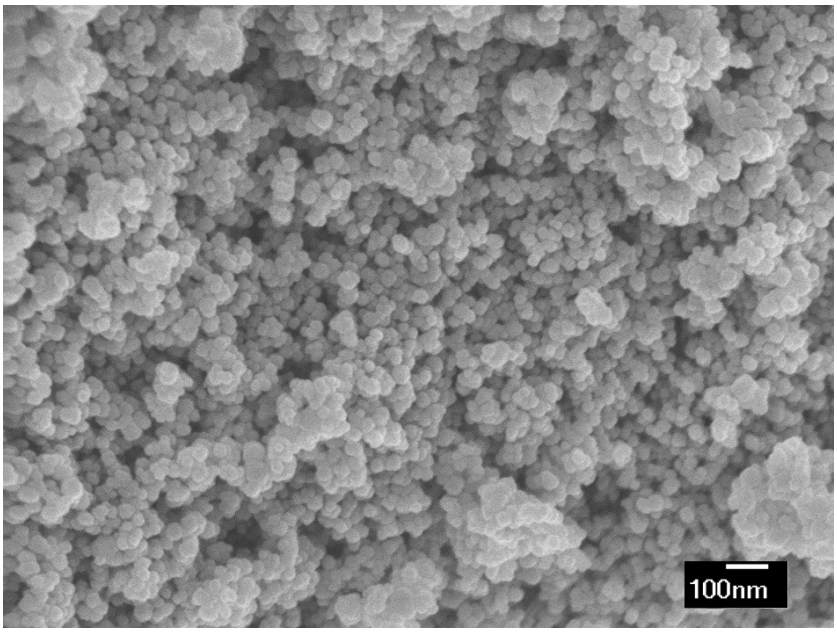

Figure 4.1: SEM image of unmodified MNPs.

4.1.2 Dynamic Light Scattering (DLS)

Figures 4.2 (a) and (b) demonstrate the hydrodynamic size distribution of the unmodified MNP and PSS-functionalized-MNP (which are denoted as MNP clusters in this dissertation, as they are made of MNPs-PSS complex that interlinked among each other and to differentiate it from the magnetic field induced aggregates) resulted from the DLS measurement.

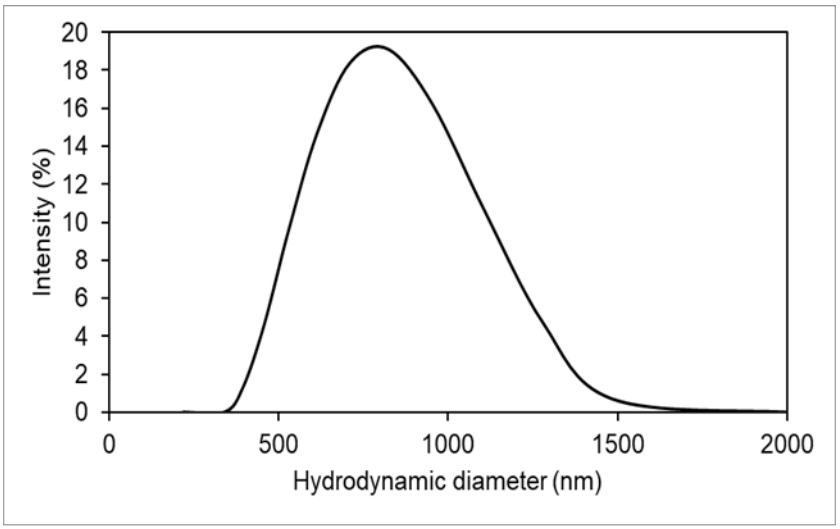

(a)

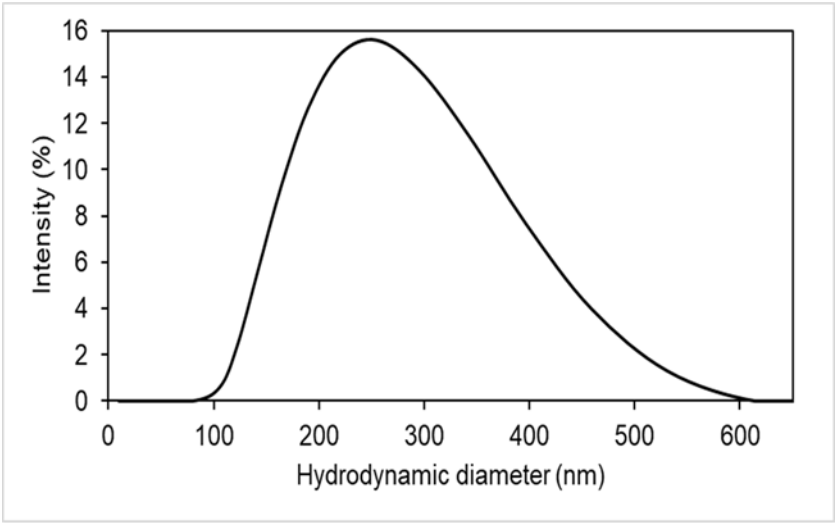

(b)

Figure 4.2: Hydrodynamic diameter distribution of (a) unmodified MNP and (b) PSS-functionalized-MNP from DLS measurement.

The average hydrodynamic diameter of unmodified MNP produced in this study is ~1123 nm with relatively broad distribution ranging from 220 nm to 1400 nm and the intensity peak located at 799.7 nm. The average hydrodynamic diameter measured (~1123 nm) is about 25 times higher than the diameter of individual MNP observed under SEM (~44 nm) which indicates the occurrence of significant agglomeration among MNPs.

Meanwhile, after undergoing surface modification with PSS, the average hydrodynamic diameter of PSS-functionalized-MNP cluster produced in this study has been dramatically declined to ~245.3 nm with distribution ranging from 90 nm to 600 nm and intensity peak at 261.1 nm. Despite of that, the average hydrodynamic diameter of PSS-functionalized-MNP cluster (~245.3 nm) is still about 5-6 times larger than the diameter of individual MNP observed under SEM. The larger hydrodynamic size displayed by the PSS-functionalized-MNP cluster is because the MNP clusters consist of multiple MNPs which are very likely have gone through the bridging flocculation induced by PSS polyanion (Leong et al., 2017).

Although the average hydrodynamic diameter of PSS-functionalized-MNP cluster is larger than the individual MNP (observed under SEM), it displayed smaller size and better colloidal stability as compared to the unmodified MNP system without undergoing functionalization. Without functionalization, the Van der Waals and magnetic dipole-dipole attraction (due to the magnetic moment possessed by MNPs) between unmodified MNPs will cause the formation of larger aggregates that can sediment more rapidly under gravitational field (Golas et al., 2010; Yeap et al., 2012). On the other hand, the PSS layer on the functionalized MNP imparts electrostatic repulsion and steric hindrance among the MNP cluster that prevents further agglomeration of the clusters into larger aggregates (Wu, He and Jiang, 2008; Yeap et al., 2015). Hence, the surface functionalization (or modification) of MNPs with PSS creates sufficient repulsive forces between MNP clusters to minimize the agglomeration of them, which results in a relatively colloidally

stable MNP system that allows the flow profile of magnetophoresis to be effectively captured (Yeap et al., 2018).

4.1.3 Vibrating Sample Magnetometer (VSM)

VSM was employed to measure the magnetic properties of MNPs by calibrating their mass magnetization (magnetic dipole moment per unit mass) at different magnetic field strengths, which allows the determination of the type of magnetism exhibited by the MNPs used in this study. Figures 4.3 (a) and (b) show the VSM measured magnetization curves of both unmodified MNPs and PSS-functionalized-MNP clusters, respectively. According to the results, it can be noticed that the unmodified MNPs present a clear hysteresis loop with coercivity (H_c) of 83.14 Oe and remanent magnetization (M_r) of 8.72 emu/g, which indicates that the particles are non-superparamagnetic in nature. The hysteresis loop also can be clearly observed in the magnetization curve of MNP cluster, but it is slightly narrower with coercivity (H_c) of 73.64 Oe and remanent magnetization (M_r) of 7.93 emu/g. The saturation magnetization of unmodified MNPs and MNP cluster was measured as 70.41 emu/g and 69.48 emu/g, respectively. MNP clusters display slightly lower saturation magnetization values as compared to unmodified MNPs because of the decrease in the mass fraction of the magnetic material (MNPs) after the incorporation of non-magnetic macromolecule during the modification process (Yeap et al., 2014).

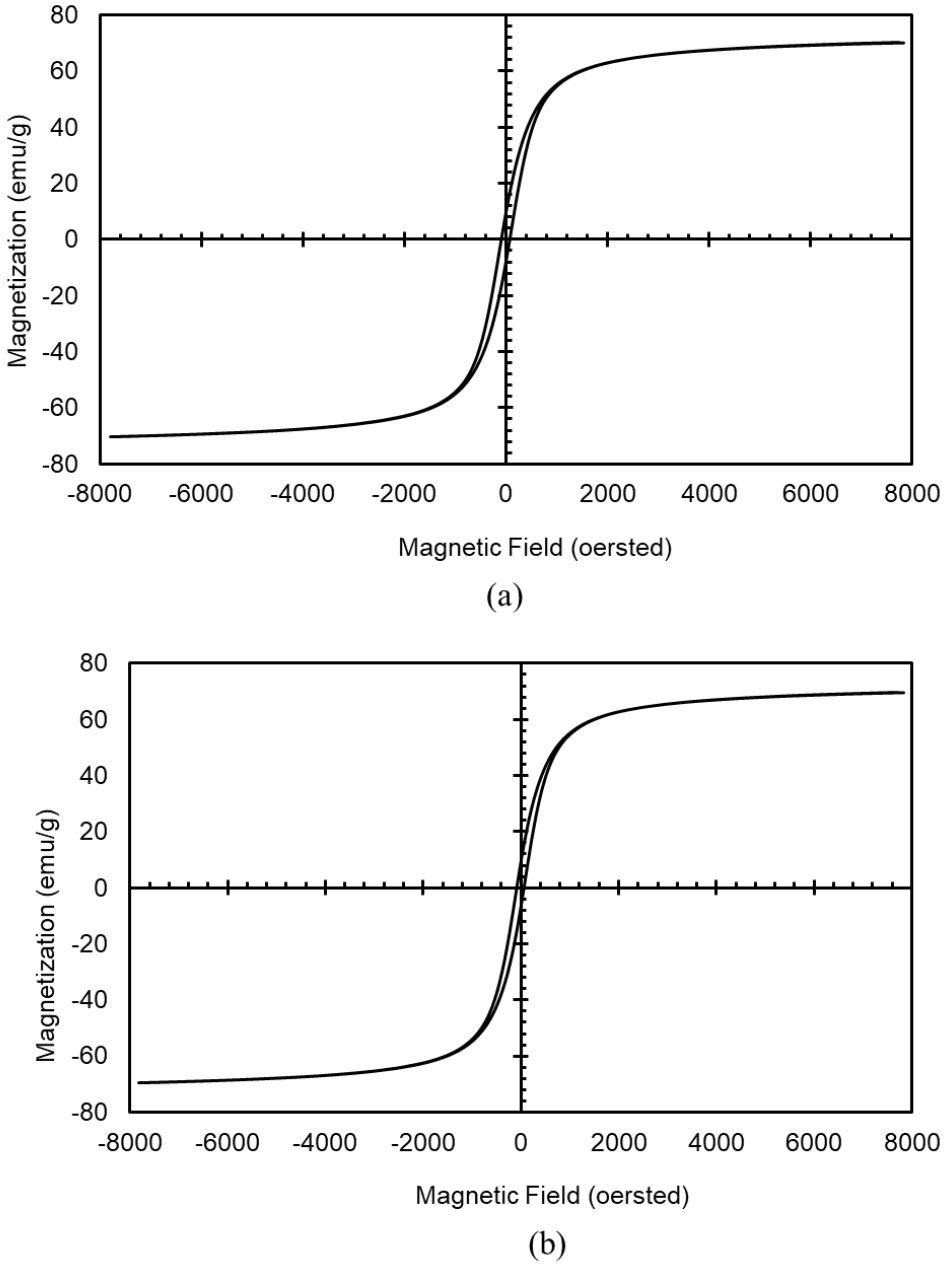

Figure 4.3: Magnetization curve of (a) unmodified MNPs and (b) PSS-functionalized-MNP from VSM measurement.

4.2 Mathematical Modelling of BW-LGMS Process

In order to elucidate the underlying mechanism/principle of magnetic separation experiments conducted in the previous section, mathematical

analysis on the transport behavior as well as kinetics of these processes is needed. In this section, the derivation of mathematical models for BW-LGMS process is thoroughly discussed.

The mathematical model for BW-LGMS process was developed according to the following assumptions: (1) PSS-functionalized-MNP cluster are uniformly distributed throughout the solution at the beginning of magnetophoresis process, (2) all MNP clusters within the separator are subjected to self-aggregation to form larger and elongated MNP aggregates throughout the entire solution (because aggregation parameter $N^* > 1$ in this system (Faraudo, Andreu and Camacho, 2013), as shown in the Appendix B), (3) the aggregation kinetics of MNPs throughout the magnetophoresis is ignored in the modelling as the timescale of particle aggregation (around few seconds) is much shorter than the duration of the magnetophoretic separation (~10 – 20 minutes) (de Las Cuevas, Faraudo and Camacho, 2008; Schaller et al., 2008), (4) the magnetophoretic migration of MNP aggregates in the solution is a creeping motion that obeys Stokes' law (Leong, Ahmad and Lim, 2015), (5) hydrodynamic effect (magnetophoresis-induced convection) is not the dominating effect in the separation processes to be investigated in this study and the fluid is assumed to be stagnant throughout the entire magnetophoresis process (due to the large MNP clusters size and interacting nature of the system that dominate the magnetophoretic scheme), (6) the Brownian motion of MNPs is insignificant as compared to their magnetophoretic motion induced by magnetic field (see Appendix C for the detailed justification), and (7) two-dimensional modelling is performed to

capture the LGMS process occurring in the three-dimensional space (refer to Appendix A for the detailed justification of this approximation).

4.2.1 Magnetic Field

The spatial magnetic field distribution created by permanent magnet(s) throughout the container is calculated by Ampere's Law (Chong et al., 2021) and solved numerically (Wang et al., 2011) by using COMSOL Multiphysics (Version 5.1) Magnetic Field (mf) module. The results from this simulation include the magnetic field strength as well as field gradient profiles with respect to spatial distance (the field gradient profiles generated by different magnet arrangement are indicated in Figure 4.4).

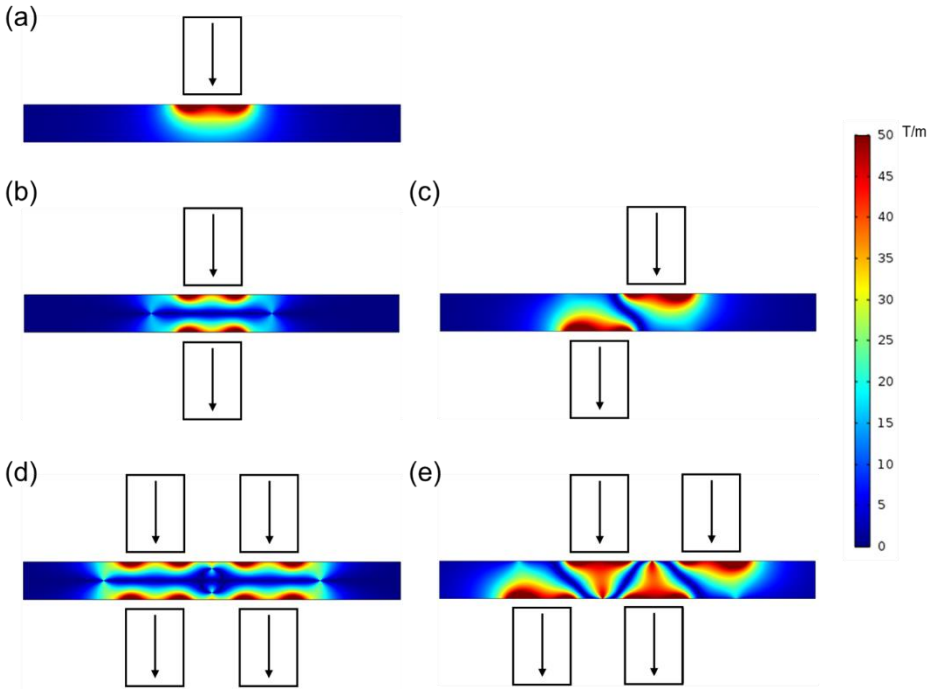

Figure 4.4: The magnetic field gradient *(∂B/∂y)* profiles under BW-LGMS experiments of different magnet arrangements (a) A1 (b) A2, (c) B2, (d) A4, (e) B4. The direction of arrow indicating the magnetization direction of the magnet from south pole to north pole.

4.2.2 Magnetophoretic motion of MNPs

The motion of MNP aggregates under magnetic field is mainly influenced by two main forces: (i) magnetic force and (ii) viscous drag force (Andreu et al., 2012a). Upon exposure to the inhomogeneous (or non-uniform) magnetic field across the container, MNP aggregates experienced magnetic force which can be formulated by Equation (2.5):

$$\overrightarrow{F_{mag}} = \mu \nabla \vec{B} \tag{2.5}$$

In this equation, it has been assumed that the magnetic dipole moment of MNP aggregates always aligns with the direction of magnetic field as it is not fixed in space and could orient freely whilst suspended in the solution. Additionally, throughout its motion in the fluid, the magnetic force imposed on the moving MNP is counter-balanced by viscous drag, which is the resistance resulted from their relative motion with respect to the surrounding fluid (Chong et al., 2021). It should be emphasized that the aggregates of MNP clusters are expected to be of the elongated shape (slender aggregate) due to the dipolar nature of the magnetic interaction leading to particle chaining (Faraudo, Andreu and Camacho, 2013). The expression of viscous drag force acting on a spherical particle is formulated by Equation (2.8), which should be slightly modified for the case of elongated aggregates:

$$\overrightarrow{F_d} = -\zeta' \eta \, \overrightarrow{v_p} \tag{4.1}$$

Here, ζ' is the friction coefficient of MNP aggregate chains (along the long axis), which is dependent on the size of the aggregate (for relationship between ζ' and the aggregate size will be discussed in Section 4.2.3). By applying force

balance on the MNP aggregates and ignore the acceleration term, for following equation is resulted:

$$\overrightarrow{F_{mag}} = -\overrightarrow{F_d} \tag{2.11}$$

After some algebraic arrangement on Equations (2.5), (2.11) and (4.1), the magnetophoretic velocity of MNP aggregates during magnetophoresis is expressed as:

$$\overrightarrow{v_p} = \frac{m_p}{\zeta'\eta} M_{p,m} \overrightarrow{\nabla B} = \frac{\mu}{\zeta'\eta} \overrightarrow{\nabla B} \tag{4.2}$$

The trajectory of MNPs (with a properly defined initial position) under magnetic field can be calculated by solving Equation (4.2) via Particle Tracing for Fluid Flow module in COMSOL Multiphysics (Version 5.1).

It should be noted that the long axis of MNP aggregate chains has been assumed to be aligned along the direction of magnetic field gradient $\overrightarrow{\nabla B}$ (or $\overrightarrow{F_{mag}}$) according to Equations (2.5), (4.1) and (4.2). This approximation has been proven to be valid at the region close to the magnet, where the magnetophoresis of MNP is very significant and dominating the separation kinetics of the entire process, as shown in Appendix D. Such assumptions have simplified the model calculation without losing much accuracy on predicting the temporal behavior of a LGMS process.

4.2.3 Estimating the Physical Properties of MNP Aggregates

This section clarifies the mathematical analysis to determine the size of MNP aggregate during magnetophoresis, within MNP solutions of different concentration. Such a relationship between MNP concentration and aggregate size is needed in the calculation of the trajectory of MNPs within MNP solutions of different concentration. The magnetophoretic velocity from Equation (4.2) can only be solved after knowing the size of MNP aggregates, which can be deduced from the physical properties of the MNP systems employed.

The self-aggregation of MNP clusters is promoted by the magnetic dipole-dipole interaction after their exposure to the external magnetic field and this process is denoted as cooperative effect of magnetophoresis (de Las Cuevas, Faraudo and Camacho, 2008; Andreu, Camacho and Faraudo, 2011). The extent of MNP aggregation is significantly influenced by the properties of MNP system such as particle concentration, magnetization and etc (Andreu et al., 2011; Faraudo, Andreu and Camacho, 2013). Andreu and coworkers have derived a parameter known as aggregation parameter N^* (from thermodynamically approach) to estimate the average number of particles residing in a MNP aggregate based on some critical physical properties of the MNP system (such as volume fraction, particle's magnetization, and size, etc.) (Faraudo and Camacho, 2010; Andreu, Camacho and Faraudo, 2011; Faraudo, Andreu and Camacho, 2013). However, the N^* value predicted from this approach can be very much larger than the actual scenario in many cases, as the duration to achieve the thermodynamic equilibrium of MNPs self-aggregation process can be much longer than the timescale of the

magnetophoresis process. Therefore, this study employed a combined theoretical and experimental approaches to estimate the average number of MNP clusters per aggregate produced within MNP solutions of different concentration but subjected to the similar magnitude of magnetic field strength (de Las Cuevas, Faraudo and Camacho, 2008).

The deduction of aggregate size started with the simple magnetophoresis experimental setup as reported in the previous literature (Leong, Ahmad and Lim, 2015; Leong et al., 2017), which involves the magnetophoresis performed in a rectangular container with a cylindrical magnet being placed underneath it. By assuming the hydrodynamic effect is dominating the overall process (which is the case for most of the magnetophoresis conditions employed in the real time experiments and engineering applications (Leong et al., 2020)), the evolution of MNP concentration $c(t)$ during the magnetophoresis has been proven to obey the first order kinetics, as shown in the following equation (Leong et al., 2017):

$$ln\frac{c(t)}{c_0} = -kt \tag{4.3}$$

Here, c_0 is the initial concentration of the MNP solution, k is the first order rate constant, t is the magnetophoresis duration. By experimentally measuring the extinction profile of magnetophoresis ($c(t)/c_0$ versus t graph) of MNP solutions of different concentration, the respective values of rate constant k (under different MNP concentration) can be deduced from Equation (4.3). Hence, the extinction profile ($c(t)/c_0$ versus t graph) of the magnetophoresis of MNP solutions with different concentration filled in cuvette with dimension of 1 cm × 1 cm × 4 cm was recorded. All magnetophoresis experiments here were

initiated by N50-graded neodymium ferrite boron (NdFeB) cylindrical permanent magnets (4 cm in diameter and 4 cm in length) with the remanent magnetization of 1.45 T (which is producing the magnetic field strength of similar order of magnitude with those of the BW- and CF-LGMS experiments conducted in this study). The extinction profile was then used to calculate the rate constant, which is needed in the estimation of the slender MNP aggregate size under the cooperative magnetophoresis. The concentration of MNP solution was inferred from the light intensity data acquired from the analysis on the time-lapsed images taken on MNP solution throughout the magnetophoresis process (by using ImageJ software). Thus, a calibration experiment was first conducted to correlate the light intensity to the concentration of MNP solution. The pictures of different concentrations of MNP solution: 0 mg/L (pure water), 20 mg/L, 40 mg/L, 60 mg/L, 80 mg/L and 100 mg/L were taken, and the light intensity across the MNP solution was measured by using ImageJ software. Figure 4.5 presents a calibration graph of light intensity against MNP concentration. As shown in this figure, light intensity increases approximately linear with MNP concentration within the concentration range of 0 to 100 mg/L, and the coefficient of determination R^2 is 0.9972. Therefore, it has been proven that the intensity of the MNP solution (obtained from ImageJ) is changing almost linearly with respect to the concentration of MNP solution.

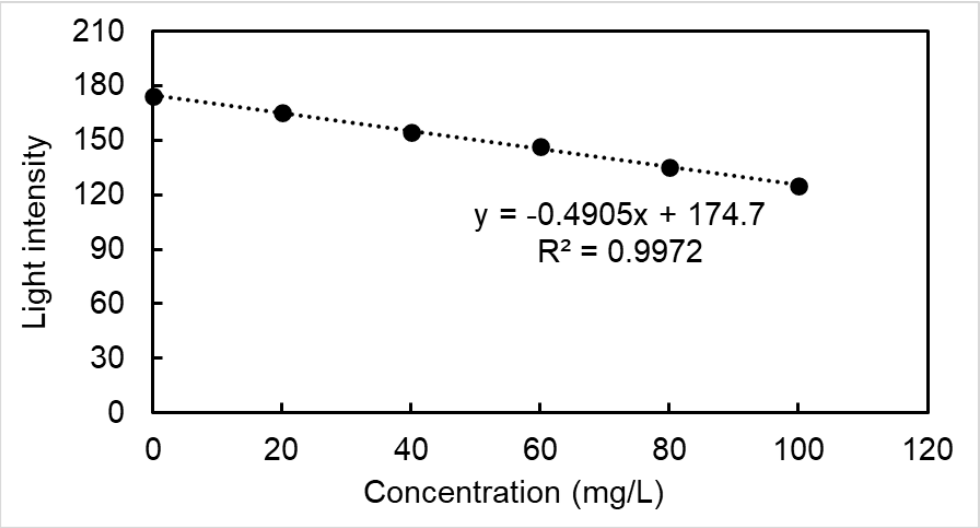

Figure 4.5: The calibration curve of initial concentration with light intensity generated by ImageJ.

After that, the time lapse images of MNP solution captured in the real time magnetophoresis were analyzed by using ImageJ software to acquire the light intensity which was then used to calculate the concentration of the MNP at a particular time (by using the calibration graph in Figure 4.5). The separation kinetic profiles for magnetophoresis of MNP solution of different initial concentration under magnetic field generated by magnet were tabulated in Figure 4.6. The coefficient of determination R^2 and gradient k (rate constant) of the curve (by making simple linear regression) are tabulated in Table 4.1. The values of rate constant k obtained were used to calculate the size of MNP aggregates, as shown in the following paragraphs.

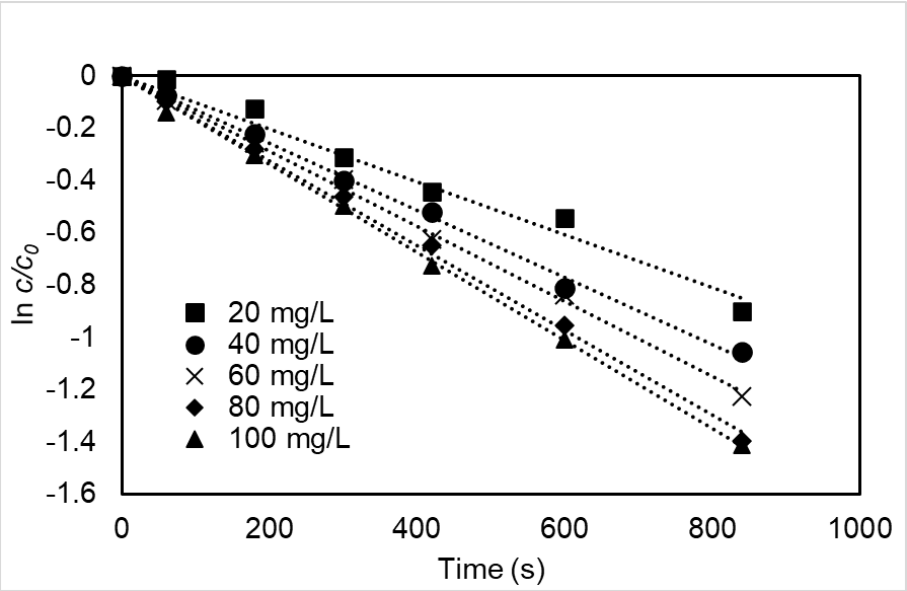

Figure 4.6: $ln\frac{c}{c_0}$ versus time graphs for magnetophoresis experiments conducted with MNP solutions of different initial concentration. Dotted lines are the linear fittings of the scattered data.

Table 4.1: The tabulation of rate constant *k* (measured from the gradient of $ln\frac{c}{c_0}$ against time graph) and coefficient of determination R^2 evaluated from the extinction profiles of magnetophoresis of MNP solution with different initial concentration.

Initial MNP Concentration (mg/L)	Rate constant, *k* (s^{-1})	Coefficient of determination, R^2
20	0.001051	0.9851
40	0.001255	0.9967
60	0.001382	0.9978
80	0.001592	0.9984
100	0.001766	0.9886

According to Table 4.1, it can be observed that the R2 values for all experiments are greater than 0.985, which indicates that the concentration decay is obeying the first order kinetics. With the values of rate constant

obtained from these experiments, the magnetophoretic velocity of MNPs (which are in the form of MNP aggregates) at the MNP collection plane $v_y(y = 0)$ can be estimated as follows (Leong et al., 2017):

$$v_y(y = 0) = \frac{k\, V_s}{A_s} \tag{4.4}$$

where V_s is the volume of MNP solution subjected to magnetophoresis and, A_s is surface area of collection plane (which is the bottom wall of the container). Based on the slender body theory, the longitudinal friction coefficient of the chain-like MNP aggregates can be determined as follow (Faraudo and Camacho, 2010):

$$\zeta' = \frac{2\pi N d}{ln(2N) - \frac{1}{2}} \tag{4.5}$$

where *d* is the diameter of the MNP clusters and *N* is the number of MNP clusters per aggregate. By applying the force balance of MNPs (magnetophoretic and viscous drag forces) at the collection plane (y = 0), the following expression can be obtained after some algebraic rearrangement:

$$\frac{\mu}{\zeta'} = \frac{v_y(y = 0)\eta}{\nabla B|_{y=0}} = \frac{N\mu_1}{2\pi N d}\left(\ln(2N) - \frac{1}{2}\right) \tag{4.6}$$

where $\nabla B|_{y=0}$ is the magnetic field gradient at the collection plane (y = 0) and μ_1 is the magnetic dipole moment carried by one MNP cluster (see Appendix E for the details of calculation). The total magnetic dipole moment possessed by one MNP aggregate can be expressed as:

$$\mu = N\mu_1 \tag{4.7}$$

where μ_1 the magnetic dipole moment exhibited by one MNP cluster. The number of MNP cluster in one MNP aggregate, *N* can be calculated by solving

Equation (4.6) with the values of v_y (y = 0) that were calculated according to the rate constant k (by using Equation (4.4)) that was obtained experimentally.

4.3 Transport Mechanism that Dominates the BW-LGMS Process

For the case of BW-LGMS process, the time-dependent concentration distribution of MNP solution (filled in batch container) subjected to magnetophoresis under different magnet arrangement (Figure 3.2) were observed and investigated. The experimental results were then compared with the outcomes from the simulation of BW-LGMS model. This study is particularly crucial in elucidating the transport mechanism that is dominating the magnetic separation process of the MNP system used in this study.

4.3.1 Profile of Magnetic Field and Magnetic Force

Before analyzing the results of BW-LGMS experiments, it is necessary to interpret the magnetic field gradient profile generated within the container filling with MNP solution, by the magnet arrays of different arrangement. It should be noted that such profile is consistent for either batch or continuous case, hence, the particle located in the same position within the system will experience the same magnetic field (and if their magnetic mass is the same then they would be experiencing the same magnetic force). The contour plot in Figure 4.7 is showing the partial derivative of magnetic field strength, B along

the vertical direction ($\partial B/\partial y$), which is the major driving force that steers the MNPs to move vertically (either upwards or downwards) towards the magnets and leads to their separation.

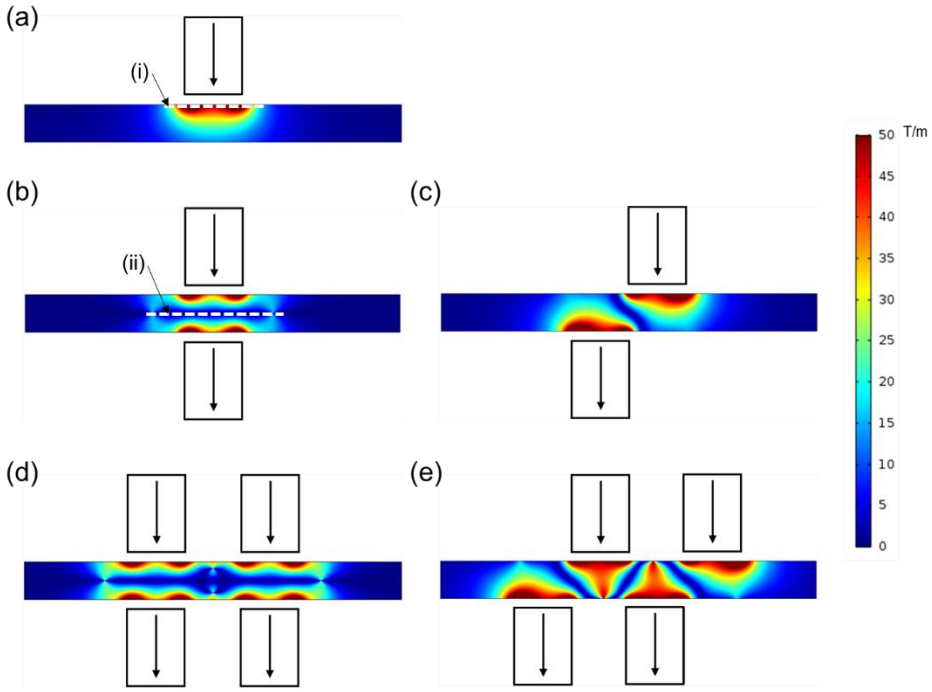

Figure 4.7: The magnetic field gradient *(∂B/∂y)* profiles under BW-LGMS experiments of different magnet arrangements (a) A1 (b) A2, (c) B2, (d) A4, (e) B4.

It is obvious from Figure 4.7 that the magnetic field profile across the MNP solution is significantly influenced by the number as well as the relative position of the magnets at the surrounding. According to Figure 4.7 (a), the magnetic field gradient is more intense at the region adjacent to the magnet pole (~45.456 T/m, which is the average value along the white dotted line labelled as (i) for Figure 4.7 (a)), as indicated by the dark red coloration around this region. When two magnets are being arranged in aligned orientation as shown in Figure 4.7 (b), the magnetic field gradient in the gap between the two magnets can be much lower (~0.0014 T/m which is the average value along the

white dotted line labelled as (ii) for Figure 4.7 (b)). This phenomenon is due to the more uniform magnetic field in between both magnets, which subsequent renders the magnetic field gradient to be lower. For the scenario in which the two magnets are slightly displaced horizontally (misaligned orientation) as presented in Figure 4.7 (c), the low magnetic field gradient region is forming an inclined angle with the horizontal direction (the inclined blue strip in the contour plot of Figure 4.7 (c)), due to the relatively more uniform magnetic field around this area. As the number of magnets is increased to 4, as shown in Figure 4.7 (d) and (e), the magnetic field gradient profile is showing the similar pattern, however, there is a larger portion of the container residing within the higher magnetic field zone. Such features have a very substantial influence on the magnetic separation efficiency, since the MNPs migrated from low field gradient zone to high field gradient zone.

Apart from that, Figure 4.8 (a) shows the tabulation of the horizontal component of magnetic force F_x encountered by MNP clusters along the horizontal lines at the center of the separator column (as indicated in Figure 4.8 (b) – (d)), induced by the magnetic arrays of different arrangement. It also should be noted that the positive and negative values of F_x indicate the magnetic force exerted on the MNP cluster is directing towards the right and the left of the separator, respectively (Gassner et al., 2009). Under misaligned magnet orientations (Figure 4.8 (c)), the horizontal component of magnetic force F_x experienced by MNPs is relatively smaller (indicated by the lower peaks of curves (ii) and (iii) in Figure 4.8 (a) with magnitude of ~1.26489×10^{-13} N and ~1.69197×10^{-13} N, respectively) as compared to those subjected to magnet system with aligned orientation (the peak of curves (i) and (iv) in

Figure 4.8 (a) shows magnitude of ~2.68634×10^{-13} N and ~2.57035×10^{-13} N, respectively). The results tabulated in this figure is required to explain the experimental observation of BW-LGMS process in the subsequent subsections.

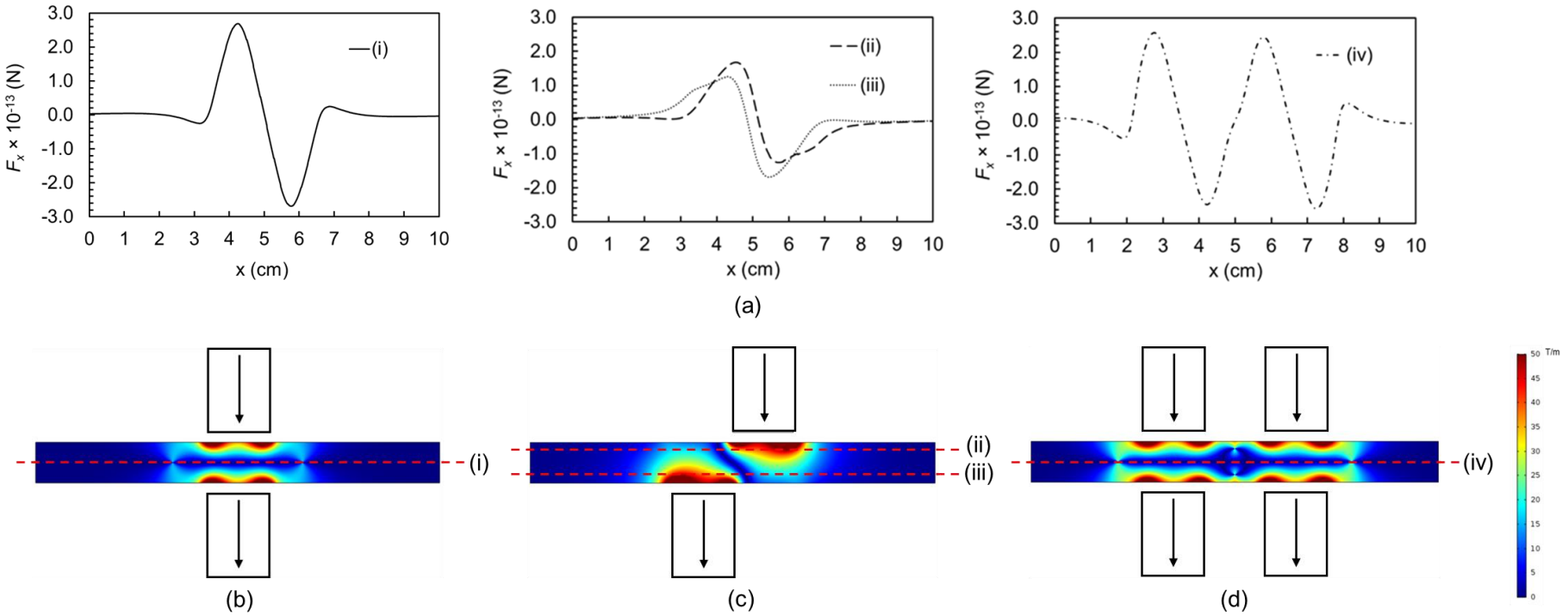

Figure 4.8: (a) The graphs of the *x*-component of magnetic force under BW-LGMS along the dotted lines (i) to (iv) in Figures (b) – (c). Contour plot of magnet field gradient throughout the container for magnet arrangements (b) A2, (c) B2, (d) A4.

4.3.2 Transient Analysis on the Distribution of MNP under BW-LGMS

The time lapsed images of MNP solution under the BW-LGMS experiment was indicated in Figure 4.9, which were performed under different magnet arrangements as indicated in Figure 3.2. In addition, Figure 4.10 presents the same results, which is produced by the simulation of BW-LGMS model as described in Section 4.2.

By using A1 magnet arrangement (only a single magnet located at one side of the container), the MNPs were progressively being collected from the solution starting from the area closer to the magnet. This scenario caused the formation of a clear convex boundary towards the magnet that separates the region of high and low particle concentration (see Figure 4.9 (a)). In this region, the magnetic force experienced by the MNPs is sufficiently large to induce their rapid separation from the solution, as compared to MNPs which are initially located at the region further away from the magnet. This finding is also consistent with the simulation results (see Figure 4.10 (a)) but with more distinctive concentration contrast. It is very likely that this observation is due to the occurrence of hydrodynamic effect in the BW-LGMS experiment, in which the magnetophoresis induced convection has been generated to homogenize the MNP solution and renders the clear-cut boundary observed in the experiment to be less sharp. On the other hand, the hydrodynamic effect is not considered in the simulation, thus, the much sharper boundary is observed owing to the absence of induced convection.

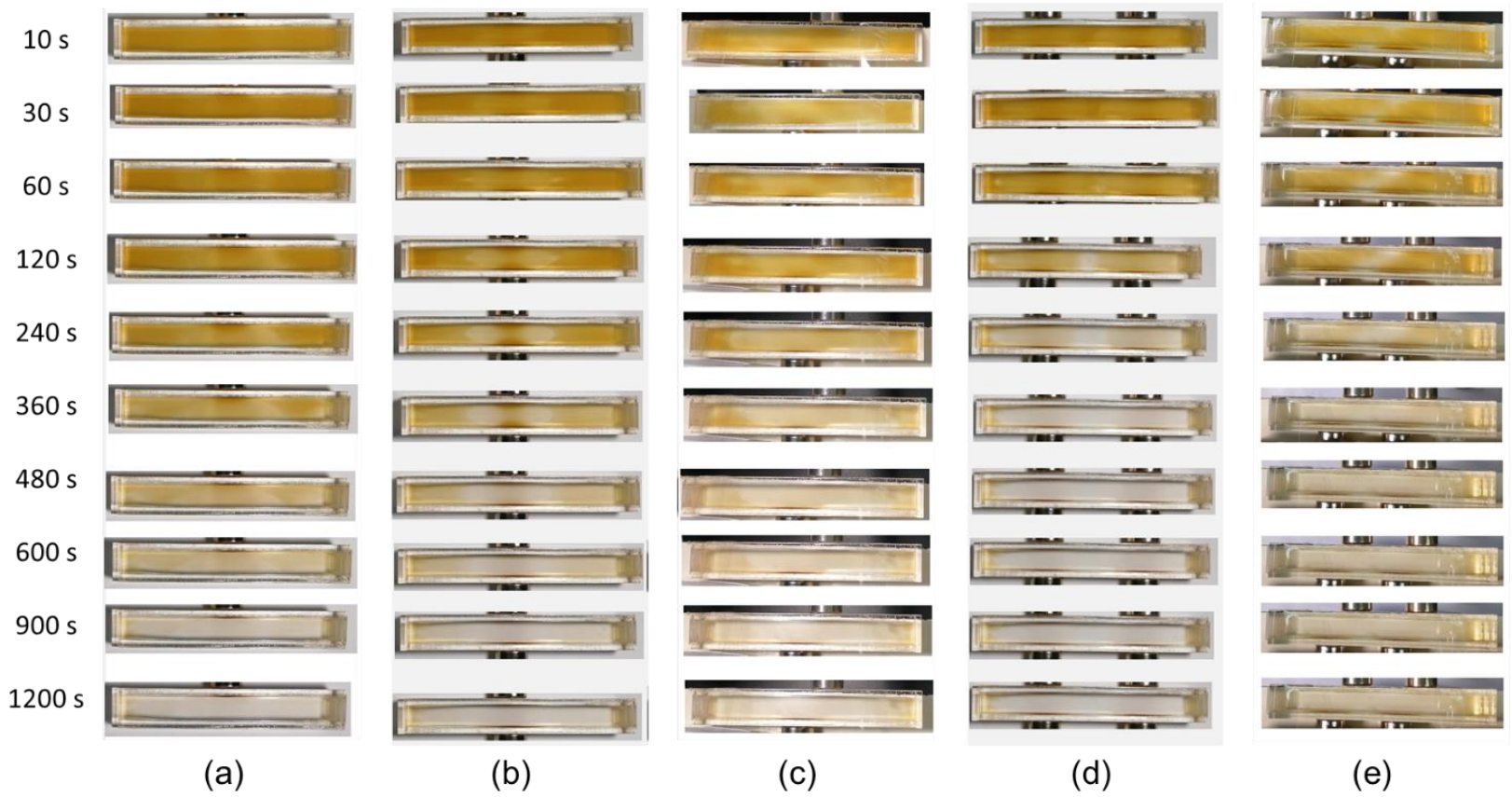

Figure 4.9: Time lapse images for MNP solution under BW-LGMS experiment induced by different magnet arrangements (a) A1 (b) A2, (c) B2, (d) A4 and (e) B4.

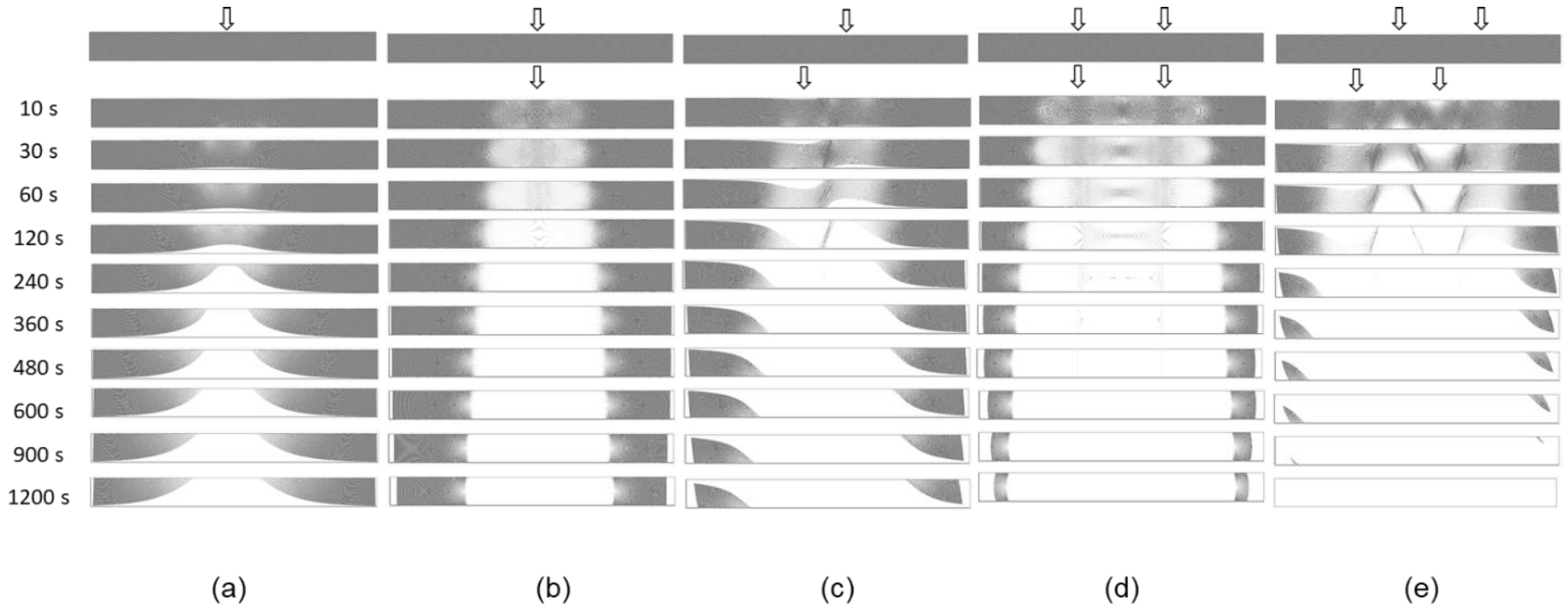

Figure 4.10: Time lapse images of 2-D particle distribution across the MNP solutions under BW-LGMS simulation induced by different magnet arrangements (a) A1 (b) A2, (c) B2, (d) A4 and (e) B4.

In addition, there is a huge deviation between the experimental and simulation results at the left- and right-ends of the MNP solution, where the magnetic field gradient is relatively low. This is attributed by the dominance of hydrodynamic effect at these regions under the real-time experiments, in which the induced convective current (typically in the order of magnitude of 10^{-5} – 10^{-4} m/s according to the previous study using the similar magnetophoresis system) is much faster as compared to the magnetophoretic velocity of individual MNP cluster (10^{-8} – 10^{-7} m/s according to simulation) (Leong, Ahmad and Lim, 2015). Therefore, the induced current will continuously sweep the MNPs from the far end towards the central region (with higher magnetic field) much more rapidly.

The employment of two magnets gives the different distribution of MNPs across the MNP solution throughout the BW-LGMS process (see Figure 4.9 (b) and (c)). Upon subjected to A2 magnet arrangement for about half minute, the MNPs near the edges of the magnets (regions labelled with B in Figure 4.11 (a)) were being collected first, whereas most of the MNPs within the region in between the magnet poles (region labelled with A in Figure 4.11 (a)) remained uncollected as indicated by remaining darker solution (higher MNP concentration). This is because Regions B have the higher magnetic field gradient as compared to Region A under this magnet configuration (see Figure 4.7 (b)), thus, MNPs residing within the Regions B (near the edges of magnet) can be separated more rapidly as compared to those located in Region A (in between the edges of magnet). In addition, this observation also can be rationalized by the nature of horizontal magnetic force generated by this magnet arrangement (see curve (i) in Figure 4.8), in which the MNPs at

Regions B are being driven horizontally and squeezed towards the Region A during the BW-LGMS process (see the red arrows in Figure 4.11 (a)). On the other hand, under B2 magnet arrangement, the regions labelled with C in Figure 4.11 (b) experienced the more rapid clearance of MNPs, due to the higher horizontal magnetic force that drives them towards the regions labelled with D (see curves (ii) and (iii) in Figure 4.8).

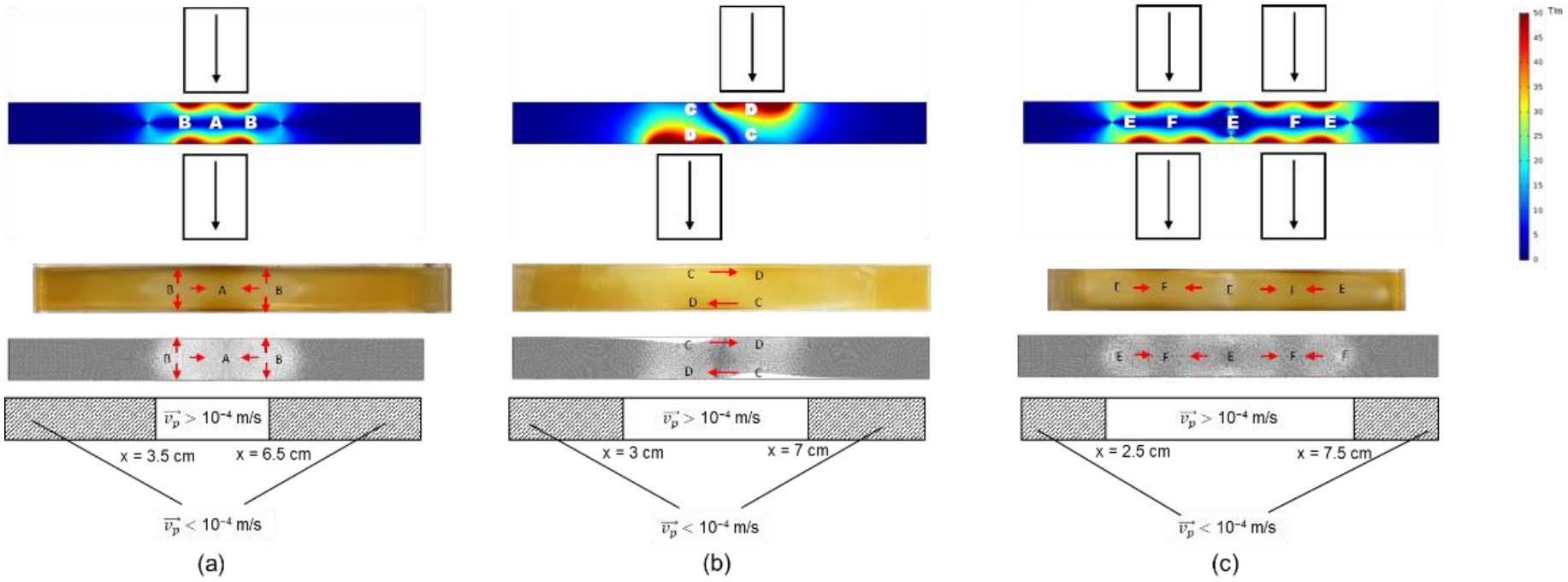

Figure 4.11: Contour plot of magnet field gradient as well as the comparison between experimental and simulation results of MNP distribution induced by magnet arrangement (a) A2, (b) B2 and (c) A4.

Also, for both A2 and B2 cases, the pattern of the MNP distribution resulted from the simulation of BW-LGMS also in agreement with the experimental observation at the region in the vicinity of the magnets. For instance, under A2 magnet configuration, there are two lobes with lower concentration being observed near the edges of the magnets for both experimental and simulation results (see Figure 4.11 (a)). However, huge discrepancy was observed for the MNPs distribution at the far end of the container (far from the magnets) between the experimental and simulation results, in which the experiments always show the faster MNPs clearance at these far-end regions (see Figures 4.9 (b)-(c) and Figures 4.10 (b)-(c)). Similar to the experiment with A1 magnet arrangement, this phenomenon is caused by the hydrodynamic effect that is dominating at the far-ended regions with very low magnetic field gradient (~0.01 T/m).

Therefore, the MNP solution domain in this study can be categorized into two regions: (i) near-to-magnet region where the inertial force is dominating (obeys with classical magnetophoresis theory); and (ii) far-end region where hydrodynamic effect is dominating. This region classification is illustrated in Figures 4.11 (a) – (b). Here, in this study, the near-to-magnet region is denoted as the region where $\left|\overrightarrow{v_p}\right| > 10^{-4}$ m/s (magnetophoretic velocity of individual MNP is dominating) and the far-end region is denoted as the region where $\left|\overrightarrow{v_p}\right| < 10^{-4}$ m/s (induced convection is dominating). In this classification, it has been assumed that the induced convective current is having velocity of 10^{-4} m/s, a typical value found in the simulation work by Leong and coworkers (Leong, Ahmad and Lim, 2015).

Some discrepancies between experimental observation and simulation results can be explained by applying this concept. For instance, under A2 magnet arrangement, the simulation predicts MNPs at the near-to-magnet region have been almost completely cleared out at t = 240 s (Figure 4.10), however, there are still significant amount of MNPs being observed in this region experimentally at the same time (Figure 4.9). This phenomenon is due to the migration of MNPs from the far-end region into the near-to-magnet region at a much faster rate in the experiment (due to the sweeping flow of induced convection), which causes the MNPs at the near-to-magnet region to deplete more slowly than those predicted by the model simulation. In the simulation, the MNPs at the far-end region are moving very much slower at their own magnetophoretic velocity (~10^{-6} m/s), however, the much faster magnetophoresis induced convection (~10^{-4} m/s) is present at these regions in the real time experiments. Therefore, from the experimental observation, the MNP concentration at far-end region drops much rapidly (typically being cleared up after 1200 seconds of magnetophoresis), as indicated in Figures 4.9 (b) and (c). On the other hand, there are still significant amount of MNPs residing at the far-end regions after 1200 s of magnetophoresis according to the simulation results, as shown in Figures 4.10 (b) and (c).

The magnet configurations with higher number of magnets (A4 and B4) also give the similar outcome. For instance, under A4 magnet configuration, the MNPs at Regions E (see Figure 4.11 (c)) are being cleared out more rapidly, due to the magnetic force that squeezes the MNPs horizontally towards the Regions F (see curve (iv) in Figure 4.8 (a)). Furthermore, since there are higher proportion of MNP solution that are immersed in the relatively more intense

magnetic field in which the transport behavior of MNPs is dominated by inertial force, the simulation results give the better agreement with the experimental observation in overall.

4.4 Analysis on the Transport Mechanism of CF-LGMS Process

From the comparison between the experimental and simulation results of BW-LGMS processes, it is apparent that the mathematical model developed in Section 4.2 (in which hydrodynamic is being neglected) is only applicable at near-to-magnet region where the magnetic field is relatively intense. In order to mathematically describe the CF-LGMS process, it is necessary to elucidate the transport mechanism that is dominating the motion of MNPs subjected to the given process. In this section, the dominating transport mechanism of the CF-LGMS process is deduced from the outcomes of the experimental and theoretical study on the BW-LGMS process, as reported in the previous sections.

From BW-LGMS experiments, it can be estimated that the timescale for the hydrodynamic effect to aid the collection of the MNP system employed in this study is ~20 minutes (1200 seconds). Evidently, it can be observed from Figure 4.9 that almost all MNPs (even at the far-end regions) have been collected after 20 minutes (1200 seconds) of magnetophoresis, under all magnet configurations. In the CF-LGMS experiments to be conducted in this study (as described in Section 3.6), it can be calculated that the residence time of MNPs in the separator column is ~4 minutes even for the experiment that

employs the lowest flowrate (5 mL/min). This timescale is about 5 times shorter than the timescale for the hydrodynamic aided separation of MNPs that initially located at the far-end of the column (for this case it is ~5 cm away). Therefore, in the CF-LGMS process conducted in this study, the residence time of MNP solution is too short for the hydrodynamic effect to accelerate the separation process.

In addition, it also has been revealed from previous works done by Leong and coworkers that the magnetophoresis induced convective current can be about 10^{-4} m/s at the far-end region with very low magnetic field gradient (Leong, Ahmad and Lim, 2015). In fact, this induced convective current is much (~4 times) slower than the velocity of the carrier fluid (forced convection), which is calculated as $\sim 4 \times 10^{-4}$ m/s for the lowest flowrate being employed in this study. Therefore, by comparing the magnitude of induced and forced convective flow, it also suggests that the magnetophoresis induced convection resulted from hydrodynamic effect is relatively trivial as compared to the forced convection generated by the flowing fluid. Up to this stage, it is reasonable to deduce that hydrodynamic effect is not an important factor to be considered for the CF-LGMS process, in particular for the MNP system that is being employed in the current study due to two reasons: (i) the residence time of MNP solution within the continuous flow separator column is too short for the hydrodynamic effect to be effective and (ii) the forced convection is much rapid than the magnetophoresis induced convection.

As the cooperative effect is instantaneous (the magnetically induced self-aggregation of MNPs is rapid as shown in Figure 2.6 (c)) and hydrodynamic effect requires the longer duration than the residence time of

MNP solution within the CF-LGMS column, the model that describes the separation kinetics of CF-LGMS process was developed by considering the self-aggregation of PSS-functionalized MNP clusters and neglecting the occurrence of magnetophoresis induced convection. The mathematical modelling of CF-LGMS process is elaborated in the next section.

4.5 Mathematical Modelling of CF-LGMS Process

The mathematical model on CF-LGMS processes is modified from the BW-LGMS model. Similarly, the 2-D approximation of the 3-D CF-LGMS process is applied here with the same magnetic field setup as BW-LGMS model. The computation of the magnetic field profile across the separator would be the same as the physics (Ampere's Law) that was applied in the BW-LGMS model, by using the Magnetic Field module of COMSOL Multiphysics. Similar to BW-LGMS model, the trajectories of MNP aggregates across the separator column are also computed by Equations (2.5), (4.1) and (4.2), embedded in the Particle Tracing for Fluid Flow module. However, in CF-LGMS process, $\overrightarrow{v_f}$ is non-zero owing to the flowing fluid across the separator column (Cao, Han and Li, 2012; Forbes and Forry, 2012), and its value is estimated by the volumetric flowrate by adopting the uniform flow assumption. The number of MNP that are escaped via the outlet boundary of the separator column is counted so that the separation efficiency can be computed as follows:

$$Separation\ efficiency, \eta' = \frac{N_{p,o} - N_p}{N_{p,o}} \tag{4.8}$$

where $N_{p,o}$ is the number of MNPs released to separator and N_p is the number of MNPs that escape from the separator column. However, due to the 2-D approximation of the model, it is crucial to correct the separation efficiency in Equation (4.8) by a function f_c to encounter for the geometrical effect under the actual 3-D cylindrical column. In the 2-D approximation in the simulation of CF-LGMS process, the separator column in rectangular shaped. Nevertheless, in reality, the separator column is of cylindrical shaped with circular cross-sectional area shown in Figure 4.12.

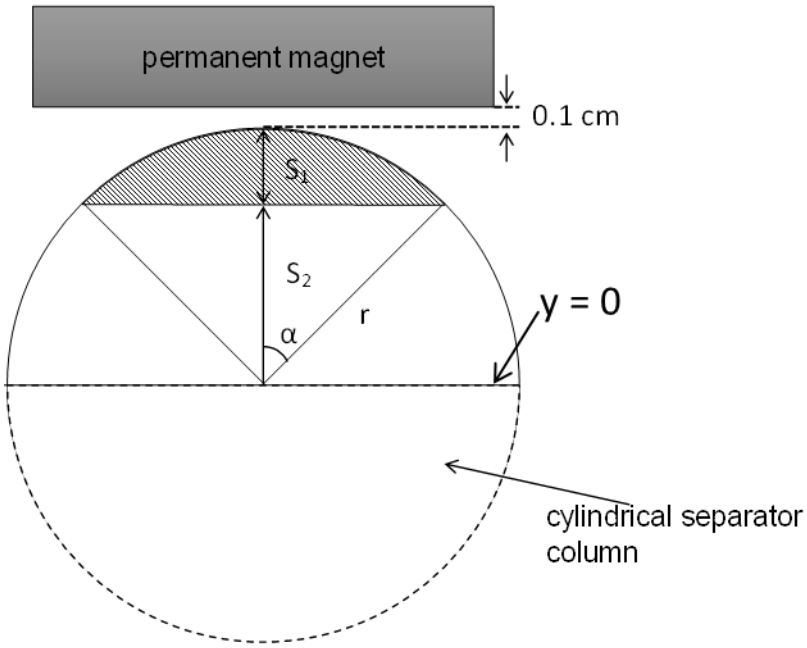

Figure 4.12: Cross-sectional view of the cylindrical separator column.

Therefore, the number of MNPs are not distributed linearly along the vertical diameter of the cross-sectional area of the separator column, as there are more MNPs appear around $y = 0$ (at the middle of separator column) than those regions with greater magnitude of y (closer to the magnets or column

wall). If there is no correction factor applied on Equation (4.8), the separation efficiency will be overestimated as the MNPs at the central region (which appear in the greater amount) are more difficult to be separated/captured. Hence, it is essential to incorporate such geometrical effect in calculating the actual separation efficiency of CF-LGMS process so that the accuracy of the simulation result can be improved.

Figure 4.12 shows the cross-sectional view of the cylindrical separator column, in which the magnet is placed to the separator column with 0.1 cm spacing and the radius of the separator column is given by *r* cm. The following derivation only focuses on the semicircle due to the symmetrical feature of the circular cross-sectional area along the horizontal (or any other) diameter. By assuming the MNPs that are initially located at the shaded region (region closer to magnet) is successfully separated from the solution, the separation efficiency calculated by Equation (4.8) is:

$$\eta' = \frac{S_1}{S_1 + S_2} = \frac{S_1}{r} \tag{4.9}$$

where S_1 and S_2 are the length of segments along the circular radius (see Figure 4.12). As the separator is of cylindrical shaped, the actual separation efficiency should be the percentage of the shaded region in the semicircle. Here, the area of the shaded segment can be determined as follow:

$$A_{s1} = \frac{1}{2} \times r^2 \times (\theta - \sin\theta) \tag{4.10}$$

where the $\theta = 2\alpha$ (in radians) and α can be calculated as follow:

$$\alpha = \cos^{-1}(S_2/r) = \cos^{-1}(1 - \eta') \tag{4.11}$$

Then the actual/corrected separation efficiency, η is calculated by using the following function:

$$\eta = \frac{2 \times A_{s1}}{\pi r^2} = \frac{(\theta - \sin\theta)}{\pi} \tag{4.12}$$

$$= \frac{\cos^{-1}(1-\eta') - \sin[\cos^{-1}(1-\eta')]}{\pi} = f_c(\eta')$$

4.6 Effect of Critical Design Parameters on the Separation Efficiency and Transport Behavior of CF-LGMS

In this section, the effect of several design parameters of CF-LGMS process (magnet arrangement, particle concentration and flowrate) on its separation efficiency is first studied experimentally. Then, the similar process also simulated by using the model (in Section 4.5) discussed. The experimental and simulation results are then compared to verify the accuracy of the mathematical model developed in Section 4.5. Lastly, the trajectory and transport behavior of MNPs within the separator (from simulation results) are also being presented and discussed.

4.6.1 Effect of Magnet Configuration

The separation efficiencies (with two trials experiments) obtained from CF-LGMS experiments (Sets 1 to 6 of Table 3.3) are tabulated in Figure 4.13. As shown in Figure 4.13, it can be noticed that the separation efficiency increases with the number of magnets, under the same type of magnet arrangement. For

instance, it has been observed that the magnet arrangement of B6 (six magnets) has higher separation efficiency (with average value of 56.70%) as compared to the situations when two magnets (with average value of 22.22% for magnet arrangement of B2) and four magnets (with average value of 38.51% for magnet arrangement of B4) were used. This observation aligned well with the conventional belief in which increasing the number of magnets can boost the separation efficiency as higher volume of the CF-LGMS separator is within the influence of strong magnetic field (Khashan and Furlani, 2014). On the other hand, by comparing among the same number of magnets, magnet arrangement of B6 (misaligned arrangement) showed the slightly higher separation efficiency as compared to the aligned arrangement (with average value of 55.98% for magnet arrangement of A6). Such observation is also consistent with the high coverage magnetic field argument (the coverage imposed by misaligned magnet arrangement is greater than aligned magnet arrangement, as indicated in Figure 4.7) is playing a role in enhancing the separation efficiency of CF-LGMS process.

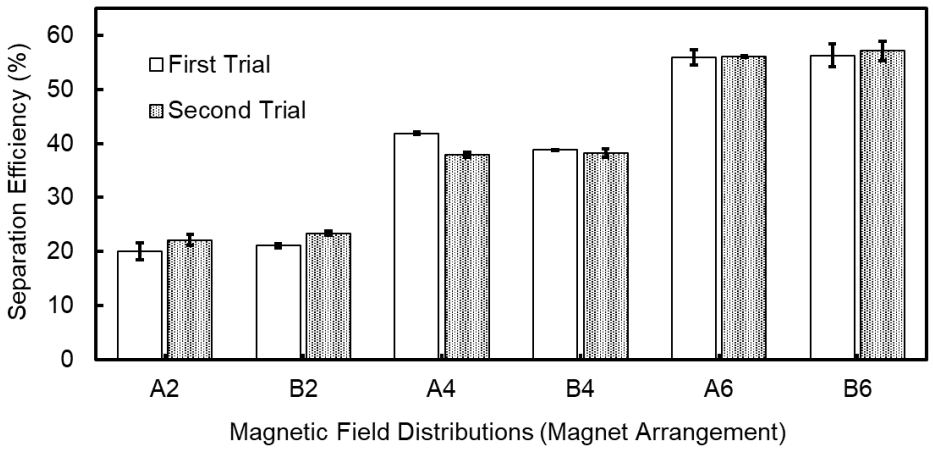

Figure 4.13: The separation efficiency with two trials experiments achieved in the CF-LGMS separator with different magnet arrangement.

The separation efficiency resulted from the simulation is tabulated in Figure 4.14 along with the average separation efficiency obtained from the experimental results. It is apparent that the simulation results show the consistent trend with the experimental results, in which the separation efficiency will be boosted as the number of magnets increases. For instance, magnet arrangements of A2 (26.5%) and B2 (24.5%) have the lower separation efficiency as compared to the setup by using four magnets (the separation efficiency imposed by magnet arrangements of A4 and B4 is given by 45.8% and 41.3%, respectively) and six magnets (the separation efficiency imposed by magnet arrangements of A6 and B6 is 60.0% and 57.6%, respectively).

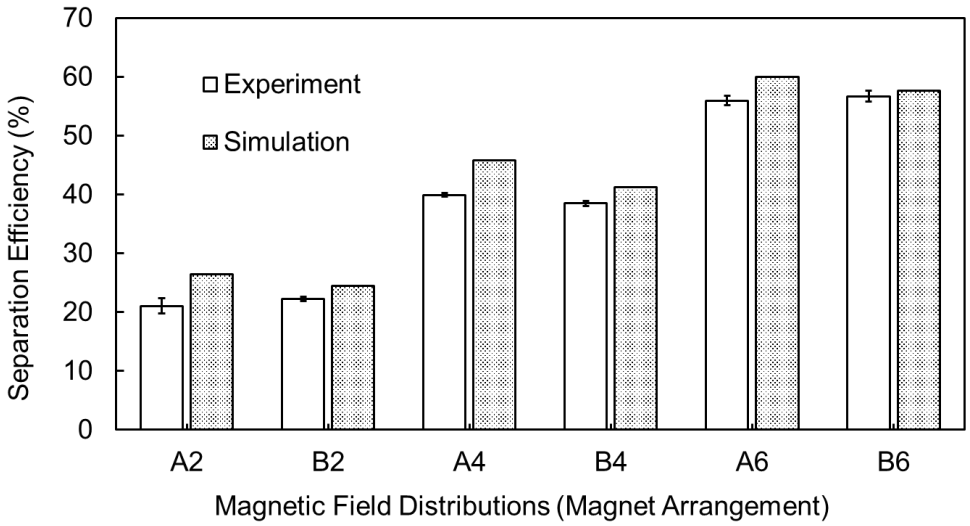

Figure 4.14: Comparison of the experimental and simulated separation efficiency achieved in the CF-LGMS separator with different magnet arrangement.

However, the separation efficiencies generated by the simulation are consistently higher than the experimental results. For instance, by using the B6 arrangement, the calculated separation efficiency is ~0.9% higher than the

experiment observation. For other cases illustrated in Figure 4.14, the separation efficiencies predicted by the simulation are ~2-5% higher than the experiments (except experiment conducted with magnet arrangement of A4 that is showing a deviation of 6%). There are two possible reasons for this over prediction scenario. The assumptions on the instantaneous aggregation of the MNPs and the MNPs are always in the aggregation state throughout the entire separator column in the modelling are not always valid, particularly at the region with very low magnetic field gradient (Heinrich et al., 2015), which causes the model to overpredict the magnetophoretic velocity as well as separation efficiency. Secondly, the greater separation efficiency shown in the calculation is due to the assumption of face-centered cubic packing (the most compact packing for arranging hard spheres with a packing factor of 0.74) in the arrangement of MNPs within a MNP cluster (see Appendix C for the detailed calculation). Nevertheless, in reality, the MNPs will not be perfectly arranged and the MNPs will be more loosely placed within the cluster because the MNP clusters are not being compressed physically during the functionalization process. So, the packing factor of the MNP clusters should be lower than 0.74 (the value assumed in the model calculation) in the actual scenario. In this regard, the magnetic mass of the MNP cluster can be lower, hence, the actual magnetic force acting on them is smaller than the model calculation which is leading to the consistently lower separation efficiency found in all CF-LGMS experiments. Such a discrepancy between the mathematical model and real case scenario causes the model simulation to predict the consistently higher separation efficiency.

In addition, it can also be generalized from Figure 4.14 that (i) the error of calculation increases as the number of magnets decreases, and (ii) the error of calculation is consistently greater for aligned magnet arrangement (with abbreviation initiated with ‘A’), as compared to misaligned magnet arrangement (with abbreviation initiated with ‘B’). When lower number of magnets are employed, the simulation result shows the greater error because there is higher proportion of separator column that is subjected to very low magnetic field, thus, the self-aggregation of MNPs did not occur or trivial in these regions during the real-time experiment. This has caused the greater extent of overprediction of the MNP self-aggregation effect, which gives rise to the larger error in the estimation of separation efficiency. Yet, the error diminishes when the number of magnets increases (see Figure 4.14), due to the higher volume ratio of the separator column is exposed to high magnetic field which closely resembles the real case scenario and is more aligned with the model assumption. This reason is also applicable in explaining the larger error is constantly being observed in the simulation of CF-LGMS process under the aligned magnet arrangement (abbreviation started with ‘A’ in Figure 4.14). In this context, the misaligned magnet arrangement brings about the higher coverage of intense magnetic field within the separator column (see Figure 4.7), which subsequently gives more spaces for self-aggregation to occur, and hence, the model assumption would be closer to the actual scenario.

In order to understand the contribution of migration pathway toward the separation kinetics, the fraction of MNPs being collected by each magnet is also shown in the Figure 4.15. It can be observed that the MNPs entering the separator (from the left) are being deflected towards the magnets, which

subsequently being captured and separated from the fluid domain. For instance, the magnet arrangement of B2 can only successfully separate a total of 24.5% of MNPs (14.2% and 10.3% on first and second magnets, respectively). However, when more magnets were used (magnet arrangements of B4 and B6), the subsequent magnets can further improve the separation efficiency by capturing more MNPs that have escaped from the preceding magnet(s) (Khashan and Furlani, 2014). In addition, as illustrated by the MNP motion path, the preceding magnet(s) is also playing the crucial role in steering the MNPs to move closer to the column wall (even though the magnet fail to capture them), which facilitates their capture by the subsequent magnet(s). For instance, under magnet arrangement of A6, the MNP entering the separation column at y = 1.0 cm has been deflected upwards with deflection angles of 36.84°, 49.52° and 70.61° after passing through the first, second and third pairs of magnets, respectively (defection angle is defined as the acute angle between the horizontal and vertical components of MNP velocity).

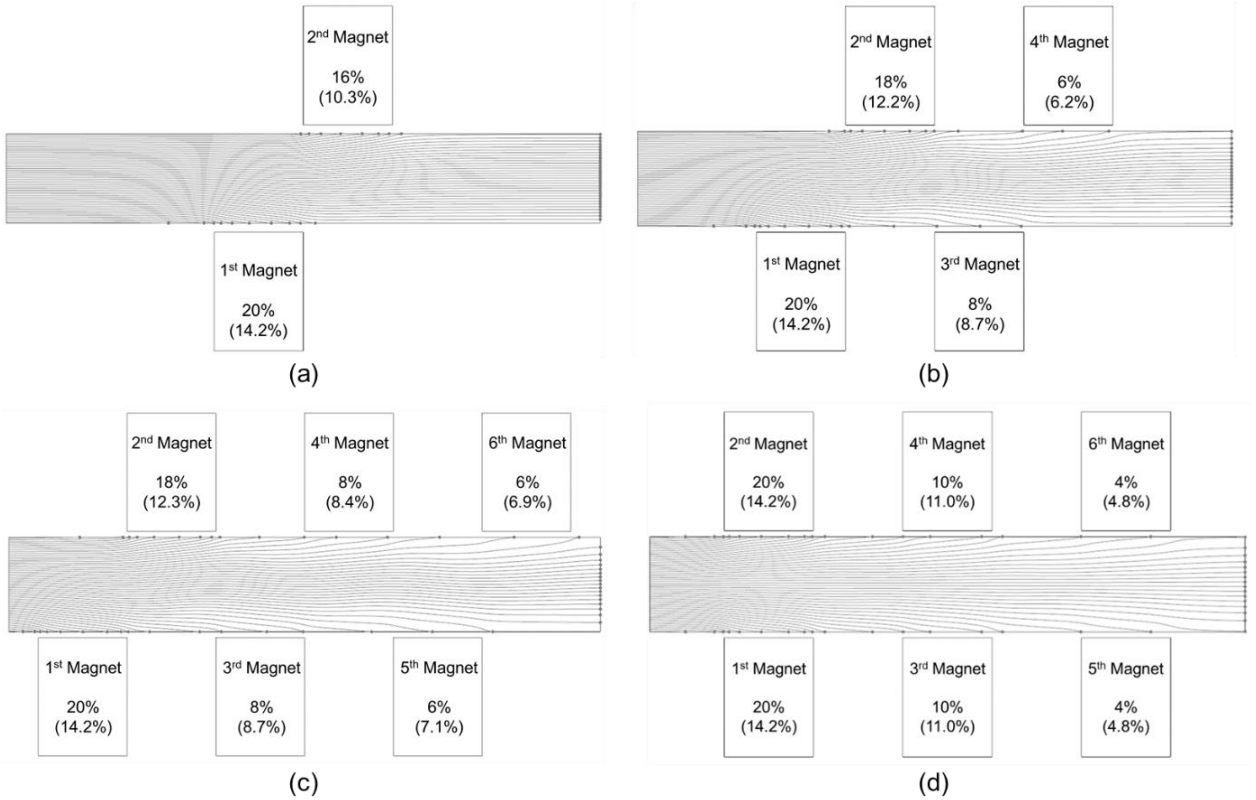

Figure 4.15: The MNP trajectory profile with different magnet arrangements (a) B2, (b) B4, (c) B6 and (d) A6 at fixed flowrate of 10 mL/min. Only 50 particles are demonstrated in the diagram. The reported numbers are the percentage of MNPs being captured by each respective magnet. The values inside the bracket are the corrected value after considering the 3-D geometrical.

Moreover, the percentage of MNPs being captured by the first magnet is always higher than the magnets that are further away from the column entrance (see Figure 4.15). By taking B4 magnet arrangement as example, the first and second magnets are able to capture more MNPs (14.2 and 12.2%) as compared to the subsequent magnets (8.7 and 6.2%), as shown in Figure 4.15 (b). Since the concentration of MNP solution is higher when the solution is being charged into the column (with higher number of MNPs per unit volume), thus, more MNPs can be captured by the first magnet. These findings suggest that increase the number of magnets can improve the separation efficiency of the CF-LGMS process, however, the degree of improvement will deteriorate as the number of magnets is getting higher to the point of diminishing return. Furthermore, due to these deflected particle trajectories the capture locality also decreases in favor of the downstream magnet(s) and should be more profoundly on the last magnet (Khashan and Furlani, 2014). By taking the CF-LGMS process induced by magnet arrangement A6 as example (Figure 4.15 (d)), the first pair of magnets can capture a total of 28.4% of MNPs, while the separation efficiency declines to 22% and 9.6% for second and third pairs of magnets, respectively, that are located at the downstream of the column.

In addition, for the misaligned magnet arrangement cases, it can be noticed that the magnets located at both sides of the separator column possess different MNP capture efficiency, in the manner that the magnet(s) located closer to the entrance is capable to capture more MNPs. By taking B6 magnet arrangement in Figure 4.15 (c) for an example, even though both the 1st and 2nd magnets are the first pair of magnets encountered by MNPs at the upper and lower half of the separator column, the percentage of MNPs being captured by

1st and 2nd magnets is given by 14.2% and 12.3%, respectively. Since the MNPs at the upper half of the separator column are also being pulled downward by the magnetic force imposed by the 1st magnet as the solution is moving through, this portion of MNPs will gain the downward velocity. As these MNPs are passing through the region where the 2nd magnet at the top, the upward deflection and capture of MNPs is more difficult due to their initially downward motion, thus causes the capture efficiency imposed by the 2nd magnet to be relatively lower. However, this phenomenon is not observed in the A6 magnet arrangement that is horizontally symmetry, as shown in Figure 4.15 (d).

4.6.2 Effect of Concentration

In this section, the effect of MNP concentration on the separation efficiency (with two trials experiments) of CF-LGMS is examined (experiment sets 6 to 10 of Table 3.3), in which the results are tabulated in Figure 4.16. According to this figure, it is apparent that the separation efficiency is increasing with the initial concentration of MNP solution that is being fed to the CF-LGMS process. For instance, when the initial concentration of MNP solution was increased from 20 mg/L to 100 mg/L, the separation efficiency of CF-LGMS experiment was improved from 39.69% to 57.59% (represent by average value). Under higher MNP concentration, the number of MNPs inside the solution is higher, with reducing inter-particle spacing. Therefore, the inter-particle interaction between MNPs (cooperative effect) can be more intense

and causes the formation of larger MNP aggregates (Chong et al., 2021). As the larger MNP aggregates are having higher magnetophoretic velocity, the efficiency of CF-LGMS process can be further improved under high particle concentration. In fact, this trend is consistent with the LGMS processes that are conducted in BW manner (Leong, Ahmad and Lim, 2015).

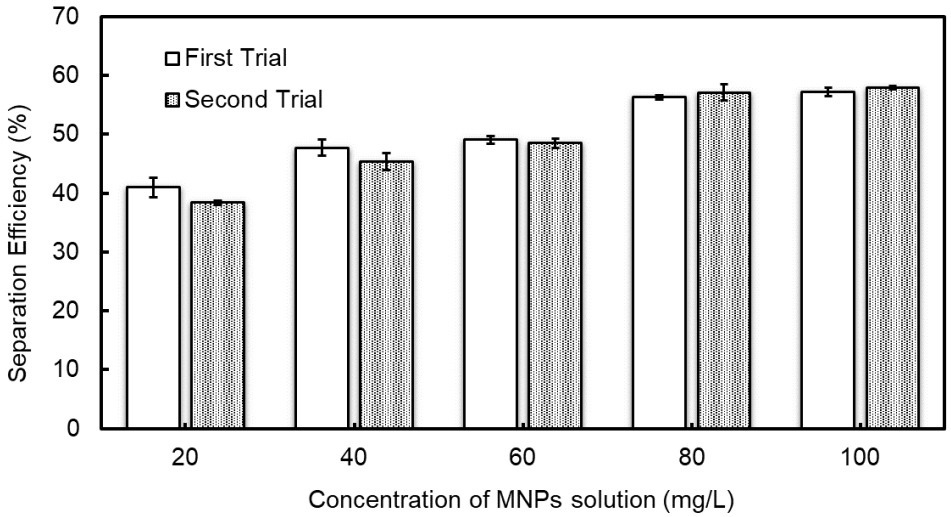

Figure 4.16: The separation efficiency with two trials experiments achieved in the CF-LGMS separator by using different initial concentration of MNP solution.

The simulation results predict an upward trend in separation efficiency as particle concentration increased (see Figure 4.17). According to the calculation, the higher MNP concentration leads to an increase in the mass and size of the MNP aggregate (*N* value in Equation (4.7)) (Chong et al., 2021), thereby causes MNPs to move toward the separator wall with the greater magnetophoretic velocity and being separated out from the solution more effectively. The separation efficiency of MNP solutions with initial concentration of 20 mg/L, 40 mg/L, 60 mg/L, 80 mg/L and 100 mg/L are 43.6%, 49.3%, 51.6%, 57.6% and 60.0%, respectively. Such trend is more

likely caused by two factors: (i) there are more magnetic mass per volume, and (ii) there are higher chance for particle interaction along its magnetophoretic migration pathway leading to more effectively separation. In fact, this phenomenon in which concentration dependency of MNPs deflection by magnetic field is much more substantial in microfluidic devices and serves as the basis of particle/cell sorting technology (Zhang et al., 2009). Nevertheless, there is a small discrepancy between experimental and simulation results in the range of 0.9 – 3.9% with the possible reasons described in the previous subsection.

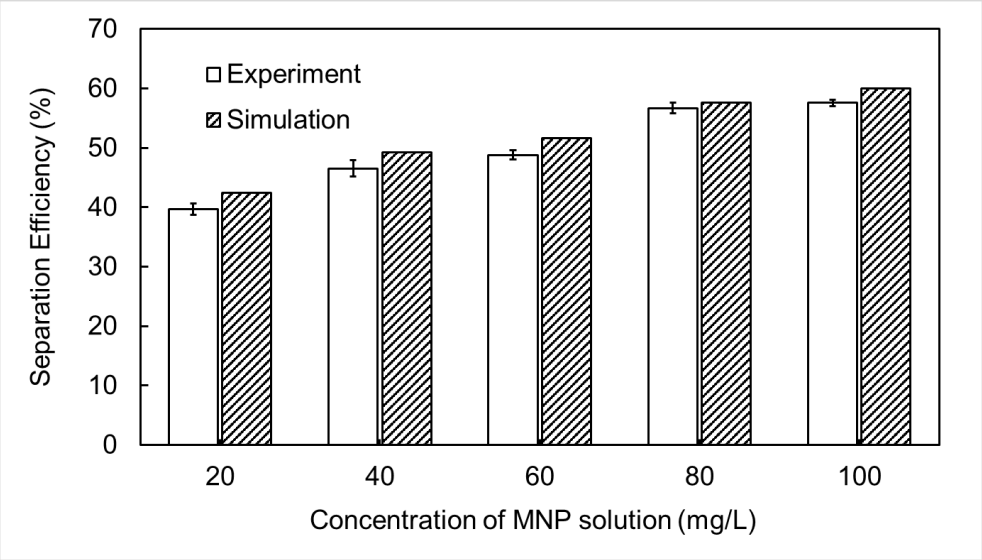

Figure 4.17: Comparison of the experimental and simulated separation efficiency achieved in the CF-LGMS separator by using different initial concentration of MNP solution.

Furthermore, the MNP trajectory profiles and the respective MNP capture percentage by each magnet under different concentrations (20 mg/L and 100 mg/L), are also tabulated in Figure 4.18. It is apparent that the MNPs can be deflected at the greater extent and more particles can be successfully captured by the magnets when higher initial concentration (100 mg/L) was

used. For instance, under B6 magnet arrangement, the capture efficiency of 1st and 2nd magnet is given by 16.3% and 14.2%, respectively when initial concentration of MNP solution at 100 mg/L is used (Figure 4.18). However, the capture efficiency has been decreased to 8.5% for both magnets when the initial MNP concentration is reduced to 20 mg/L, under the same magnet arrangement (Figure 4.18). Since the fluid flow is constant throughout all these experiments, the extent of particle trajectory deflection is mainly influenced by the magnetophoretic velocity of the MNP (Pamme and Wilhelm, 2006). As discussed previously, higher concentration is more favorable for cooperative magnetophoresis (Faraudo, Andreu and Camacho, 2013), and so, the capture efficiency of the subsequent magnet is also concentration dependent.

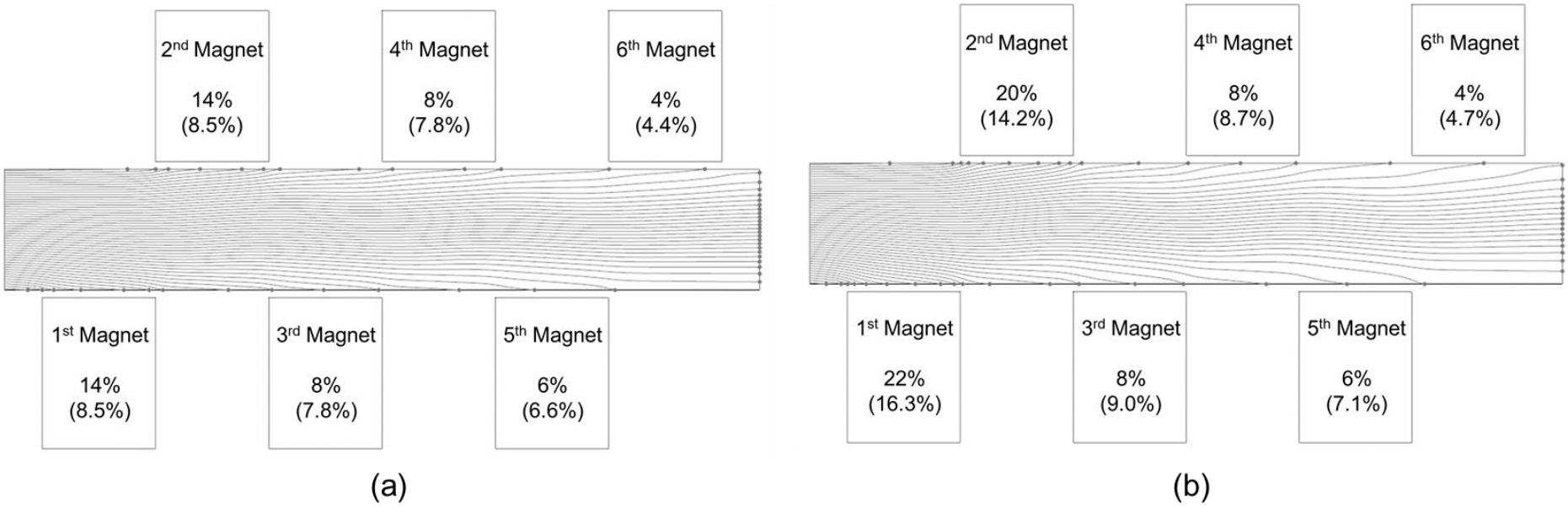

Figure 4.18: The MNP trajectory profile with various initial MNP concentration (a) 100 mg/L, (b) 20 mg/L at fixed flowrate 10 mL/min. Only 50 particles are demonstrated in the diagram. The reported numbers are the percentage of MNPs being captured by each respective magnet. The values inside the bracket are the corrected value after considering the 3-D geometrical effect.

4.6.3 Effect of Flowrate

The separation efficiency (with two trials experiments) of CF-LGMS subjected to different flowrate of MNP solution is tabulated in Figure 4.19. According to this figure, it can be noticed that the separation efficiency is as high as 78.90% at the lowest flowrate. Meanwhile, when the flowrate is further increased to 10, 15 and 20 mL/min, the separation efficiency is declined dramatically to 56.70%, 43.57% and 32.82% (represent by average value), respectively. The higher the flowrate of MNP solution, the shorter its residence time and lesser time for MNPs to be exposed to the magnets (or remaining within the capture zone of the magnet) which subsequently causes more MNPs to be flushed out of the column without being separated. On the other hand, if the flow rate is decreased, the duration for MNPs to migrate towards the magnets will be longer, thus, more MNPs can be captured on the separator wall and isolated from the solution.

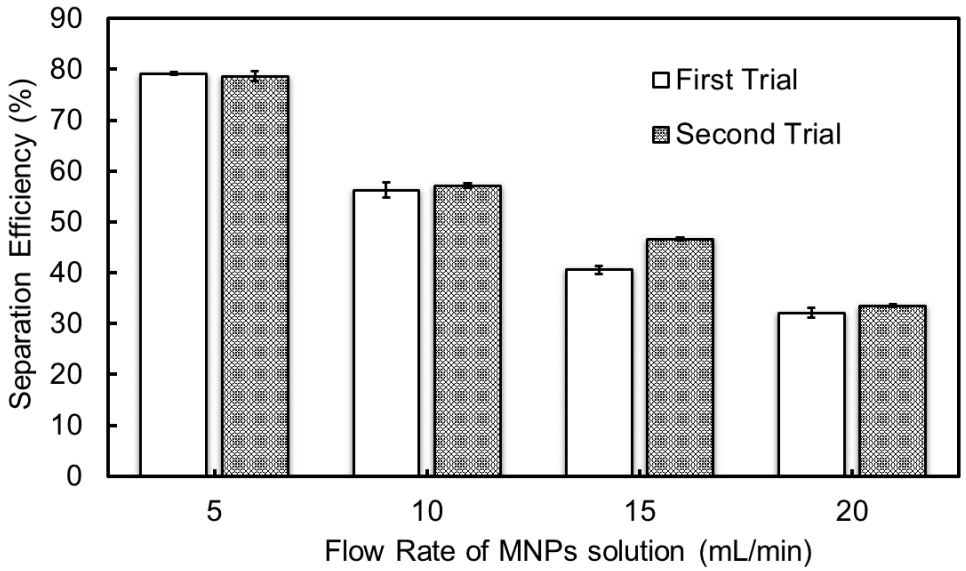

Figure 4.19: The separation efficiency with two trials experiments achieved in the CF-LGMS separator at different MNP flowrate.

In addition, at high flow rate, the hydrodynamic contribution of the convective current greatly out weight the magnetophoretically induced flow and greatly reduced the particle deflection (Pamme and Manz, 2004). By taking a 6 mm flow chamber as an example, a small increment of convective flow velocity from 0.4 mm/sec to 2.0 mm/sec has completely suppressed the contribution of magnetophoretic separation (Pamme and Wilhelm, 2006). Such phenomenon is less pronounced here, since at the highest flow rate in this experiment at 20 mL/min (corresponds to 1.70 mm/sec, which is approaching the maximum flow velocity in the work reported by Pamme and Wilhelm), a separation efficiency of 32.82% was still being observed (Pamme and Wilhelm, 2006). Hence, the arrangement of magnetic array for separation is critical and could lead to more localized magnetic field gradient for capture purpose. For instance, the magnetic field gradient as high as ~100 T/m can be observed in the vicinity of the magnets, by employing the magnet arrangement in this study (Figure 4.7). On the other hand, the magnetic field gradient generated in the work reported by Pamme and Wilhelm is much lower at ~45 T/m, which causes the magnetophoretic separation of MNPs under high flowrate to be significantly suppressed (Pamme and Wilhelm, 2006).

Also, the simulation (shown in Figure 4.20) is in good agreement with the experimental results in term of the relationship between the flowrate and separation efficiency, in which the separation efficiency of the CF-LGMS process is higher if lower flowrate is employed. For instance, the predicted separation efficiency of MNPs under flowrate of 5 mL/min can be as high as 77.2%, however, it decreases to 57.6%, 43.6% and 34.8% when the flowrate is increased to 10 mL/min, 15 mL/min and 20 mL/min, respectively. Similarly to

the results reported in the previous subsections, the separation efficiency predicted by the simulation is consistently higher than the experimental results (except for low flowrate of 5 mL/min). Separation efficiency was under-predicted by the simulation as compared to the experimental results (~2% lower) at low flowrate of 5 mL/min. This phenomenon is probably attributed to the formation of the larger MNP aggregates than theoretical prediction when the MNP residence time is sufficiently long in the separator. Owing to this reason, the separation efficiency of the real time CF-LGMS process under low flowrate is higher than the result predicted by the model simulation. Regardless of that, the model prediction of separation efficiency is still accurate with only error of ~2%. Such findings suggest that the cooperative magnetophoresis is quite substantial on influencing the magnetic separation, even under forced convection, as compared to hydrodynamic flow generated by MNP motion.

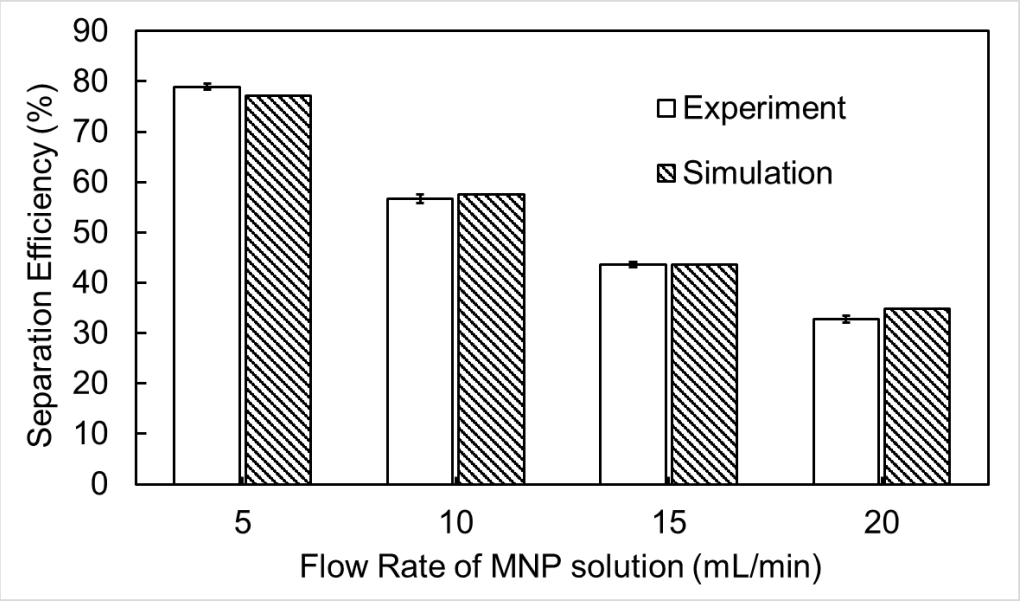

Figure 4.20: Comparison of the experimental and simulated separation efficiency achieved in the CF-LGMS separator at different MNP flowrate.

The MNP trajectory profiles and percentage of particle capture by each magnet under different flowrate is also tabulated in Figure 4.21. It is apparent that more particles are being captured onto the wall by the magnet at lower flowrate (5 mL/min) as compared to higher flowrate (20 mL/min). For instance, under magnet arrangement B6, the CF-LGMS process operated at lower flowrate (5 mL/min) exhibits higher capture efficiency (27.6% and 22.9% of MNPs being captured on the 1^{st} and 2^{nd} magnets, respectively) as compared to 20 mL/min (6.8% of MNP being captured on both 1^{st} and 2^{nd} magnets). However, for the magnets that are located closer to the column exit (at the more downstream position), the capture efficiency is relatively smaller for the case with low MNP solution flowrate as compared to the higher flowrate. For instance, there are 5.0% and 2.4% of MNPs being captured on 5^{th} and 6^{th} magnets, respectively when lower flowrate of 5 mL/min is adopted. Yet, at high flowrate of 20 mL/min, the percentage of MNP being captured by 5^{th} and 6^{th} magnet is relatively higher at 6.3% and 4.1%, respectively. Under the lower flowrate (5 mL/min), the MNPs moved slowly with the fluid so that it have the longer time to be deflected toward the magnets located nearer to the entrance or upstream location (the magnetic force on the MNPs became too large with respect to the hydrodynamic flow by fluid), causing the concentration of MNP to be lower after the solution flowing through these magnets. Therefore, there are lesser particles available when the solution is passing through the magnets located at the downstream (nearer to the exit), which renders the percentage of MNPs to be captured by those magnets to be lower. On the other hand, under the higher flowrate (20 mL/min), there are higher proportion of MNPs escape from the magnets located at the upstream due to the magnetic force is not

enough to complete deflection of the MNPs toward the magnets (the magnetic force on the particle was outweighed by the hydrodynamic flow). Therefore, the MNPs that have accomplished half of their deflection will be fully deflected towards the magnets located nearer to the exit and the concentration of MNPs is higher at the downstream, which causes more MNPs being captured by magnets. Such finding suggests that the increment in the number of magnets imposes more significant improvement on the CF-LGMS processes that are operated under the higher flowrate.

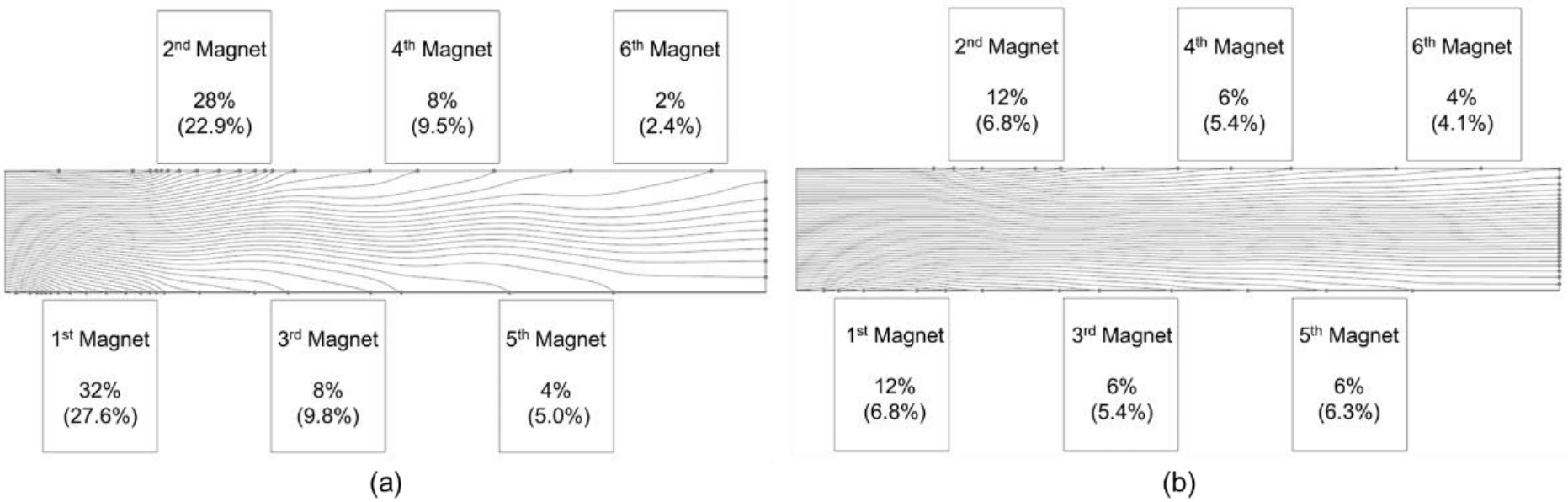

Figure 4.21: The MNP trajectory profile with different flowrate of MNP solution (a) 5 mL/min, (b) 20 mL/min at fixed initial concentration 80 mg/L. Only 50 particles are demonstrated in the diagram. The reported numbers are the percentage of MNPs being captured by each respective magnet. The values inside the bracket are the corrected value after considering the 3-D geometrical effect.

According to the comparison between the separation efficiencies predicted by the simulation and experimental measurement (for all experimental sets tabulated in Figures 4.14, 4.17, 4.20), it can be concluded that the CF-LGMS model established in this study is able to predict the real time scenario up to excellent accuracy (with average percentage error ~2.6%). Thus, the mathematical model developed in this study can be used to estimate the separation efficiency of CF-LGMS process during design and optimization phases of the separator for engineering applications.

4.7 Feasibility Study of CF-LGMS in Achieving High Separation Efficiency

Lastly, to further verify the feasibility of implementing the CF-LGMS process in real time application to achieve high separation efficiency, the multistage CF-LGMS processes were conducted experimentally. In this context, the MNP solution effluent from the first separator column is directed to the subsequent cycle of CF-LGMS process for two times, which resembled the MNP solution undergoing three stages of CF-LGMS columns connected in series. Here, only two sets of experiments conducted which involve the usage of magnet arrangements B6 and B4. In these experiments, the concentration of the MNP solution flowing into the CF-LGMS column for magnet arrangements of B6 and B4 is 100 mg/L and 80 mg/L, respectively while the flowrate is fixed at 10 mL/min.

The separation efficiency after each stage of CF-LGMS column is demonstrated in Figure 4.22. According to the figure, it can be noticed that the

separation efficiency can be further enhanced after undergoing every stage of CF-LGMS separation. For instance, the separation efficiency was boosted to almost 90% after three stages of CF-LGMS separation when magnet arrangement B6 was used (Figure 4.22 (a)). In addition, even for the three-stages CF-LGMS experiment conducted with magnet arrangement B4, separation efficiency of MNP solution after the third column also significantly higher (75.31%) as compared to those effluent obtained from the first (40.76%) and second (63.14%) stages (Figure 4.22 (b)). Such observation indicates that increasing the number of stages of CF-LGMS separation can enhance the separation efficiency which enables this separation scheme to be feasible in the real time engineering application (the separation efficiency can up to ~90% as shown by the experimental results in Figure 4.22 (a)).

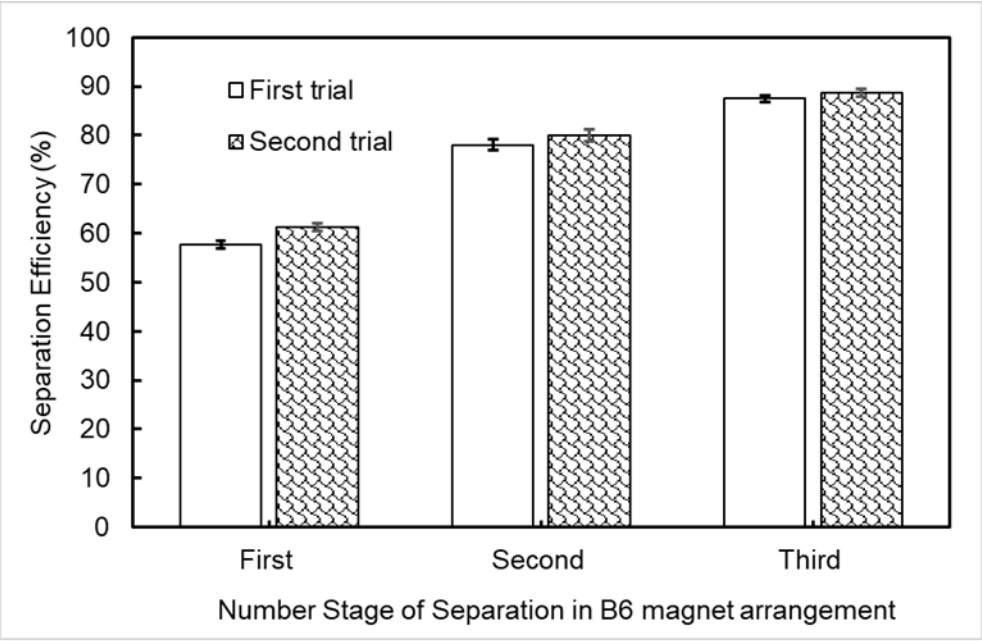

(a)

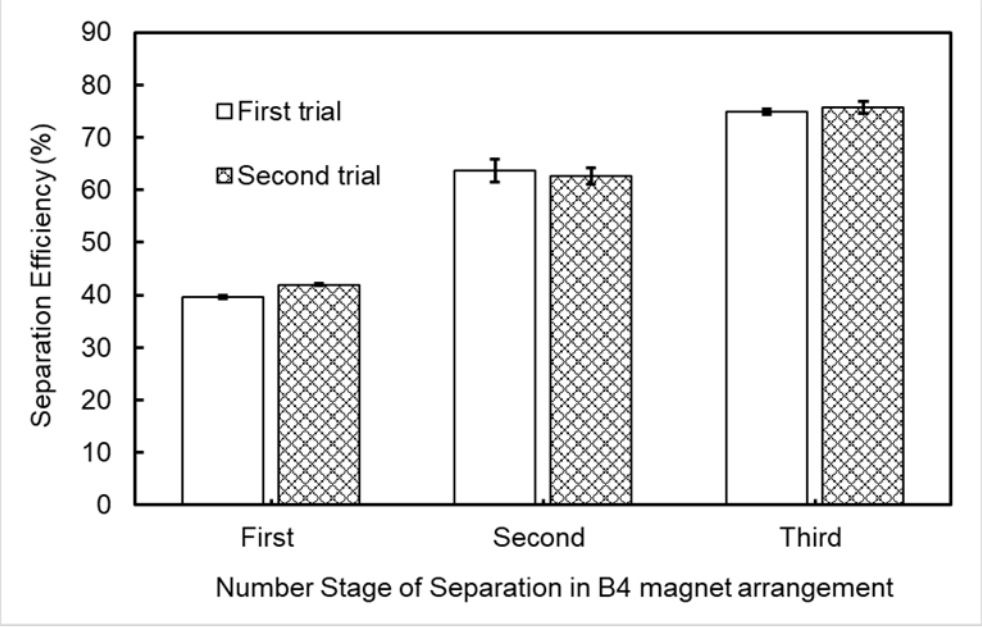

(b)

Figure 4.22: The separation efficiency with two trials experiments achieved in three-stages of CF-LGMS process by using (a) magnet arrangement of B6 and MNP concentration of 100 mg/L and (b) magnet arrangement of B4 and MNP concentration of 80 mg/L.

In addition, such a multi-stages CF-LGMS process also being simulated by using the model developed in Section 4.5. The separation efficiency of the

three-stages CF-LGMS process resulted from the model simulation is tabulated in the Figure 4.23. In addition, the average separation efficiency measured from the experiment is also included in this figure for comparison purpose. It is apparent that the simulation results show the consistent trend with the experimental results, in which the separation efficiency will be boosted by increasing the number of stages of CF-LGMS separation. For instance, under magnet arrangement B6, the separation efficiency after three stages of CF-LGMS separation (88.55%) is remarkably higher than those demonstrated by MNP solution coming out from the first (60%) and second (79.72%) stages of separation (Figure 4.23 (a)). Nevertheless, there is a small discrepancy between experimental and simulation results in the range of 0.4 – 0.7 %, which indicates that the model developed in Section 4.5 also can predict the separation efficiency of multi-stages CF-LGMS process up to very high accuracy. The possible reasons for the minor error from the model prediction have been described in Section 4.6.1.

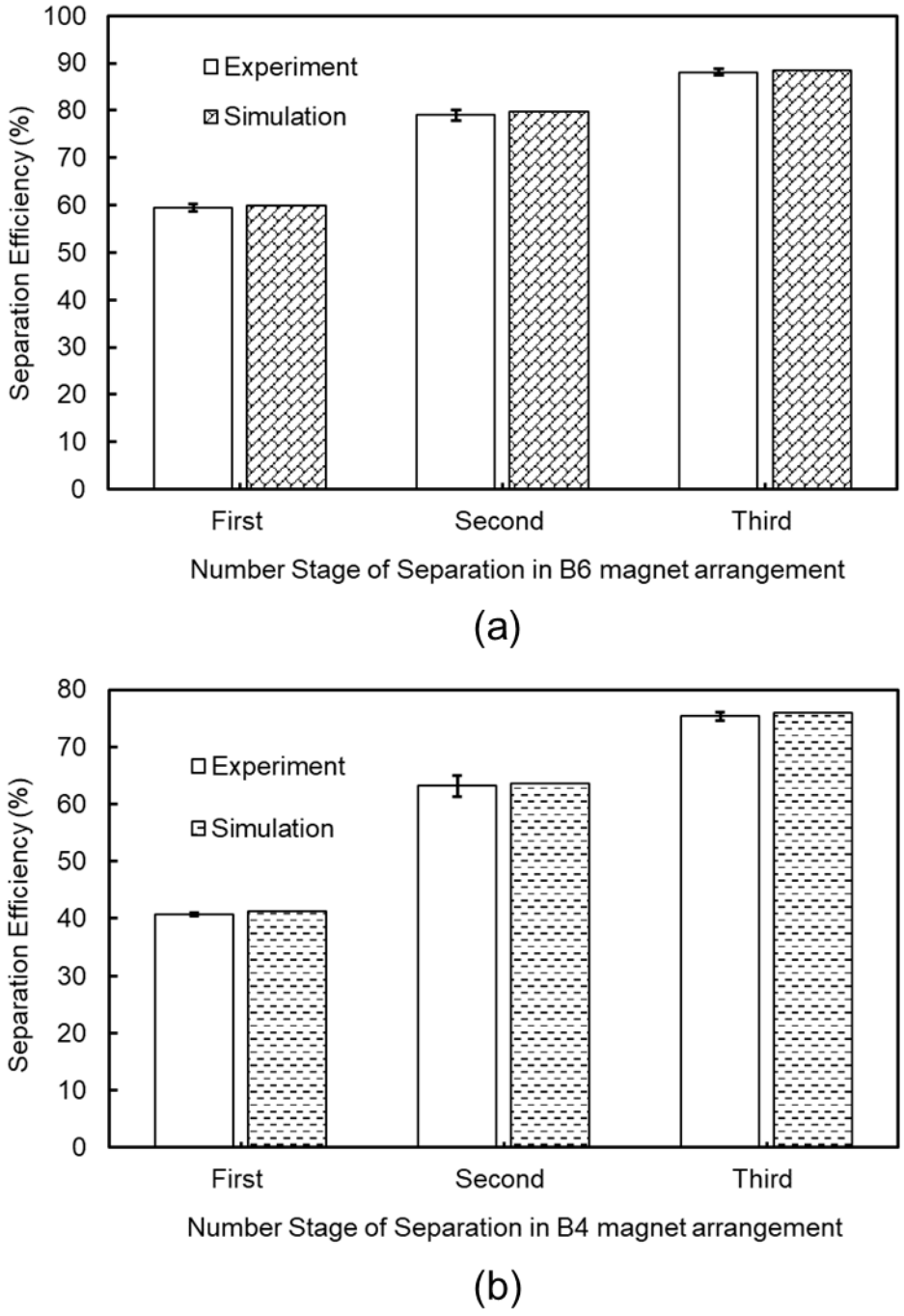

Figure 4.23: Comparison of the experimental and simulated separation efficiency of the three-stages of CF-LGMS process in (a) magnet arrangement of B6 and MNP concentration of 100 mg/L and (b) magnet arrangement of B4 and MNP concentration of 80 mg/L.

Furthermore, the separation efficiency of individual stages as well as the overall process for the multi-stages CF-LGMS is demonstrated in Figure

4.24, for both results obtained from experiment and model simulation. According to this figure, both experimental and simulation results are consistent among each other, with only minor discrepancy between both results. Moreover, it can be observed that the individual separation efficiency declines in the separator column that is located at the more downstream location. For instance, under magnet arrangement B6, the individual separation efficiency for the third separation column (43.12%) appears to be lower as compared to the first separation column (59.44%) (Figure 4.24 (a)). This is because after flowing through the upstream separation stages, there are some MNPs being captured on the magnet and isolated from the MNP solution, which leads to the decrease in the initial concentration of MNP solution to be charged to the next separation stage. Owing to the decrease of MNP concentration, the intensity of the cooperative effect declines at the CF-LGMS column(s) located at the downstream which subsequently leads to the poorer performance of the given separation stage(s).

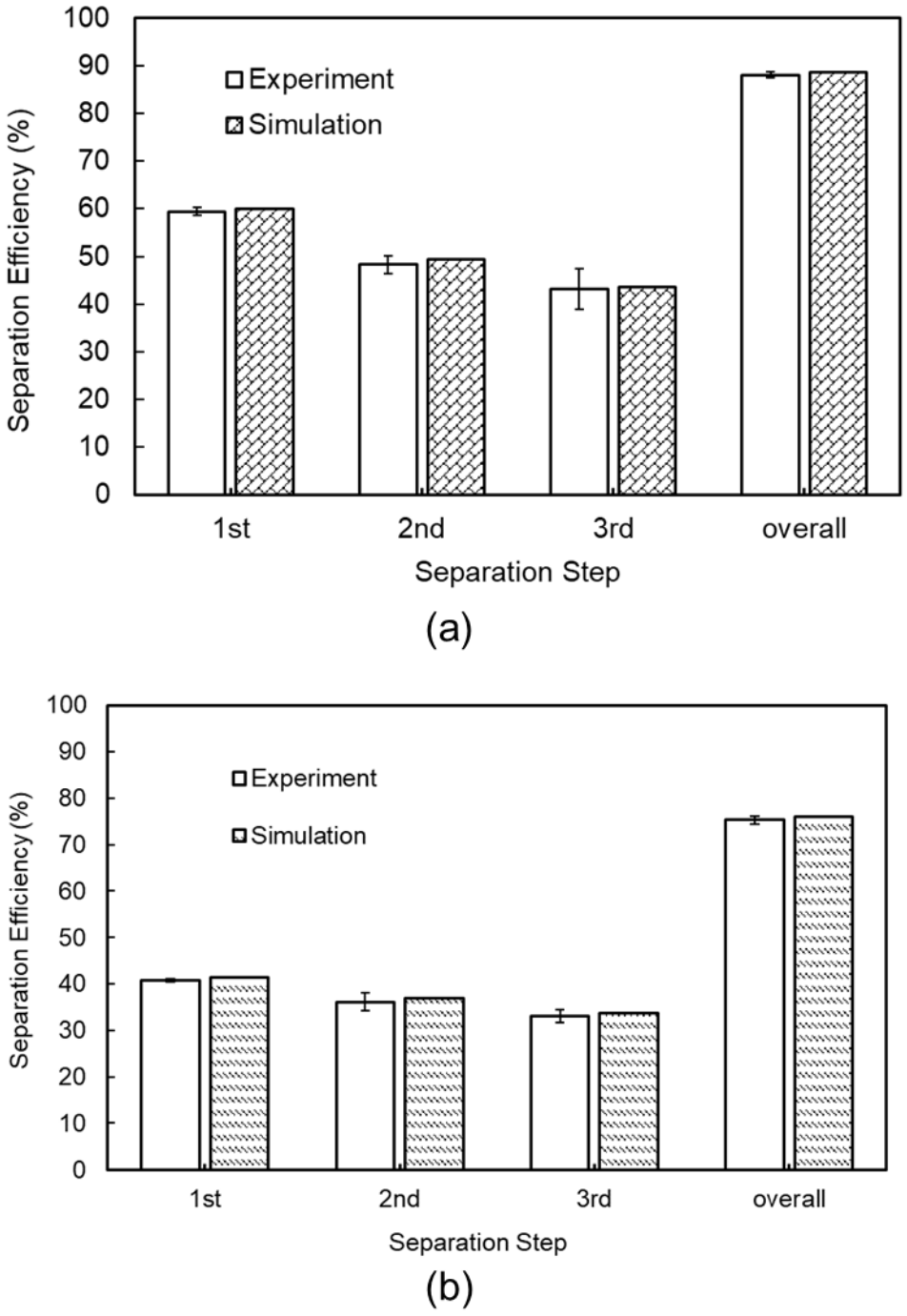

Figure 4.24: Comparison of the experimental and simulated separation efficiency at individual stages as well as the overall process for the multi-stages CF-LGMS in (a) magnet arrangement of B6 and MNP concentration of 100 mg/L and (b) magnet arrangement of B4 and MNP concentration of 80 mg/L.

CHAPTER FIVE

CONCLUSIONS AND RECOMMENDATIONS

This chapter summarizes all the outcomes acquired in this study. Additionally, some possible recommendations for potential improvements of this study are proposed at the end of this chapter.

5.1 Conclusion

In this study, the characterization of unmodified magnetic nanoparticles (MNPs) as well as PSS-functionalized-MNPs used in this study was done by using (i) scanning electron microscopy (SEM), (ii) dynamic light scattering (DLS) and (iii) vibrating sample magnetometer (VSM). According to the SEM results, the MNPs are almost spherical in shape with average diameter of 44.1 ± 5.3 nm. Furthermore, based on the DLS measurement, the average hydrodynamic diameter of unmodified MNP and PSS-functionalized-MNPs are ~1123 nm and ~245.3 nm, respectively. Moreover, the magnetization curve for unmodified MNP and PSS-functionalized-MNPs obtained from the VSM analysis shows the MNP system is almost superparamagnetic with negligible hysteresis loop. The saturation magnetization of unmodified MNP and PSS-functionalized-MNPs was measured as 70.41 emu/g and 69.48 emu/g, respectively.

Later on, the lab-scale experiments on the low gradient magnetic separation (LGMS) of the PSS-functionalized-MNP under batchwise low gradient magnetic separation (BW-LGMS) (induced by different magnet arrangements) were first performed to observe the transient behavior of MNP distribution. Next, a mathematical model based on BW-LGMS process was developed by using classical magnetophoresis theory with the incorporation of particle aggregation effect (without the consideration of hydrodynamic effect, i.e., the fluid is assumed to be always at the stagnant condition). Comparison between mathematical model and experiment has revealed that the simulation results of BW-LGMS model is closer to the experimental observation when higher number of magnets was employed, which implies that the inertial motion of MNPs is dominating the induced convection (by hydrodynamic effect) at the regions with more intense magnetic field. In addition, it also can be concluded that the forced convective flow of continuous flow low gradient magnetic separation (CF-LGMS) is more significant than the magnetophoresis induced convection (which is ~4 times higher in term of magnitude of velocity), even under the lowest MNP solution flowrate of 5 mL/min. In this regard, only cooperative effect (self-aggregation of MNP clusters) is considered, and hydrodynamic effect (magnetophoresis-induced convection) is ignored to formulate the model to describe CF-LGMS process, in which the results from simulation are showing the same trend with the experimental results.

Then, the LGMS experiments were further extended to continuous flow (CF) manner to study the effect of several design parameters (MNP concentration, MNP solution flowrate and arrangement of magnet) on the separation efficiency. Furthermore, a mathematical model on CF-LGMS

processes was developed by modifying from the BW-LGMS model to describe the transport behavior of MNP during CF-LGMS process and predict the separation efficiency. Both experiment and simulation results of LGMS processes confirmed that the separation efficiency increases when the number of magnets increases (separation efficiency η = 22.22% and 56.70% when two and six magnets are used, respectively) as the higher proportion of the CF-LGMS separator is within the influence of relatively strong magnetic field. On the other hand, by comparing the same number of magnets, misaligned magnet arrangement demonstrated slightly greater separation efficiency (56.70% for magnet arrangement of B6) than aligned arrangement (55.98% for magnet arrangement of A6). Such finding is resulted from the high coverage of strong magnetic field within the separator column when the number of magnets is higher and misaligned magnet orientation is used. In addition, the separation efficiency of CF-LGMS process also can be enhanced when MNP solution with higher concentration is used (57.59% under concentration of 100 mg/L while 39.69% for concentration of 20 mg/L). This is because the cooperative effect is more pronounced under higher MNP concentration, which allows the formation of larger MNP aggregates that are subjected to the higher magnetophoretic velocity and can be separated in a shorter duration. Lastly, it was revealed that the separation efficiency is the highest (78.90%) when the CF-LGMS process is operated under the lowest flow rate (5 mL/min), and it started to decline when the flow rate increases from 10 mL/min to 20 mL/min. The higher the flowrate, the shorter the residence time of MNP solution within the separator column to perform the separation, which causes more MNPs to be flushed out of the column without being separated. On the other hand, if the

flow rate is decreased, the duration for MNPs to migrate towards the magnets will be longer, thus, more MNPs can be captured on the separator wall and separated from the solution.

Even through the experimental and simulation results shows the consistent trend in term of the separation efficiency of the CF-LGMS process, the separation efficiency predicted by the model simulation is consistently higher by 0.9-5.9% (except for the experiment conducted with the lowest flow rate at 5 mL/min). Such phenomenon is due to the overprediction of MNP aggregation activity at the region with very low magnetic field in the mathematical model developed in this study. Regardless of that, the model is able to predict the separation efficiency of CF-LGMS experiments conducted in this study up to excellent accuracy, with average error of ~2.6% for 13 sets of experiments.

Last but not least, to further verify the feasibility of implementing the CF-LGMS process in the real time application, the CF-LGMS process is conducted in multistage manner, which resembles the MNP solution that is flowing through a few separation columns at are connected in series. According to the experiment and simulation results, it can be found that the separation efficiency has been boosted to almost 90% after three stages of CF-LGMS separation when magnet arrangement B6 and MNP solution with concentration of 100 mg/L was used. This observation has proven the feasibility of the CF-LGMS technique in removing the MNPs up to huge extent.

5.2 Recommendation

1. Hydrodynamic effect can be incorporated in the BW-LGMS model to improve the accuracy of the simulation result as the magnetophoresis induced convection is noticeable and quite significant in the BW-LGMS process, particularly at the far-end region with very low magnetic field gradient.
2. Dynamic particle agglomeration/aggregation process should be taken into consideration in the CF-LGMS modelling process to further improve the predictability of the model as instantaneous aggregation assumption might not be valid under all circumstances of CF-LGMS process. In fact, the magnetophoresis induced convection and forced convection could affect the dynamical behavior of aggregate formation under the CF-LGMS process.
3. The variation of the horizontal component of the MNP velocity should be physically simulated rather than assuming that it is constant, in the simulation of CF-LGMS process. This is due to the presence of frictional forces within the fluid, which oppose MNPs original motion and affect the horizontal component of the MNP velocity.
4. From industrial point of view, aligned magnet arrangement is strongly encouraged to be used in the CF-LGMS process in any real time application, as the setup of aligned arrangement is easier than misaligned arrangement which can reduce the manufacturing costs. This is because misaligned magnet arrangement might need some additional supports to hold the magnets while the magnets in aligned arrangement are in the stable state.

REFERENCES

Agiotis, L., Theodorakos, I., Samothrakitis, S., Papazoglou, S., Zergioti, I. and Raptis, Y.S., 2016. Magnetic manipulation of superparamagnetic nanoparticles in a microfluidic system for drug delivery applications. *Journal of Magnetism and Magnetic Materials*, [online] 401, pp.956–964. https://doi.org/10.1016/j.jmmm.2015.10.111.

Ahmed, Y. and Abdel, A., 2016. Superparamagnetic Nanoparticles for Cancer Theranostics the challenges and the hope. *Advances in Materials Science and Engineering*, [online] 2(1), pp.1–22. https://doi.org/10.13140/RG.2.2.12754.35522.

Ali, A., Shah, T., Ullah, R., Zhou, P., Guo, M., Ovais, M., Tan, Z. and Rui, Y., 2021. Review on Recent Progress in Magnetic Nanoparticles: Synthesis, Characterization, and Diverse Applications. *Frontiers in Chemistry*, [online] 9, p.629054. https://doi.org/10.3389/fchem.2021.629054.

Aliabadi, M., Shagholani, H. and Yunessnia lehi, A., 2017. Synthesis of a novel biocompatible nanocomposite of graphene oxide and magnetic nanoparticles for drug delivery. *International Journal of Biological Macromolecules*, [online] 98, pp.287–291. https://doi.org/10.1016/j.ijbiomac.2017.02.012.

Andreu, J.S., Barbero, P., Camacho, J. and Faraudo, J., 2012a. Simulation of Magnetophoretic Separation Processes in Dispersions of Superparamagnetic Nanoparticles in the Noncooperative Regime. *Journal of Nanomaterials*, [online] 2012, pp.1–10. https://doi.org/10.1155/2012/678581.

Andreu, J.S., Calero, C., Camacho, J. and Faraudo, J., 2012b. On-the-fly coarse-graining methodology for the simulation of chain formation of superparamagnetic colloids in strong magnetic fields. *Physical Review E*, [online] 85(3), p.036709. https://doi.org/10.1103/PhysRevE.85.036709.

Andreu, J.S., Camacho, J. and Faraudo, J., 2011. Aggregation of superparamagnetic colloids in magnetic fields: The quest for the equilibrium state. *Soft Matter*, [online] 7(6), pp.2336–2339. https://doi.org/10.1039/c0sm01424a.

Andreu, J.S., Camacho, J., Faraudo, J., Benelmekki, M., Rebollo, C. and Martínez, Ll.M., 2011. Simple analytical model for the magnetophoretic separation of superparamagnetic dispersions in a uniform magnetic gradient. *Physical Review E*, [online] 84(2), p.021402. https://doi.org/10.1103/PhysRevE.84.021402.

Babaei, A.A., Kakavandi, B., Rafiee, M., Kalantarhormizi, F., Purkaram, I., Ahmadi, E. and Esmaeili, S., 2017. Comparative treatment of textile wastewater by adsorption, Fenton, UV-Fenton and US-Fenton using magnetic nanoparticles-functionalized carbon (MNPs@C). *Journal of Industrial and Engineering Chemistry*, [online] 56, pp.163–174. https://doi.org/10.1016/j.jiec.2017.07.009.

Babincova, M., Altanerova, V., Altaner, C., Bergemann, C. and Babinec, P., 2008. <emphasis emphasistype="italic">In Vitro</emphasis> Analysis of Cisplatin Functionalized Magnetic Nanoparticles in Combined Cancer Chemotherapy and Electromagnetic Hyperthermia. *IEEE Transactions on NanoBioscience*, [online] 7(1), pp.15–19. https://doi.org/10.1109/TNB.2008.2000145.

Badruddoza, A.Z.M., Bhattarai, B. and Suri, R.P.S., 2017. Environmentally Friendly β-Cyclodextrin–Ionic Liquid Polyurethane-Modified Magnetic Sorbent for the Removal of PFOA, PFOS, and Cr(VI) from Water. *ACS Sustainable Chemistry & Engineering*, [online] 5(10), pp.9223–9232. https://doi.org/10.1021/acssuschemeng.7b02186.

Baik, S.K., Ha, D.W., Ko, R.K. and Kwon, J.M., 2010. Magnetic field and gradient analysis around matrix for HGMS. *Physica C: Superconductivity and its Applications*, [online] 470(20), pp.1831–1836. https://doi.org/10.1016/j.physc.2010.05.217.

Bao, S., Li, K., Ning, P., Peng, J., Jin, X. and Tang, L., 2017. Highly effective removal of mercury and lead ions from wastewater by mercaptoamine-functionalised silica-coated magnetic nano-adsorbents: Behaviours and mechanisms. *Applied Surface Science*, [online] 393, pp.457–466. https://doi.org/10.1016/j.apsusc.2016.09.098.

Benelmekki, M., Montras, A., Martins, A.J., Coutinho, P.J.G. and Martinez, Ll.M., 2011. Magnetophoresis behaviour at low gradient magnetic field and size control of nickel single core nanobeads. *Journal of Magnetism and Magnetic Materials*, [online] 323(15), pp.1945–1949. https://doi.org/10.1016/j.jmmm.2011.02.027.

Berensmeier, S., 2006. Magnetic particles for the separation and purification of nucleic acids. *Applied Microbiology and Biotechnology*, [online] 73(3), pp.495–504. https://doi.org/10.1007/s00253-006-0675-0.

Bharath, G., Alhseinat, E., Ponpandian, N., Khan, M.A., Siddiqui, M.R., Ahmed, F. and Alsharaeh, E.H., 2017. Development of adsorption and electrosorption techniques for removal of organic and inorganic pollutants from wastewater using novel magnetite/porous graphene-based nanocomposites. *Separation and Purification Technology*, [online] 188, pp.206–218. https://doi.org/10.1016/j.seppur.2017.07.024.

Binder, C., Feichtinger, C., Schmid, H.-J., Thürey, N., Peukert, W. and Rüde, U., 2006. Simulation of the hydrodynamic drag of aggregated particles. *Journal of Colloid and Interface Science*, [online] 301(1), pp.155–167. https://doi.org/10.1016/j.jcis.2006.04.045.

Bronkala, W.J., 2000. Magnetic Separation. In: *Ullmann's Encyclopedia of Industrial Chemistry*. [online] Weinheim, Germany: Wiley-VCH Verlag GmbH & Co. KGaA. pp.133–144. https://doi.org/10.1002/14356007.b02_19.

Calì, E., Qi, J., Preedy, O., Chen, S., Boldrin, D., Branford, W.R., Vandeperre, L. and Ryan, M.P., 2018. Functionalised magnetic nanoparticles for uranium adsorption with ultra-high capacity and selectivity. *Journal of Materials Chemistry A*, [online] 6(7), pp.3063–3073. https://doi.org/10.1039/C7TA09240G.

Cao, Q., Han, X. and Li, L., 2012. Numerical analysis of magnetic nanoparticle transport in microfluidic systems under the influence of permanent magnets. *Journal of Physics D: Applied Physics*, [online] 45(46), p.465001. https://doi.org/10.1088/0022-3727/45/46/465001.

Capuzzi, S. and Timelli, G., 2018. Preparation and Melting of Scrap in Aluminum Recycling: A Review. *Metals*, [online] 8(4), p.249. https://doi.org/10.3390/met8040249.

Che, H.X., Yeap, S.P., Osman, M.S., Ahmad, A.L. and Lim, J., 2014. Directed Assembly of Bifunctional Silica–Iron Oxide Nanocomposite with Open Shell Structure. *ACS Applied Materials & Interfaces*, [online] 6(19), pp.16508–16518. https://doi.org/10.1021/am5050949.

Chen, G.D., Alberts, C.J., Rodriguez, W. and Toner, M., 2010. Concentration and Purification of Human Immunodeficiency Virus Type 1 Virions by Microfluidic Separation of Superparamagnetic Nanoparticles. *Analytical Chemistry*, [online] 82(2), pp.723–728. https://doi.org/10.1021/ac9024522.

Chen, K., He, J., Li, Y., Cai, X., Zhang, K., Liu, T., Hu, Y., Lin, D., Kong, L. and Liu, J., 2017. Removal of cadmium and lead ions from water by sulfonated magnetic nanoparticle adsorbents. *Journal of Colloid and Interface Science*, [online] 494, pp.307–316. https://doi.org/10.1016/j.jcis.2017.01.082.

Chen, Y., Xianyu, Y., Wang, Y., Zhang, X., Cha, R., Sun, J. and Jiang, X., 2015. One-step detection of pathogens and viruses: Combining magnetic relaxation switching and magnetic separation. *ACS Nano*, [online] 9(3), pp.3184–3191. https://doi.org/10.1021/acsnano.5b00240.

Chong, P.H., Tan, Y.W., Teoh, Y.P., Lim, C.H., Toh, P.Y., Lim, J. and Leong, S.S., 2021. Continuous Flow Low Gradient Magnetophoresis of Magnetic Nanoparticles: Separation Kinetic Modelling and Simulation. *Journal of*

Superconductivity and Novel Magnetism, [online] 34(8), pp.2151–2165. https://doi.org/10.1007/s10948-021-05893-z.

Chong, W.H., Leong, S.S. and Lim, J., 2021. Design and operation of magnetophoretic systems at microscale: Device and particle approaches. *Electrophoresis*, [online] 42(21–22), pp.2303–2328. https://doi.org/10.1002/elps.202100081.

Chorny, M., Fishbein, I., Forbes, S. and Alferiev, I., 2011. Magnetic nanoparticles for targeted vascular delivery. *IUBMB Life*, [online] 63(8), pp.613–620. https://doi.org/10.1002/iub.479.

Cieśla, A., 2003. Practical aspects of high gradient magnetic separation using superconducting magnets. *Physicochemical Problems of Mineral Processing*, 37, pp.169–181.

Corchero, J.L. and Villaverde, A., 2009. Biomedical applications of distally controlled magnetic nanoparticles. *Trends Biotechnol.*, [online] 27(8), pp.468–476. https://doi.org/10.1016/j.tibtech.2009.04.003.

Darras, A., Fiscina, J., Vandewalle, N. and Lumay, G., 2017. Relating Brownian motion to diffusion with superparamagnetic colloids. *American Journal of Physics*, [online] 85(4), pp.265–270. https://doi.org/10.1119/1.4975382.

Dauer, R.R. and Dunlop, E.H., 1991. High gradient magnetic separation of yeast. *Biotechnology and Bioengineering*, [online] 37(11), pp.1021–1028. https://doi.org/10.1002/bit.260371106.

Devi, S.M., Nivetha, A. and Prabha, I., 2019. Superparamagnetic Properties and Significant Applications of Iron Oxide Nanoparticles for Astonishing Efficacy—a Review. *Journal of Superconductivity and Novel Magnetism*, [online] 32(2), pp.127–144. https://doi.org/10.1007/s10948-018-4929-8.

Ditsch, A., Laibinis, P.E., Wang, D.I.C. and Hatton, T.A., 2005a. Controlled clustering and enhanced stability of polymer-coated magnetic nanoparticles. *Langmuir*, 21(13), pp.6006–6018. https://doi.org/10.1021/la047057+.

Ditsch, A., Lindenmann, S., Laibinis, P.E., Wang, D.I.C. and Hatton, T.A., 2005b. High-Gradient Magnetic Separation of Magnetic Nanoclusters. *Industrial & Engineering Chemistry Research*, [online] 44(17), pp.6824–6836. https://doi.org/10.1021/ie048841s.

Dobson, J., 2006. Gene therapy progress and prospects: magnetic nanoparticle-based gene delivery. *Gene Therapy*, [online] 13(4), pp.283–287. https://doi.org/10.1038/sj.gt.3302720.

Elmobarak, W.F. and Almomani, F., 2021. Application of magnetic nanoparticles for the removal of oil from oil-in-water emulsion:

Regeneration/reuse of spent particles. *Journal of Petroleum Science and Engineering*, [online] 203, p.108591. https://doi.org/10.1016/j.petrol.2021.108591.

Faraudo, J., Andreu, J.S., Calero, C. and Camacho, J., 2016. Predicting the Self-Assembly of Superparamagnetic Colloids under Magnetic Fields. *Advanced Functional Materials*, [online] 26(22), pp.3837–3858. https://doi.org/10.1002/adfm.201504839.

Faraudo, J., Andreu, J.S. and Camacho, J., 2013. Understanding diluted dispersions of superparamagnetic particles under strong magnetic fields: a review of concepts, theory and simulations. *Soft Matter*, [online] 9(29), p.6654. https://doi.org/10.1039/c3sm00132f.

Faraudo, J. and Camacho, J., 2010. Cooperative magnetophoresis of superparamagnetic colloids: theoretical aspects. *Colloid and Polymer Science*, [online] 288(2), pp.207–215. https://doi.org/10.1007/s00396-009-2107-z.

Feng, B., Hong, R.Y., Wang, L.S., Guo, L., Li, H.Z., Ding, J., Zheng, Y. and Wei, D.G., 2008. Synthesis of Fe3O4/APTES/PEG diacid functionalized magnetic nanoparticles for MR imaging. *Colloids and Surfaces A: Physicochemical and Engineering Aspects*, [online] 328(1–3), pp.52–59. https://doi.org/10.1016/j.colsurfa.2008.06.024.

Forbes, T.P. and Forry, S.P., 2012. Microfluidic magnetophoretic separations of immunomagnetically labeled rare mammalian cells. *Lab Chip*, [online] 12(8), p.1471. https://doi.org/10.1039/c2lc40113d.

Friedman, G. and Yellen, B., 2005. Magnetic separation, manipulation and assembly of solid phase in fluids. *Current Opinion in Colloid & Interface Science*, [online] 10(3–4), pp.158–166. https://doi.org/10.1016/j.cocis.2005.08.002.

Gassner, A.L., Abonnenc, M., Chen, H.X., Morandini, J., Josserand, J., Rossier, J.S., Busnel, J.M. and Girault, H.H., 2009. Magnetic forces produced by rectangular permanent magnets in static microsystems. *Lab Chip*, 9(16), pp.2356–2363. https://doi.org/10.1039/b901865d.

Ge, L., Wang, W., Peng, Z., Tan, F., Wang, X., Chen, J. and Qiao, X., 2018. Facile fabrication of Fe@MgO magnetic nanocomposites for efficient removal of heavy metal ion and dye from water. *Powder Technology*, [online] 326, pp.393–401. https://doi.org/10.1016/j.powtec.2017.12.003.

Ge, W., Encinas, A., Araujo, E. and Song, S., 2017. Magnetic matrices used in high gradient magnetic separation (HGMS): A review. *Results in Physics*, [online] 7, pp.4278–4286. https://doi.org/10.1016/j.rinp.2017.10.055.

Golas, P.L., Louie, S., Lowry, G. v., Matyjaszewski, K. and Tilton, R.D., 2010. Comparative Study of Polymeric Stabilizers for Magnetite Nanoparticles Using

ATRP. *Langmuir*, [online] 26(22), pp.16890–16900. https://doi.org/10.1021/la103098q.

Gómez-Pastora, J., Bringas, E. and Ortiz, I., 2014. Recent progress and future challenges on the use of high performance magnetic nano-adsorbents in environmental applications. *Chemical Engineering Journal*, [online] 256, pp.187–204. https://doi.org/10.1016/j.cej.2014.06.119.

Gómez-Pastora, J., Xue, X., Karampelas, I.H., Bringas, E., Furlani, E.P. and Ortiz, I., 2017. Analysis of separators for magnetic beads recovery: From large systems to multifunctional microdevices. *Separation and Purification Technology*, [online] 172, pp.16–31. https://doi.org/10.1016/j.seppur.2016.07.050.

Gourikutty, S.B.N., Chang, C.-P. and Puiu, P.D., 2016. Microfluidic immunomagnetic cell separation from whole blood. *Journal of Chromatography B*, [online] 1011, pp.77–88. https://doi.org/10.1016/j.jchromb.2015.12.016.

Gunther, G.G., 1909. Electro-magnetic ore separation. *Journal of Chemical Information and Modeling*, 53(9).

Gupta, A.K. and Wells, S., 2004. Surface-Modified Superparamagnetic Nanoparticles for Drug Delivery: Preparation, Characterization, and Cytotoxicity Studies. *IEEE Transactions on Nanobioscience*, [online] 3(1), pp.66–73. https://doi.org/10.1109/TNB.2003.820277.

Hatch, G.P. and Stelter, R.E., 2001. Magnetic design considerations for devices and particles used for biological high-gradient magnetic separation (HGMS) systems. *Journal of Magnetism and Magnetic Materials*, [online] 225(1–2), pp.262–276. https://doi.org/10.1016/S0304-8853(00)01250-6.

Heinrich, D., Goñi, A.R., Osán, T.M., Cerioni, L.M.C., Smessaert, A., Klapp, S.H.L., Faraudo, J., Pusiol, D.J. and Thomsen, C., 2015. Effects of magnetic field gradients on the aggregation dynamics of colloidal magnetic nanoparticles. *Soft Matter*, [online] 11(38), pp.7606–7616. https://doi.org/10.1039/C5SM00541H.

Helseth, L.E. and Skodvin, T., 2009. Optical monitoring of low-field magnetophoretic separation of particles. *Measurement Science and Technology*, [online] 20(9), p.095202. https://doi.org/10.1088/0957-0233/20/9/095202.

Hyun, K.-A. and Jung, H.-I., 2013. Microfluidic devices for the isolation of circulating rare cells: A focus on affinity-based, dielectrophoresis, and hydrophoresis. *Electrophoresis*, [online] 34(7), pp.1028–1041. https://doi.org/10.1002/elps.201200417.

Jeong, K., Petrakis, L., Takayasu, M. and Friedlaender, F., 1982. High gradient magnetic separation I: The removal of solids from shale oils. *IEEE*

Transactions on Magnetics, [online] 18(6), pp.1692–1694. https://doi.org/10.1109/TMAG.1982.1062009.

de Jong, 2008. Drug delivery and nanoparticles: Applications and hazards. *International Journal of Nanomedicine*, [online] 3(2), p.133. https://doi.org/10.2147/IJN.S596.

Jordens, A., Sheridan, R.S., Rowson, N.A. and Waters, K.E., 2014. Processing a rare earth mineral deposit using gravity and magnetic separation. *Minerals Engineering*, [online] 62, pp.9–18. https://doi.org/10.1016/j.mineng.2013.09.011.

Kang, T., Li, F., Baik, S., Shao, W., Ling, D. and Hyeon, T., 2017. Surface design of magnetic nanoparticles for stimuli-responsive cancer imaging and therapy. *Biomaterials*, [online] 136, pp.98–114. https://doi.org/10.1016/j.biomaterials.2017.05.013.

Kärger, J., 1992. Straightforward derivation of the long-time limit of the mean-square displacement in one-dimensional diffusion. *Physical Review A*, [online] 45(6), pp.4173–4174. https://doi.org/10.1103/PhysRevA.45.4173.

Kayvani Fard, A., Rhadfi, T., Mckay, G., Al-marri, M., Abdala, A., Hilal, N. and Hussien, M.A., 2016. Enhancing oil removal from water using ferric oxide nanoparticles doped carbon nanotubes adsorbents. *Chemical Engineering Journal*, [online] 293, pp.90–101. https://doi.org/10.1016/j.cej.2016.02.040.

Kelland, D., 1973. High gradient magnetic separation applied to mineral beneficiation. *IEEE Transactions on Magnetics*, [online] 9(3), pp.307–310. https://doi.org/10.1109/TMAG.1973.1067683.

Khashan, S.A. and Furlani, E.P., 2012. Effects of particle–fluid coupling on particle transport and capture in a magnetophoretic microsystem. *Microfluidics and Nanofluidics*, [online] 12(1–4), pp.565–580. https://doi.org/10.1007/s10404-011-0898-y.

Khashan, S.A. and Furlani, E.P., 2013. Coupled particle–fluid transport and magnetic separation in microfluidic systems with passive magnetic functionality. *Journal of Physics D: Applied Physics*, [online] 46(12), p.125002. https://doi.org/10.1088/0022-3727/46/12/125002.

Khashan, S.A. and Furlani, E.P., 2014. Scalability analysis of magnetic bead separation in a microchannel with an array of soft magnetic elements in a uniform magnetic field. *Separation and Purification Technology*, [online] 125, pp.311–318. https://doi.org/10.1016/j.seppur.2014.02.007.

Khizar, S., ben Halima, H., Ahmad, N.M., Zine, N., Errachid, A. and Elaissari, A., 2020. Magnetic nanoparticles in microfluidic and sensing: From transport to detection. *Electrophoresis*, [online] 41(13–14), pp.1206–1224. https://doi.org/10.1002/elps.201900377.

Kim, E.-J., Lee, C.-S., Chang, Y.-Y. and Chang, Y.-S., 2013. Hierarchically Structured Manganese Oxide-Coated Magnetic Nanocomposites for the Efficient Removal of Heavy Metal Ions from Aqueous Systems. *ACS Applied Materials & Interfaces*, [online] 5(19), pp.9628–9634. https://doi.org/10.1021/am402615m.

Ko, S., Kim, E.S., Park, S., Daigle, H., Milner, T.E., Huh, C., Bennetzen, M. v. and Geremia, G.A., 2017. RETRACTED ARTICLE: Amine functionalized magnetic nanoparticles for removal of oil droplets from produced water and accelerated magnetic separation. *Journal of Nanoparticle Research*, [online] 19(4), p.132. https://doi.org/10.1007/s11051-017-3826-6.

Kolosnjaj-Tabi, J. and Wilhelm, C., 2017. Magnetic nanoparticles in cancer therapy: how can thermal approaches help? *Nanomedicine*, [online] 12(6), pp.573–575. https://doi.org/10.2217/nnm-2017-0014.

Krishnan, J.N., Kim, C., Park, H.J., Kang, J.Y., Kim, T.S. and Kim, S.K., 2009. Rapid microfluidic separation of magnetic beads through dielectrophoresis and magnetophoresis. *ELECTROPHORESIS*, [online] 30(9), pp.1457–1463. https://doi.org/10.1002/elps.200800646.

de Las Cuevas, G., Faraudo, J. and Camacho, J., 2008. Low-Gradient Magnetophoresis through Field-Induced Reversible Aggregation. *The Journal of Physical Chemistry C*, [online] 112(4), pp.945–950. https://doi.org/10.1021/jp0755286.

Laurent, S., Forge, D., Port, M., Roch, A., Robic, C., vander Elst, L. and Muller, R.N., 2008. Magnetic Iron Oxide Nanoparticles: Synthesis, Stabilization, Vectorization, Physicochemical Characterizations, and Biological Applications. *Chemical Reviews*, [online] 108(6), pp.2064–2110. https://doi.org/10.1021/cr068445e.

Lee, J.-H., Kim, J. and Cheon, J., 2013. Magnetic nanoparticles for multi-imaging and drug delivery. *Molecules and Cells*, [online] 35(4), pp.274–284. https://doi.org/10.1007/s10059-013-0103-0.

Lee, S.L., O'Connor, T.F., Yang, X., Cruz, C.N., Chatterjee, S., Madurawe, R.D., Moore, C.M. v., Yu, L.X. and Woodcock, J., 2015. Modernizing Pharmaceutical Manufacturing: from Batch to Continuous Production. *Journal of Pharmaceutical Innovation*, [online] 10(3), pp.191–199. https://doi.org/10.1007/s12247-015-9215-8.

Leong, S.S., Ahmad, Z., Camacho, J., Faraudo, J. and Lim, J., 2017. Kinetics of Low Field Gradient Magnetophoresis in the Presence of Magnetically Induced Convection. *The Journal of Physical Chemistry C*, [online] 121(9), pp.5389–5407. https://doi.org/10.1021/acs.jpcc.6b13090.

Leong, S.S., Ahmad, Z. and Lim, J., 2015. Magnetophoresis of superparamagnetic nanoparticles at low field gradient: hydrodynamic effect. *Soft Matter*, [online] 11(35), pp.6968–6980. https://doi.org/10.1039/C5SM01422K.

Leong, S.S., Ahmad, Z., Low, S.C., Camacho, J., Faraudo, J. and Lim, J.K., 2020. Unified View of Magnetic Nanoparticle Separation under Magnetophoresis. *Langmuir*, 36(28), pp.8033–8055. https://doi.org/10.1021/acs.langmuir.0c00839.

Leong, S.S., Yeap, S.P. and Lim, J., 2016. Working principle and application of magnetic separation for biomedical diagnostic at high- and low-field gradients. *Interface Focus*, [online] 6(6), p.20160048. https://doi.org/10.1098/rsfs.2016.0048.

Li, H., Li, Z., Liu, T., Xiao, X., Peng, Z. and Deng, L., 2008. A novel technology for biosorption and recovery hexavalent chromium in wastewater by bio-functional magnetic beads. *Bioresource Technology*, [online] 99(14), pp.6271–6279. https://doi.org/10.1016/j.biortech.2007.12.002.

Lien, K.-Y., Lin, J.-L., Liu, C.-Y., Lei, H.-Y. and Lee, G.-B., 2007. Purification and enrichment of virus samples utilizing magnetic beads on a microfluidic system. *Lab on a Chip*, [online] 7(7), pp.868–877. https://doi.org/10.1039/b700516d.

Lim, J., Lanni, C., Evarts, E.R., Lanni, F., Tilton, R.D. and Majetich, S.A., 2011. Magnetophoresis of Nanoparticles. *ACS Nano*, [online] 5(1), pp.217–226. https://doi.org/10.1021/nn102383s.

Lim, J., Yeap, S.P., Leow, C.H., Toh, P.Y. and Low, S.C., 2014. Magnetophoresis of iron oxide nanoparticles at low field gradient: The role of shape anisotropy. *Journal of Colloid and Interface Science*, [online] 421, pp.170–177. https://doi.org/10.1016/j.jcis.2014.01.044.

Lim, J., Yeap, S.P. and Low, S.C., 2014. Challenges associated to magnetic separation of nanomaterials at low field gradient. *Separation and Purification Technology*, [online] 123, pp.171–174. https://doi.org/10.1016/j.seppur.2013.12.038.

Lim, J.K., Chieh, D.C.J., Jalak, S.A., Toh, P.Y., Yasin, N.H.M., Ng, B.W. and Ahmad, A.L., 2012. Rapid magnetophoretic separation of microalgae. *Small*, [online] 8(11), pp.1683–1692. https://doi.org/10.1002/smll.201102400.

Lim, J.K., Majetich, S.A. and Tilton, R.D., 2009. Stabilization of Superparamagnetic Iron Oxide Core−Gold Shell Nanoparticles in High Ionic Strength Media. *Langmuir*, [online] 25(23), pp.13384–13393. https://doi.org/10.1021/la9019734.

Lin, Y., Weng, C. and Chen, F., 2008. Effective removal of AB24 dye by nano/micro-size zero-valent iron. *Separation and Purification Technology*, [online] 64(1), pp.26–30. https://doi.org/10.1016/j.seppur.2008.08.012.

Liu, J., Cao, D. and Zhang, L., 2008. Molecular Dynamics Study on Nanoparticle Diffusion in Polymer Melts: A Test of the Stokes−Einstein Law. *The Journal of Physical Chemistry C*, [online] 112(17), pp.6653–6661. https://doi.org/10.1021/jp800474t.

Liu, Y., Wang, W., Jia, M., Liu, R., Liu, Q., Xiao, H., Li, J., Xue, Y., Wang, Y. and Yan, C., 2018. Recent advances in microscale separation. *Electrophoresis*, [online] 39(1), pp.8–33. https://doi.org/10.1002/elps.201700271.

Lone, I.H., Ahmed, J. and Ahmad, T., 2018. Reverse Micellar Synthesis, Characterization, Magnetic and Ferroelectric Properties of YFeO3 Nanoparticles. *Materials Today: Proceedings*, [online] 5(7), pp.15303–15310. https://doi.org/10.1016/j.matpr.2018.05.010.

Long, Y., Xiao, L. and Cao, Q., 2017. Co-polymerization of catechol and polyethylenimine on magnetic nanoparticles for efficient selective removal of anionic dyes from water. *Powder Technology*, [online] 310, pp.24–34. https://doi.org/10.1016/j.powtec.2017.01.013.

Ma, Y., Chen, T., Iqbal, M.Z., Yang, F., Hampp, N., Wu, A. and Luo, L., 2019. Applications of magnetic materials separation in biological nanomedicine. *Electrophoresis*, [online] 40(16–17), pp.2011–2028. https://doi.org/10.1002/elps.201800401.

Ma, Z., Shan, C., Liang, J. and Tong, M., 2018. Efficient adsorption of Selenium(IV) from water by hematite modified magnetic nanoparticles. *Chemosphere*, [online] 193, pp.134–141. https://doi.org/10.1016/j.chemosphere.2017.11.005.

Mariani, G., Fabbri, M., Negrini, F. and Ribani, P.L., 2010. High-Gradient Magnetic Separation of pollutant from wastewaters using permanent magnets. *Separation and Purification Technology*, [online] 72(2), pp.147–155. https://doi.org/10.1016/j.seppur.2010.01.017.

Mashhadi Malekzadeh, A., Ramazani, A., Tabatabaei Rezaei, S.J. and Niknejad, H., 2017. Design and construction of multifunctional hyperbranched polymers coated magnetite nanoparticles for both targeting magnetic resonance imaging and cancer therapy. *Journal of Colloid and Interface Science*, [online] 490, pp.64–73. https://doi.org/10.1016/j.jcis.2016.11.014.

Mathew, B., Alazzam, A., Abutayeh, M., Gawanmeh, A. and Khashan, S., 2015. Modeling the trajectory of microparticles subjected to dielectrophoresis in a microfluidic device for field flow fractionation. *Chemical Engineering Science*, [online] 138, pp.266–280. https://doi.org/10.1016/j.ces.2015.07.014.

de Melo, F.M., Almeida, S. da N., Santos, A.D. dos and Toma, H.E., 2017. Magnetophoresis of Superparamagnetic Nanoparticles Applied to the Extraction of Lanthanide Ions in the Presence of Magnetic Field. *NanoWorld Journal*, [online] 03(02), pp.38–43. https://doi.org/10.17756/nwj.2017-044.

Meng, C., Zhikun, W., Qiang, L., Chunling, L., Shuangqing, S. and Songqing, H., 2018. Preparation of amino-functionalized Fe3O4@mSiO2 core-shell magnetic nanoparticles and their application for aqueous Fe3+ removal. *Journal of Hazardous Materials*, [online] 341, pp.198–206. https://doi.org/10.1016/j.jhazmat.2017.07.062.

Moeser, G.D., Roach, K.A., Green, W.H., Alan Hatton, T. and Laibinis, P.E., 2004. High-gradient magnetic separation of coated magnetic nanoparticles. *AIChE Journal*, [online] 50(11), pp.2835–2848. https://doi.org/10.1002/aic.10270.

Moeser, G.D., Roach, K.A., Green, W.H., Laibinis, P.E. and Hatton, T.A., 2002. Water-Based Magnetic Fluids as Extractants for Synthetic Organic Compounds. *Industrial & Engineering Chemistry Research*, [online] 41(19), pp.4739–4749. https://doi.org/10.1021/ie0202118.

Mohammed, L., Gomaa, H.G., Ragab, D. and Zhu, J., 2017. Magnetic nanoparticles for environmental and biomedical applications: A review. *Particuology*, [online] 30, pp.1–14. https://doi.org/10.1016/j.partic.2016.06.001.

Morgan, D.G. and Bronkala, W.J., 1993. The Selection and Application of Magnetic Separation Equipment. Part II. *Magnetic and Electrical Separation*, [online] 4(3), pp.151–172. https://doi.org/10.1155/1993/81597.

Moy, A.J. and Tunnell, J.W., 2017. Combinatorial immunotherapy and nanoparticle mediated hyperthermia. *Advanced Drug Delivery Reviews*, [online] 114, pp.175–183. https://doi.org/10.1016/j.addr.2017.06.008.

Mu, X., Qiao, J., Qi, L., Dong, P. and Ma, H., 2014. Poly(2-Vinyl-4,4-dimethylazlactone)-Functionalized Magnetic Nanoparticles as Carriers for Enzyme Immobilization and Its Application. *ACS Applied Materials & Interfaces*, [online] 6(23), pp.21346–21354. https://doi.org/10.1021/am5063025.

Narayana Iyengar, S., Kumar, T., Mårtensson, G. and Russom, A., 2021. High resolution and rapid separation of bacteria from blood using elasto-inertial microfluidics. *Electrophoresis*, [online] 42(23), pp.2538–2551. https://doi.org/10.1002/elps.202100140.

Ngo, H.T., Gandra, N., Fales, A.M., Taylor, S.M. and Vo-Dinh, T., 2016. Sensitive DNA detection and SNP discrimination using ultrabright SERS nanorattles and magnetic beads for malaria diagnostics. *Biosensors and Bioelectronics*, [online] 81, pp.8–14. https://doi.org/10.1016/j.bios.2016.01.073.

Oberteuffer, J., 1973. High gradient magnetic separation. *IEEE Transactions on Magnetics*, [online] 9(3), pp.303–306. https://doi.org/10.1109/TMAG.1973.1067673.

Oberteuffer, J., 1974. Magnetic separation: A review of principles, devices, and applications. *IEEE Transactions on Magnetics*, [online] 10(2), pp.223–238. https://doi.org/10.1109/TMAG.1974.1058315.

Oberteuffer, J., Wechsler, I., Marston, P. and McNallan, M., 1975. High gradient magnetic filtration of steel mill process and waste waters. *IEEE Transactions on Magnetics*, [online] 11(5), pp.1591–1593. https://doi.org/10.1109/TMAG.1975.1058803.

Oroujeni, M., Kaboudin, B., Xia, W., Jönsson, P. and Ossipov, D.A., 2018. Conjugation of cyclodextrin to magnetic Fe3O4 nanoparticles via polydopamine coating for drug delivery. *Progress in Organic Coatings*, [online] 114, pp.154–161. https://doi.org/10.1016/j.porgcoat.2017.10.007.

Pamme, N., 2006. Magnetism and microfluidics. *Lab Chip*, [online] 6(1), pp.24–38. https://doi.org/10.1039/B513005K.

Pamme, N. and Manz, A., 2004. On-Chip Free-Flow Magnetophoresis: Continuous Flow Separation of Magnetic Particles and Agglomerates. *Analytical Chemistry*, [online] 76(24), pp.7250–7256. https://doi.org/10.1021/ac049183o.

Pamme, N. and Wilhelm, C., 2006. Continuous sorting of magnetic cells via on-chip free-flow magnetophoresis. *Lab Chip*, [online] 6(8), pp.974–980. https://doi.org/10.1039/b604542a.

Parker, M.R., 1977. The physics of magnetic separation. *Contemporary Physics*, [online] 18(3), pp.279–306. https://doi.org/10.1080/00107517708231486.

Phenrat, T., Saleh, N., Sirk, K., Tilton, R.D. and Lowry, G. v., 2007. Aggregation and Sedimentation of Aqueous Nanoscale Zerovalent Iron Dispersions. *Environmental Science & Technology*, [online] 41(1), pp.284–290. https://doi.org/10.1021/es061349a.

Ramos, A.P., 2017. Dynamic Light Scattering Applied to Nanoparticle Characterization. In: *Nanocharacterization Techniques*. [online] Elsevier. pp.99–110. https://doi.org/10.1016/B978-0-323-49778-7.00004-7.

Rezayan, A.H., Mousavi, M., Kheirjou, S., Amoabediny, G., Ardestani, M.S. and Mohammadnejad, J., 2016. Monodisperse magnetite (Fe3O4) nanoparticles modified with water soluble polymers for the diagnosis of breast cancer by MRI method. *Journal of Magnetism and Magnetic Materials*, [online] 420, pp.210–217. https://doi.org/10.1016/j.jmmm.2016.07.003.

Robert, D., Pamme, N., Conjeaud, H., Gazeau, F., Iles, A. and Wilhelm, C., 2011. Cell sorting by endocytotic capacity in a microfluidic magnetophoresis device. *Lab on a Chip*, [online] 11(11), pp.1902–1912. https://doi.org/10.1039/c0lc00656d.

Runkana, V., Somasundaran, P. and Kapur, P.C., 2006. A population balance model for flocculation of colloidal suspensions by polymer bridging. *Chemical Engineering Science*, [online] 61(1), pp.182–191. https://doi.org/10.1016/j.ces.2005.01.046.

Šafařík, I. and Šafaříková, M., 1999. Use of magnetic techniques for the isolation of cells. *Journal of Chromatography B: Biomedical Sciences and Applications*, [online] 722(1–2), pp.33–53. https://doi.org/10.1016/S0378-4347(98)00338-7.

Sahraei, R., Sekhavat Pour, Z. and Ghaemy, M., 2017. Novel magnetic bio-sorbent hydrogel beads based on modified gum tragacanth/graphene oxide: Removal of heavy metals and dyes from water. *Journal of Cleaner Production*, [online] 142, pp.2973–2984. https://doi.org/10.1016/j.jclepro.2016.10.170.

Salmani, M.M., Hashemian, M. and Khandan, A., 2020. Therapeutic effect of magnetic nanoparticles on calcium silicate bioceramic in alternating field for biomedical application. *Ceramics International*, [online] 46(17), pp.27299–27307. https://doi.org/10.1016/j.ceramint.2020.07.215.

Sangaiya, P. and Jayaprakash, R., 2018. A Review on Iron Oxide Nanoparticles and Their Biomedical Applications. *Journal of Superconductivity and Novel Magnetism*, [online] 31(11), pp.3397–3413. https://doi.org/10.1007/s10948-018-4841-2.

Schaller, V., Kräling, U., Rusu, C., Petersson, K., Wipenmyr, J., Krozer, A., Wahnström, G., Sanz-Velasco, A., Enoksson, P. and Johansson, C., 2008. Motion of nanometer sized magnetic particles in a magnetic field gradient. *Journal of Applied Physics*, [online] 104(9), p.093918. https://doi.org/10.1063/1.3009686.

Schrick, B., Hydutsky, B.W., Blough, J.L. and Mallouk, T.E., 2004. Delivery Vehicles for Zerovalent Metal Nanoparticles in Soil and Groundwater. *Chemistry of Materials*, [online] 16(11), pp.2187–2193. https://doi.org/10.1021/cm0218108.

Seebergh, J.E. and Berg, J.C., 1994. Depletion flocculation of aqueous, electrosterically-stabilized latex dispersions. *Langmuir*, [online] 10(2), pp.454–463. https://doi.org/10.1021/la00014a020.

Shaikh, A.M.H. and Dixit, S.G., 1992. Removal of phosphate from waters by precipitation and high gradient magnetic separation. *Water Research*, [online] 26(6), pp.845–852. https://doi.org/10.1016/0043-1354(92)90016-W.

Shen, Y.F., Tang, J., Nie, Z.H., Wang, Y.D., Ren, Y. and Zuo, L., 2009. Tailoring size and structural distortion of Fe3O4 nanoparticles for the purification of contaminated water. *Bioresource Technology*, [online] 100(18), pp.4139–4146. https://doi.org/10.1016/j.biortech.2009.04.004.

Simonsen, G., Strand, M. and Øye, G., 2018. Potential applications of magnetic nanoparticles within separation in the petroleum industry. *Journal of Petroleum Science and Engineering*, [online] 165, pp.488–495. https://doi.org/10.1016/j.petrol.2018.02.048.

Singh, A.K., Srivastava, O.N. and Singh, K., 2017. Shape and Size-Dependent Magnetic Properties of Fe3O4 Nanoparticles Synthesized Using Piperidine. *Nanoscale Research Letters*, [online] 12(1), p.298. https://doi.org/10.1186/s11671-017-2039-3.

Song, E.-Q., Hu, J., Wen, C.-Y., Tian, Z.-Q., Yu, X., Zhang, Z.-L., Shi, Y.-B. and Pang, D.-W., 2011. Fluorescent-Magnetic-Biotargeting Multifunctional Nanobioprobes for Detecting and Isolating Multiple Types of Tumor Cells. *ACS Nano*, [online] 5(2), pp.761–770. https://doi.org/10.1021/nn1011336.

Stephens, J.R., Beveridge, J.S. and Williams, M.E., 2012. Analytical methods for separating and isolating magnetic nanoparticles. *Physical Chemistry Chemical Physics*, [online] 14(10), p.3280. https://doi.org/10.1039/c2cp22982j.

Sun, C., Lee, J.S.H. and Zhang, M., 2008. Magnetic nanoparticles in MR imaging and drug delivery. *Advanced Drug Delivery Reviews*, [online] 60(11), pp.1252–1265. https://doi.org/10.1016/j.addr.2008.03.018.

Sun, J., Shi, Z., Chen, S. and Jia, S., 2019. Experimental and numerical analysis of the magnetophoresis of magnetic nanoparticles under the influence of cylindrical permanent magnet. *Journal of Magnetism and Magnetic Materials*, [online] 475, pp.703–714. https://doi.org/10.1016/j.jmmm.2018.11.124.

Sun, L., K. Siddique, M., Wang, L. and Li, S., 2021. Mixing characteristics of a bubble mixing microfluidic chip for genomic DNA extraction based on magnetophoresis: CFD simulation and experiment. *Electrophoresis*, [online] 42(21–22), pp.2365–2374. https://doi.org/10.1002/elps.202000295.

Svoboda, J., 2004. *Magnetic Techniques for the Treatment of Materials*. [online] *Magnetic Techniques for the Treatment of Materials*. Dordrecht: Kluwer Academic Publishers. https://doi.org/10.1007/1-4020-2107-0.

Taheri-Ledari, R., Rahimi, J. and Maleki, A., 2019. Synergistic catalytic effect between ultrasound waves and pyrimidine-2,4-diamine-functionalized magnetic nanoparticles: Applied for synthesis of 1,4-dihydropyridine pharmaceutical derivatives. *Ultrasonics Sonochemistry*, [online] 59, p.104737. https://doi.org/10.1016/j.ultsonch.2019.104737.

Tang, W., Jiang, D., Li, Z., Zhu, L., Shi, J., Yang, J. and Xiang, N., 2019. Recent advances in microfluidic cell sorting techniques based on both physical and biochemical principles. *Electrophoresis*, [online] 40(6), pp.930–954. https://doi.org/10.1002/elps.201800361.

Terashima, Y., Ozaki, H. and Sekine, M., 1986. Removal of dissolved heavy metals by chemical coagulation, magnetic seeding and high gradient magnetic filtration. *Water Research*, [online] 20(5), pp.537–545. https://doi.org/10.1016/0043-1354(86)90017-5.

Tham, F.K., Ng, W.M., Leong, S.S., Yeap, S.P., Low, S.C., Lee, H.L. and Lim, J., 2021. Magnetophoresis of Magnetic Pickering Emulsions Under Low Field Gradient: Macroscopic and Microscopic Motion. *Langmuir*, [online] 37(5), pp.1811–1822. https://doi.org/10.1021/acs.langmuir.0c03153.

Toh, P.Y., Ng, B.W., Ahmad, A.L., Chieh, D.C.J. and Lim, J., 2014. Magnetophoretic separation of Chlorella sp.: Role of cationic polymer binder. *Process Safety and Environmental Protection*, [online] 92(6), pp.515–521. https://doi.org/10.1016/j.psep.2014.03.010.

Toh, P.Y., Yeap, S.P., Kong, L.P., Ng, B.W., Chan, D.J.C., Ahmad, A.L. and Lim, J.K., 2012. Magnetophoretic removal of microalgae from fishpond water: Feasibility of high gradient and low gradient magnetic separation. *Chemical Engineering Journal*, [online] 211–212, pp.22–30. https://doi.org/10.1016/j.cej.2012.09.051.

Wang, X., Yue, H., Liu, G. and Zhao, Z., 2011. The Application of COMSOL Multiphysics in Direct Current Method Forward Modeling. *Procedia Earth and Planetary Sci*, [online] 3, pp.266–272. https://doi.org/10.1016/j.proeps.2011.09.093.

Warren L. McCabe, Julian C. Smith and Peter Harriott, 2018. *Unit Operations of Chemical Engineering Fifth Edition*. *Notes on Numerical Fluid Mechanics and Multidisciplinary Design*, .

Wills, B.A. and Finch, J.A., 2016. Magnetic and Electrical Separation. In: *Wills' Mineral Processing Technology*. [online] Elsevier. pp.381–407. https://doi.org/10.1016/B978-0-08-097053-0.00013-3.

Wu, W., He, Q. and Jiang, C., 2008. Magnetic Iron Oxide Nanoparticles: Synthesis and Surface Functionalization Strategies. *Nanoscale Research Letters*, [online] 3(11), p.397. https://doi.org/10.1007/s11671-008-9174-9.

Wu, X., Wu, H. and Hu, Y., 2011. Enhancement of separation efficiency on continuous magnetophoresis by utilizing L/T-shaped microchannels. *Microfluidics and Nanofluidics*, [online] 11(1), pp.11–24. https://doi.org/10.1007/s10404-011-0768-7.

Xu, H., Aguilar, Z.P., Yang, L., Kuang, M., Duan, H., Xiong, Y., Wei, H. and Wang, A., 2011. Antibody conjugated magnetic iron oxide nanoparticles for cancer cell separation in fresh whole blood. *Biomaterials*, [online] 32(36), pp.9758–9765. https://doi.org/10.1016/j.biomaterials.2011.08.076.

Yan, S., Zhang, J., Yuan, D. and Li, W., 2017. Hybrid microfluidics combined with active and passive approaches for continuous cell separation. *Electrophoresis*, [online] 38(2), pp.238–249. https://doi.org/10.1002/elps.201600386.

Yavuz, C.T., Mayo, J.T., Yu, W.W., Prakash, A., Falkner, J.C., Yean, S., Cong, L., Shipley, H.J., Kan, A., Tomson, M., Natelson, D. and Colvin, V.L., 2006. Low-Field Magnetic Separation of Monodisperse Fe $_3$ O $_4$ Nanocrystals. *Science*, [online] 314(5801), pp.964–967. https://doi.org/10.1126/science.1131475.

Yavuz, C.T., Prakash, A., Mayo, J.T. and Colvin, V.L., 2009. Magnetic separations: From steel plants to biotechnology. *Chemical Engineering Science*, [online] 64(10), pp.2510–2521. https://doi.org/10.1016/j.ces.2008.11.018.

Yeap, S.P., Ahmad, A.L., Ooi, B.S. and Lim, J., 2012. Electrosteric Stabilization and Its Role in Cooperative Magnetophoresis of Colloidal Magnetic Nanoparticles. *Langmuir*, [online] 28(42), pp.14878–14891. https://doi.org/10.1021/la303169g.

Yeap, S.P., Ahmad, A.L., Ooi, B.S. and Lim, J., 2015. Manipulating cluster size of polyanion-stabilized Fe3O4 magnetic nanoparticle clusters via electrostatic-mediated assembly for tunable magnetophoresis behavior. *Journal of Nanoparticle Research*, [online] 17(10), p.403. https://doi.org/10.1007/s11051-015-3207-y.

Yeap, S.P., Leong, S.S., Ahmad, A.L., Ooi, B.S. and Lim, J., 2014. On Size Fractionation of Iron Oxide Nanoclusters by Low Magnetic Field Gradient. *The Journal of Physical Chemistry C*, [online] 118(41), pp.24042–24054. https://doi.org/10.1021/jp504808v.

Yeap, S.P., Lim, J., Ooi, B.S. and Ahmad, A.L., 2018. Feasibility of Electrostatic-Mediated Post-Functionalization to Induce Long Term Colloidal Stability and Stability After Freeze Drying of Amphoteric Nanoparticles. *Colloid and Interface Science Communications*, [online] 23, pp.14–20. https://doi.org/10.1016/j.colcom.2018.02.003.

Ying, T.-Y., Yiacoumi, S. and Tsouris, C., 2000. High-gradient magnetically seeded filtration. *Chemical Engineering Science*, [online] 55(6), pp.1101–1113. https://doi.org/10.1016/S0009-2509(99)00383-8.

Zborowski, M., Ostera, G.R., Moore, L.R., Milliron, S., Chalmers, J.J. and Schechter, A.N., 2003. Red Blood Cell Magnetophoresis. *Biophys. J.*, [online] 84(4), pp.2638–2645. https://doi.org/10.1016/S0006-3495(03)75069-3.

Zborowski, M., Sun, L., Moore, L.R., Stephen Williams, P. and Chalmers, J.J., 1999. Continuous cell separation using novel magnetic quadrupole flow sorter. *Journal of Magnetism and Magnetic Materials*, [online] 194(1–3), pp.224–230. https://doi.org/10.1016/S0304-8853(98)00581-2.

Zeng, H., Li, Y., Xu, F., Jiang, H. and Zhang, W., 2015. Feasibility of turbidity removal by high-gradient superconducting magnetic separation. *Environmental Technology*, [online] 36(19), pp.2495–2501. https://doi.org/10.1080/09593330.2015.1036130.

Zhang, K., Liang, Q., Ma, S., Mu, X., Hu, P., Wang, Y. and Luo, G., 2009. On-chip manipulation of continuous picoliter-volume superparamagnetic droplets using a magnetic force. *Lab Chip*, [online] 9(20), pp.2992–2999. https://doi.org/10.1039/b906229g.

Zirak, M., Abdollahiyan, A., Eftekhari-Sis, B. and Saraei, M., 2018. Carboxymethyl cellulose coated Fe3O4@SiO2 core–shell magnetic nanoparticles for methylene blue removal: equilibrium, kinetic, and thermodynamic studies. *Cellulose*, [online] 25(1), pp.503–515. https://doi.org/10.1007/s10570-017-1590-5.

APPENDICES

APPENDIX A: Two-dimensional approximation in the modelling

The main objective of this appendix is to prove that the 2-D approximation of the BW-LGMS in the 3-D space in the modelling as well as simulation is reasonable without causing significant error in the model prediction. To prove this statement, the magnetic field gradients (generated by 3-D simulation) along a few straight lines that are aligned along *y*- and *z*- directions were plotted (see Figure A1). The purpose of plotting these graphs is to compare the forces along the both directions as the *i*-component of magnetophoretic force F_i is directly proportional to the partial derivative of magnetic field strength *B* with respect to i:

$$F_i \propto \frac{\partial B}{\partial i} \tag{A1}$$

The *x*-direction is not considered in this analysis because the system studied in this research has the longest length along this direction, thus, its dimension is crucial and must be taken into consideration in the modelling. Hence, the analysis providing here serves the purpose of excluding either *y*- or *z*-dimension out from analysis and reduced the problem from 3-D to 2-D. The results are tabulated in Figure A2.

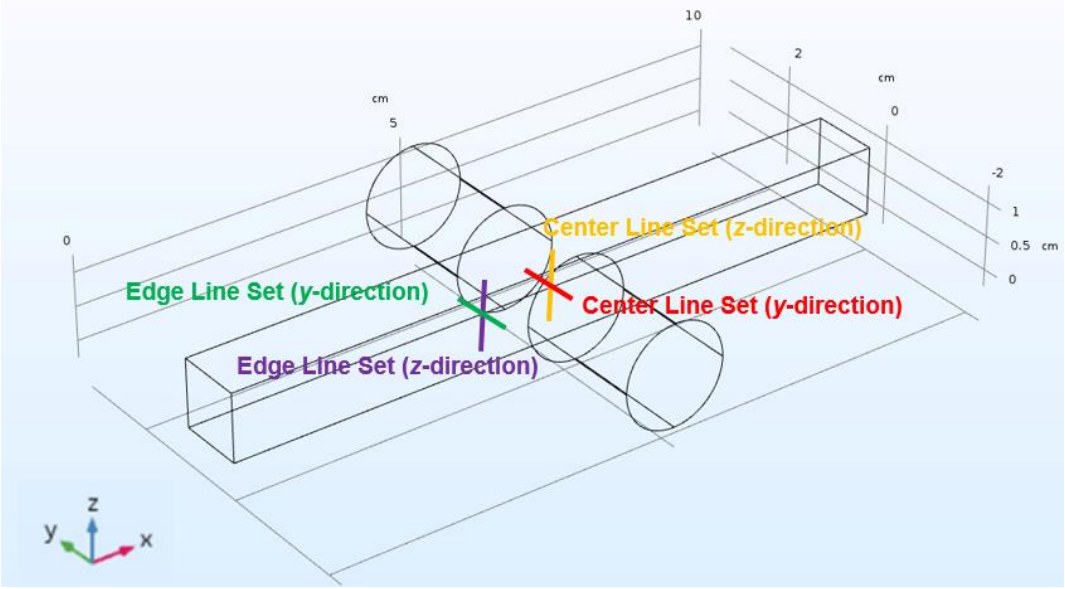

Figure A1: BW-LGMS model simulation in 3-dimensional space

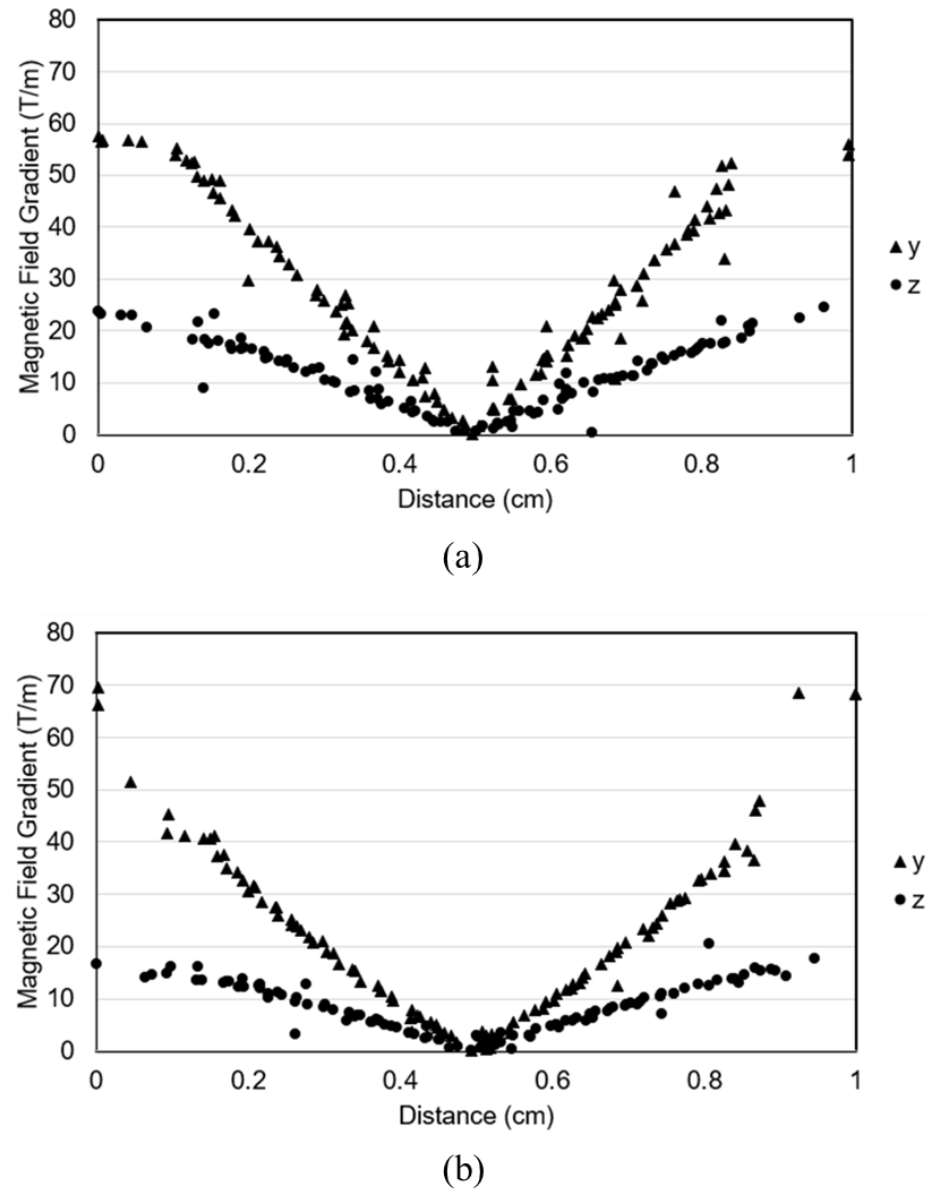

Figure A2: The magnetic field gradient along (A) Center Line Set and (B) Edge Line Set as shown in Figure A1.

According to the calculation, the directional derivative of magnetic field along the *y*-direction is always higher than their counterpart along the *z*-direction. For instance, for the Center Line Set, the maximum value of $\frac{\partial B}{\partial y}$ can reach ~60 T/m while only ~20 T/m is being recorded for $\frac{\partial B}{\partial z}$, which indicates that the *y*-component of magnetophoretic force is about ~3 times larger than

the *z*-component (Figure A2 (a)). On the other hand, the *y*-component of magnetophoretic force can be ~4 times larger than its *z*-component for the Edge Line Set (Figure A2 (b)). Therefore, this scenario causes the horizontal motion of MNPs (along the *y*-direction) to overwhelm its vertical motion (along the *z*-direction). Owing to this reason, the vertical (or *z*-) component of the system was neglected in the modelling, which reduces the 3-D problem to 2-D problem with only *x*- and *y*- components. Such a simplification on the BW-LGMS process has greatly reduced the consumption of computational power yet producing results that are sufficiently accurate for the analysis of this study. It is noteworthy to stress that the main purpose of the BW-LGMS experiments in this study is to qualitatively compare the time-lapsed MNP distribution so that the transport mechanism that is dominating can be determined, without involving intensive numerical analysis. Due to these reasons, 2-D space simulation of BW-LGMS process is sufficient to serve the purpose in current study. In addition, Leong and coworkers works on low gradient magnetic separation of MNP solution with similar length scale (Leong, Ahmad and Lim, 2015; Leong et al., 2017) have also shown a good agreement between the experimental and simulation results by using 2-D approximation in the modelling and numerical calculation.

APPENDIX B: Calculation of magnetic volume fraction of PSS-functionalized-MNPs and aggregation parameter, *N**

Magnetic Volume Fraction of PSS-functionalized-MNPs cluster

According to magnetization curves reported in this study (Figure 4.3), the saturation magnetization value, M_s, of unmodified MNPs and PSS-functionalized-MNPs is 70.41 and 69.48 emu/g, respectively. By assuming the magnetic response is entirely originated from the MNP (PSS does not contribute any magnetic response), the mass fraction of MNP within the PSS-functionalized-MNPs can be estimated as follows:

Mass fraction of MNP in PSS-functionalized-MNPs cluster

$$= \frac{69.48\ emu/kg}{70.41\ emu/kg} \times 100\%$$

= 98.68 wt%

Mass fraction of PSS in PSS-functionalized-MNPs cluster

= 100 – 98.68

= 1.32 wt%

Now, assuming that the packing factor of the MNP clusters is 0.74 (only 74 vol% of the cluster is occupied by MNP and PSS, which is the densest packing of the hard spheres), density of MNP is 5180 kg/m^3 and density of PSS is 810 kg/m^3

(Leong et al., 2017). With the assumptions stated above, the volume fraction of MNPs in the cluster can be estimated:

Volume fraction of MNP in PSS-functionalized-MNPs cluster

$$= \frac{\frac{0.9868}{5180\ kg/m^3}}{\frac{0.9868}{5180\ kg/m^3} + \frac{0.0132}{810\ kg/m^3}} \times 0.74$$

$$= 0.6820$$

Aggregation Parameter, *N**

Volume of MNP in one PSS-functionalized-MNPs cluster[#] , V

$$= \frac{\pi d^3}{6} \times\ 68.20\% = \frac{\pi(245.3 \times 10^{-9})^3}{6} \times 0.6820$$

$$= 5.271 \times 10^{-21} m^3$$

[#]With average hydrodynamic diameter of 245.3 nm (see Figure 4.2 (b)).

Mass of MNP in one PSS-functionalized-MNPs cluster, m_p

$$= 5.271 \times 10^{-21} m^3 \times 5180\ kg/m^3$$

$$= 2.730 \times 10^{-17} kg$$

The dimension of magnet used in the experiment is: radius, r = 0.75 cm and height, h = 2 cm. Therefore, at the surface of the magnet (y = 0),

$$B = \frac{B_r}{2}\left[\frac{y+h}{\sqrt{(y+h)^2 + r^2}} - \frac{y}{\sqrt{y^2 + r^2}}\right]$$

$$= \frac{1.45}{2}\left[\frac{0 + 0.02}{\sqrt{(0+0.02)^2 + 0.0075^2}} - \frac{0}{\sqrt{0^2 + 0.0075^2}}\right] = 0.6788\ T$$

$$H = \frac{B}{u} = \frac{0.6788}{1.257 \times 10^{-6}} = 5.40 \times 10^{5}\ A/m$$

Then, the magnetic dipole moment carried by one PSS-functionalized-MNPs cluster is with the saturation magnetization value, M_s, of pure MNP is 70.41 emu/g:

$$m = m_p M_{p,m}$$

$$= (2.730 \times 10^{-17}\ kg)\ (70.41\ A \cdot m^2/kg)$$

$$= 1.922 \times 10^{-15}\text{A.m}^2$$

Finally, the aggregation parameter N^* of MNP solution at concentration of 80 mg/L can be computed as follows:

$$\Gamma = \frac{\mu_0\, m^2}{2\pi d^3 k_B T}$$

$$= \frac{1.257 \times 10^{-6} \times (1.922 \times 10^{-15})^2}{2\pi \times (245.3 \times 10^{-9})^3 \times 1.381 \times 10^{-23} \times 298}$$

$$= 12167$$

$$\emptyset_0 = \frac{c}{\rho_p} = \frac{0.08}{5180 \times 0.6820} = 2.265 \times 10^{-5}$$

$$N^* = \sqrt{\emptyset_0 e^{\Gamma - 1}}$$

$$= \sqrt{(2.265 \times 10^{-5}) e^{12167-1}}$$

$$= 9.662 \times 10^{5278} \gg 1$$

The extremely huge value of N^* indicates that the MNP system employed in this study is indeed a cooperative system with remarkable aggregation effect, which should be considered in the modelling of the magnetic separation process. In addition, it should be noted that the MNP system has no sufficient MNP and time to form such a large aggregate with such a large number of particles and achieve the equilibrium state (which is not a practical scenario in the reality). So, the calculated value here is only to prove the interacting-nature of the MNP system and it does not reflect the number of MNP per aggregate throughout the CF-LGMS experiment. The method to estimate the number of MNP per aggregate during the experiment can be found in Section 4.2.3 and Appendix E.

APPENDIX C: Justification on the significance of Brownian Motion effect on the LGMS experiments.

The main intention of this section is to justify that the Brownian motion effect is negligible for the particle systems that studied and reported in this work. In order to clarify this point further, a numerical estimation on the order of magnitude of the Brownian motion effect is determined, by estimating the magnitude of the diffusive displacement of the particles during the experiment. In this study are using MNP aggregate (ζ' = $3.579 \times 10^{-6}\, m$) that are suspended in water with viscosity of ~0.00089 Pa.s under room temperature (*T* = 298 K). According to Einstein-Stokes Equation, the diffusion coefficient of the particle can be estimated as:

$$D = \frac{kT}{\zeta'\eta} = \frac{1.38 \times 10^{-23}(298)}{(0.00089)(3.579 \times 10^{-6})} = 1.29 \times 10^{-16} m^2/s$$

Using this diffusion coefficient, it can estimate the magnitude of the diffusive displacement of the particles in the radial direction of the separator during the experiment. Noting that the magnetophoresis experiment has a duration of about ~1200 seconds, the diffusive displacement of the MNP, *d* throughout the entire experiment is given by:

$$d \approx \sqrt{2Dt} = \sqrt{2 \times 1.29 \times 10^{-16} \times 1200}$$

$$\approx 5.57 \times 10^{-7} m \ll 1.5 \times 10^{-2} m$$

In the numerical estimation show that diffusive displacement of the MNP (5.57×10^{-5}cm) is much smaller than the length scale of the

experimental system (~1.5 cm), which indicates that Brownian motion exerts a negligible impact on the motion of magnetic particle as compared to magnetophoresis effect, and thus, it is not considered in the mathematical model.

APPENDIX D: Alignment of MNP aggregates in separator column

During the aggregation of MNPs in the magnetophoresis, they would form non-spherical shapes (this study has indeed incorporated this feature into modelling). According to the experimental observation, the aggregates of MNP clusters are expected to be of the elongated shape (slender aggregates) due to the dipolar nature of the magnetic interaction leading to particle chaining. The orientation of the aggregated MNP chains is following to the direction of the magnetic field lines when the external magnetic field is present (de Las Cuevas, Faraudo and Camacho, 2008). On the other hand, the motion of MNPs is following the direction of magnetic field gradient ∇B. The vector of magnetic field lines and magnetic field gradient ∇B on two of experiment/simulation setups (magnet arrangements A1 and A4 under the BW-LGMS experiments) were simulated, which is shown in Figure A3.

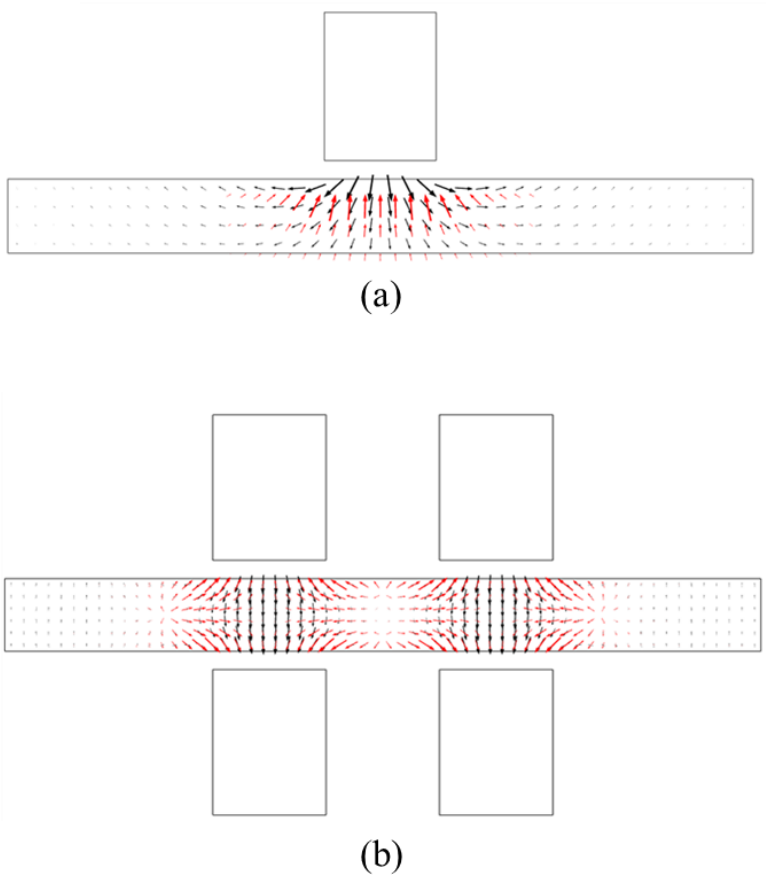

Figure A3: The vector of magnetic field lines is indicated as the black arrows while the magnetic field gradient ∇B vectors are indicated as the red arrows on magnet arrangements (a) A1 and (b) A4.

According to Figure A3, both magnetic field line and magnetic field gradient vectors ∇B (black and red arrows) are almost aligned among each other at the region near to magnet where the magnetophoresis is very significant. Therefore, at the region in which the magnetophoresis is fast and dominating the overall kinetics (near to magnet), the aggregate chains are orientated along the direction of the magnetic field gradient ∇B or magnetophoretic force $\overrightarrow{F_{mag}}$ (because both magnetic field line and ∇B are almost aligned among one another). Since the friction coefficient ζ' adopted in the modelling is that defined along the long axis of the aggregate chain, it can

be claimed that the drag force $\overrightarrow{F_d}$ formulated in this model is also collinear with the ∇B or $\overrightarrow{F_{mag}}$ (but they are having the opposite sense). This fact is indeed in-line with Equation (2.8). At the region that are further away from the magnets, the magnetic field lines (black arrows) and magnetic field gradient ∇B (red arrows) maybe misaligned, as indicated in Figure A3. However, the magnetophoresis at these region is relatively much slower which only exerts negligible effect on the overall kinetics of magnetophoresis. Therefore, the assumption which is leading to Equation (4.2) does not impose significant error in the modelling of CF-LGMS process.

APPENDIX E: Calculation on size of MNP aggregates

The dimension of magnet used to determine the separation kinetic profiles is given by radius, r = 2 cm and height, h = 4 cm. Therefore, the magnetic field gradient at the surface of the magnet (y = 0) (Leong, Ahmad and Lim, 2015) is:

$$\nabla B|_{z=0} = \frac{B_r r^2}{2}\left[\frac{1}{[(z+h)^2+r^2]^{\frac{3}{2}}} - \frac{1}{[z^2+r^2]^{\frac{3}{2}}}\right]$$

$$= \frac{1.45 \times 0.02^2}{2}\left[\frac{1}{[(0+0.04)^2+0.02^2]^{\frac{3}{2}}} - \frac{1}{[0^2+0.02^2]^{\frac{3}{2}}}\right]$$

$$= 33.01\ kg/m \cdot s^2 \cdot A$$

The magnetic dipole moment carried by one PSS-coated MNP cluster with the saturation magnetization value, M_s, of 70.41 emu/g is given by (MNPs achieve saturation magnetization at the MNP collection plane with relatively high magnetic field strength):

$$\mu = m_p M_s$$

$$= (2.730 \times 10^{-17} kg)\ (70.41\ A \cdot m^2/kg)$$

$$= 1.922 \times 10^{-15} \text{A.m}^2$$

Next, the number of MNP clusters in one MNP aggregate at concentration of 80 mg/L can be computed as follows. First, it can be found that the rate constant is 0.001592 s^{-1} under this MNP concentration (please refer to Table

4.1). According to Equation (4.4), the magnetophoretic velocity of MNP at the MNP collection plane with cuvette dimension of 1 cm × 1 cm × 4 cm is given by:

$$v_z(z=0) = \frac{k\,V_s}{A_s}$$

$$= (0.001592\ s^{-1})\frac{4\ \times 10^{-6}\ m^3}{1\ \times 10^{-4}\ m^2} = \ 6.368\ \times 10^{-5}\ m/s$$

After that, the number of MNP cluster in one slender aggregate can be calculated from Equation (4.6) by using this $v_z(z=0)$ value. In addition, it can be known that $\nabla B|_{z=0}$ = 33.01 $kg/m \cdot s^2 \cdot A$ and the viscosity of the MNP solution is 0.00089 Pa.s. Thus:

$$\frac{\mu}{\zeta'} = \frac{v_z(z=0)\eta}{\nabla B|_{z=0}} = \frac{N\,\mu_1}{2\pi N d}\left(\ln(2N) - \frac{1}{2}\right)$$

$$= \frac{(6.368\ \times 10^{-5})(8.9 \times 10^{-4})}{33.01} = \frac{1.922\ \times 10^{-15}\ N}{2\pi\ \times\ 245.3 \times 10^{-9}\ N}\left(\ln(2N) - \frac{1}{2}\right)$$

By solving the equation above, it can be found that $N\ \cong\ 3$.

Therefore, the mass and size of the MNP aggregate is:

Mass of MNP in one MNP aggregate

= Mass of MNP in one MNP cluster, $m_p\ \times N$

= $2.730 \times 10^{-17} kg\ \times 3$

= $8.191 \times 10^{-17} kg$

In addition, the friction factor also can be calculated as follows:

$$\zeta' = \frac{2\pi Nd}{\ln(2N) - \frac{1}{2}} = \frac{2\pi \times 3 \times 245.3 \times 10^{-9}}{\ln(2 \times 3) - \frac{1}{2}} = 3.579 \times 10^{-6}\, m$$

LIST OF PUBLICATION

1. Tan, Y.W., Leong, S.S., Lim, J., Yeoh, W.M. and Toh, P.Y., 2022. Low-gradient magnetic separation of magnetic nanoparticles under continuous flow: Experimental study, transport mechanism and mathematical modelling. *Electrophoresis*, [online] 43(21–22), pp.2234–2249. https://doi.org/10.1002/elps.202200078.